DEVELOPMENT OF WEAR RESISTANT METAL MATRIX COMPOSITE COATINGS BASED ON LASER SURFACING ENGINEERING TECHNIQUE

MOINUDDIN MOHAMMED QUAZI

FACULTY OF ENGINEERING
UNIVERSITY OF MALAYA
KUALA LUMPUR

2017

DEVELOPMENT OF WEAR RESISTANT METAL MATRIX COMPOSITE COATINGS BASED ON LASER SURFACING ENGINEERING TECHNIQUE

MOINUDDIN MOHAMMED QUAZI

THESIS SUBMITTED IN FULFILMENT OF THE REQUIREMENTS FOR THE DEGREE OF DOCTOR OF PHILOSOPHY

FACULTY OF ENGINEERING
UNIVERSITY OF MALAYA
KUALA LUMPUR

2017

UNIVERSITY OF MALAYA

ORIGINAL LITERARY WORK DECLARATION

Name of Candidate: **MOINUDDIN MOHAMMED QUAZI**

Registration/Matric No: **KHA140059**

Name of Degree: **DOCTOR OF PHILOSOPHY**

Title of Thesis: DEVELOPMENT OF WEAR RESISTANT METAL MATRIX COMPOSITE COATINGS BASED ON LASER SURFACING ENGINEERING TECHNIQUE

Field of Study: **ADVANCE MATERIALS / NANO MATERIALS**

I do solemnly and sincerely declare that:

(1) I am the sole author/writer of this Work;
(2) This Work is original;
(3) Any use of any work in which copyright exists was done by way of fair dealing and for permitted purposes and any excerpt or extract from, or reference to or reproduction of any copyright work has been disclosed expressly and sufficiently and the title of the Work and its authorship have been acknowledged in this Work;
(4) I do not have any actual knowledge nor do I ought reasonably to know that the making of this work constitutes an infringement of any copyright work;
(5) I hereby assign all and every rights in the copyright to this Work to the University of Malaya ("UM"), who henceforth shall be owner of the copyright in this Work and that any reproduction or use in any form or by any means whatsoever is prohibited without the written consent of UM having been first had and obtained;
(6) I am fully aware that if in the course of making this Work I have infringed any copyright whether intentionally or otherwise, I may be subject to legal action or any other action as may be determined by UM.

Candidate's Signature Date:

Subscribed and solemnly declared before,

Witness's Signature Date:

Name:

Designation:

ABSTRACT

Laser based additive manufacturing technology (LAM) comprising of Laser composite surfacing (LCS) technique has emerged as an alternative photon driven manufacturing technology for the fabrication of hybrid metal matrix composite coatings to enhance the mechanical and tribological properties of critical machinery components. To meet the application needs, instead of bulk material processing, surface coatings are rendered far more suitable and are often utilized in form of Hybrid metal matric composite coatings (HMMC). These coatings have great potential in the fabrication and regeneration of automotive, aerospace, defense and manufacturing components as protective hard facing self-lubricating wear resistant composite coating. Under the category of lightweight metals, self-lubricating coatings have eluded aluminium alloys and researchers have not realized the potential of optimization techniques for the laser processing parameters. This may dramatically increase the friction coefficient and wear rates of critical sliding components and the full potential of improvement in mechanical and surface properties are not realized. The present work explores the possibility to utilize several wear resistant metal matrixes composite (MMC) and hybrid (HMMC) coatings with the assimilation of various solid lubricants in these coatings blends to investigate their tribo-mechanical performance. In the first phase fabrication, characterization and optimization of Ni-WC based wear resistant MMC coatings was deposited on aluminium alloy AA5083. To achieve laser composite surfacing, an analysis on optimization of laser processing parameters was made, in order to improve the tribo-mechanical properties of aluminium alloy. To carry out the investigation, Taguchi optimization method using standard orthogonal array of L_{16} (3^4) was employed. Thereafter, the results were analyzed using signal to noise (S/N) ratio response analysis and Pareto analysis of variance (ANOVA). Finally, confirmation tests with the best

parameter combinations obtained in the optimization process were made to demonstrate the progress made. Results showed that the surface hardness (953 H_v) and roughness (0.81μm) of coated AA5083 samples were enhanced by 9.27%, and 13.14% respectively. Tribological behavior of LCS samples was investigated using ball-on-plate tribometer against a counter-body of hardened and tempered 440c bearing steel. It was revealed that the wear of the Ni-WC coated samples improved to around 2.5 times. For lower applied loads, coating exhibited abrasive wear mode and a reduction in plastic deformation. In the second phase, solid lubricant coating comprising of lamellar graphite and TiO_2 was employed to fabricate Ni-WC based HMMC coatings on Al-Si hypereutectic piston alloy. The concentrations of both solid lubricants were varied in concentration of 5, 10, and 15 wt. % to identify their optimum concentration. Results indicated that the addition of graphite and TiO_2 to fabricate HMMC was beneficial in reducing friction and wear of Ni-WC MMC coating. Furthermore, the hardness of both coatings was improved. The wear mechanism of MMC coating was transformed into mild abrasive and adhesive after the addition of both solid lubricants.

ABSTRAK

Berasaskan teknologi pembuatan bahan tambahan Laser (LAM) yang terdiri daripada Laser permukaan komposit teknik (LCS) telah muncul sebagai foton didorong teknologi pembuatan alternatif untuk fabrikasi logam hibrid lapisan matriks komposit untuk meningkatkan sifat-sifat mekanikal dan tribological komponen jentera kritikal. Bagi memenuhi keperluan permohonan, daripada pemprosesan bahan pukal, lapisan permukaan diberikan jauh lebih sesuai dan sering digunakan dalam bentuk logam salutan komposit matrik Hibrid (HMMC). lapisan ini mempunyai potensi yang besar dalam pembuatan dan pertumbuhan semula automotif, aeroangkasa, pertahanan dan pembuatan komponen yang melindungi sukar dihadapi salutan komposit tahan Haus diri pelincir. Di bawah kategori logam ringan, lapisan diri pelincir tidak terurai aloi aluminium dan penyelidik tidak menyedari potensi teknik pengoptimuman untuk parameter pemprosesan laser. Ini secara mendadak boleh meningkatkan pekali geseran dan memakai kadar komponen gelongsor kritikal dan sepenuhnya potensi peningkatan dalam sifat-sifat mekanik dan permukaan tidak direalisasikan. Kajian yang meneroka kemungkinan untuk menggunakan beberapa memakai matriks logam tahan komposit (MMC) dan hibrid (HMMC) lapisan dengan asimilasi pelbagai pelincir pepejal dalam lapisan ini menggabungkan untuk menyiasat prestasi tribo-mekanikal mereka. Dalam fasa pertama fabrikasi, pencirian dan pengoptimuman Ni-WC memakai berdasarkan lapisan MMC tahan didepositkan pada aloi aluminium AA5083. Untuk mencapai laser komposit permukaan, analisis pengoptimuman parameter pemprosesan laser telah dibuat, untuk meningkatkan sifat-sifat tribo-mekanikal aloi aluminium. Menjalankan siasatan, kaedah pengoptimuman Taguchi menggunakan pelbagai ortogon taraf L16 (34) telah digunakan. Selepas itu, keputusan telah dianalisis dengan menggunakan isyarat-hingar analisis sambutan (S/N) nisbah dan analisis Pareto varians (ANOVA). Akhirnya, ujian pengesahan dengan kombinasi parameter yang terbaik diperolehi dalam

proses pengoptimuman telah dibuat untuk menunjukkan kemajuan yang dibuat. Hasil kajian menunjukkan bahawa kekerasan permukaan (953 Hv) dan kekasaran (0.81μm) sampel AA5083 bersalut telah dipertingkatkan masing-masing sebanyak 9.27%, dan 13.14%. tingkah laku Tribological sampel LCS disiasat menggunakan tribometer bola-on-plat terhadap balas badan keras dan marah 440C galas keluli. Ia telah mendedahkan bahawa memakai sampel Ni-WC bersalut meningkat kepada kira-kira 2.5 kali. Untuk beban yang lebih rendah gunaan, salutan dipamerkan mod memakai kasar dan pengurangan dalam ubah bentuk plastik. Dalam fasa kedua, pelincir pepejal yang terdiri daripada grafit lamela dan TiO_2 telah bekerja untuk mereka-reka Ni-WC lapisan HMMC berdasarkan Al-Si aloi omboh hipereutektik. Kepekatan kedua-dua pelincir pepejal telah diubah dalam kepekatan 5, 10, dan 15 wt. % Untuk mengenalpasti kepekatan optimum. Keputusan inducated bahawa penambahan grafit dan TiO_2 untuk mereka-reka HMMC adalah benifical dalam mengurangkan geseran dan haus lapisan MMC Ni-WC. Tambahan pula, kekerasan kedua-dua lapisan telah bertambah baik. Mekanisme memakai lapisan MMC telah berubah menjadi sederhana kasar dan pelekat selepas penambahan kedua-dua pelincir pepejal.

ACKNOWLEDGEMENTS

My father Syed Munawar Uddin Quazi is a lovely person and it is because of him that I have inherited such abilities in completing my PhD. My mother Shahina Tabassum is a woman whom I owe my life to. My son, Faseeh Uddin Mohammed Quazi who remained a source of inspiration to me, throughout the PhD tenure. I would like to express my gratitude to Dr. Mohammad Abul Fazal, Professor Dr. A.S.M.A Haseeb and Dr. Farazila Binti Yusof who have been my supervisor as well as the mentor of the thesis. My earnest thanks are given to my former mentor Dr. Erfan and Dr. A. D Sarhan.

I wish to extend my warmest thanks to all my colleagues in the Department of Mechanical Engineering and the laboratories that have made this work successful. Special mentions of Puan Hartini from surface engineering laboratory who helped me immensely. Moreover, I am thankful to Faculty of Dentistry and Faculty of Science for providing with characterization resources.

Last but not least all my teachers of Faculty of Engineering who have supported me in a way such that I was able to produce this research. Additionally, I am grateful to my friends Mr. Arslan Ahmad, Dr. Tipu sultan, Dr. Faisal Siddiqui and Mr. Ghulam Mujtaba Shaikh for their moral support. I would like to acknowledge the financial support provided by the Research Grant of University Malay's, Grant No CG061-2013 and PRO13A-13AET. My lovely father Syed Munawar Uddin Quazi also gave financial support to me. At last, I shall highly acknowledge the role of friends and family for their continuous commitment and rigorous help which are my only source of strength and vitality.

Moinuddin Mohammed Quazi

May 2016

TABLE OF CONTENTS

ABSTRACT ..... **iii**

ABSTRAK ..... **v**

ACKNOWLEDGEMENTS ..... **vii**

TABLE OF CONTENTS ..... **viii**

LIST OF FIGURES ..... **xiii**

LIST OF TABLES ..... **xviii**

LIST OF ABBREVIATIONS ..... **xix**

CHAPTER 1: INTRODUCTION **1**

1.1 Background 1

1.2 Problem Statement 5

1.3 Research Objectives 6

1.4 Framework of Thesis 6

CHAPTER 2: LITERATURE REVIEW **8**

2.1 Introduction to Lasers 8

2.1.1 Construction of Lasers 10

2.1.2 Classification of lasers 12

2.2 Lasers in Coatings Technology 13

2.3 Laser Surface Modification of Aluminium Alloys 15

2.3.1 High Power Lasers suitable for surface modification 18

2.3.2 Laser Surface Melting (LSM) 20

2.3.3 Laser Surface Alloying (LSA) 22

2.3.3.1 LSA with addition of Nickel (Ni) and Ni based Alloys 23

2.3.3.2 Addition of Chromium (Cr) and Cr based Surface Alloys 25

2.3.3.3 Addition of Copper (Cu) and Cu based Surface Alloys 25

2.3.3.4 Addition of Molybdenum (Mo) and Mo based Surface Alloy 25

2.3.3.5 Addition of Other Surface Alloying Systems 26

2.3.4 Laser Surface Cladding (LSC) 27

2.3.4.1 Cladding of Metallic/Alloy Layer 28
2.3.4.2 Cladding of Ceramic and Composite Layer 29
2.3.5 Laser Composite Surfacing (LCS) 34
2.3.5.1 Addition of Micron Sized Particles 35
2.3.5.2 Addition of Nanometer sized particles 37

2.4 Laser coatings incorporating solid-lubricants 38

2.4.1 Friction Reduction Mechanism 39
2.4.2 Classification of Solid-Lubricants 39
2.4.3 Lamellar based solids 40
2.4.3.1 Addition of Graphite 47
2.4.3.2 Addition of Molybdenum di sulphide (MoS_2) 49
2.4.3.3 Addition of Tungsten di sulphide (WS_2) 51
2.4.3.4 Addition of hexagonal boron nitride (hBN) 52
2.4.4 Halides and metal oxides based materials 53
2.4.4.1 Addition of calcium di fluoride (CaF_2) 59
2.4.4.2 Addition of Titanium di oxide (TiO_2) 59

2.5 Applications of laser based self-lubricating composite coatings 60

2.6 Statistical experimental design techniques 61

2.6.1 Taguchi Design of Experiment 62
2.6.2 Analysis of variance Pareto (ANOVA) technique 64

2.7 Summary and conclusion 65

CHAPTER 3: MATERIALS AND EXPERIMENTAL METHODS 67

3.1 Substrate Materials 67

3.1.1 AA5083-O Aluminium Wrought Alloy 67
3.1.2 Al-17Si Hypereutectic Cast alloy 67

3.2 Coating Materials 68

3.2.1 MMC coating powders 68
3.2.1.1 Nickel as Matrix phase 68
3.2.1.2 WC as Particulate phase 69
3.2.2 HMMC coating powders 69
3.2.2.1 Graphite as solid lubricant phase 70

3.2.2.2 TiO_2 as solid lubricant phase 70

3.3 Experimental Methods 71

3.3.1 Substrate pre-processing 72
3.3.2 Powder Pre-placement 72
3.3.2.1 MMC coating composition 73
3.3.2.2 HMMC coating composition 73
3.3.3 Laser Surface Processing 74
3.3.3.1 Laser processing parameters for MMC coating 74
3.3.3.2 Laser processing parameters for HMMC coatings 75

3.4 Characterization and microstructural analysis 75

3.4.1 Scanning Electron Microscopy (SEM) 76
3.4.1.1 Beam-Specimen Interactions 76
3.4.1.2 Equipment Details 76
3.4.2 Atomic Force Microscopy (AFM) 77
3.4.2.1 Equipment Details 77
3.4.3 Xray-Diffraction (XRD) 78
3.4.3.1 Fundamentals 78
3.4.3.2 Equipment Details 79

3.5 Surface analysis 79

3.5.1 Vickers Micro-hardness 79
3.5.2 3D surface scan, surface profilometry and roughness Testing 80

3.6 Tribological Testing 80

3.6.1 Tribological testing parameters for AA5083 and MMC coating 82
3.6.2 Tribological testing parameters for Al-17Si and HMMC coating 82

3.7 Comparative evaluations between MMC and HMMC coatings 82

CHAPTER 4: RESULTS AND DISCUSSION 84

4.1 Optimization of Ni-WC MMC coating 84

4.1.1 Design of experiment 84
4.1.2 Taguchi method: analysis of the signal-to-noise ratio 85
4.1.3 Influence of processing parameters on hardness and roughness 89
4.1.4 Pareto-ANOVA Analysis 90

4.2 Microstructure and Phase identification 94
4.2.1 Microstructure and Phase identification of Ni-WC coating 94
4.2.2 Microstructure of substrate Al-17Si hypereutectic alloy 100
4.2.3 HMMC coating deposited on Al-17Si 101
4.2.4 Phase identification of Ni-WC-Graphite coating 103
4.2.5 Phase identification of Ni-WC-TiO_2 coating 104
4.3 Hardness of MMC and HMMC coatings 106
4.4 Tribological properties of MMC coating 107
4.4.1 Wear and friction coefficient of AA5083 and Ni-WC coating 108
4.4.2 Characterization of worn surface and debris 112
4.4.3 Atomic force microscopy of worn scars 117
4.5 Tribological properties of HMMC coatings 118
4.5.1 Wear and friction coefficient of Al-17Si substrate, Ni-WC-Graphite and Ni-WC-TiO_2 coating 118
4.5.2 Wear characteristics of substrate Al-17Si alloy 122
4.5.2.1 Characterization of worn surfaces 123
4.5.2.2 Counter-body wear and debris analysis 124
4.5.3 Wear characteristics of Ni-WC-Graphite coating 126
4.5.3.1 Characterization of worn surface 126
4.5.3.2 Counter-body wear and debris analysis 129
4.5.4 Wear characteristics of Ni-WC-TiO_2 coating 134
4.5.4.1 Characterization of worn surface 134
4.5.4.2 Counter-body wear and debris analysis 137
4.6 Comparative Evaluations 140
4.6.1 3D Surface scans and roughness profilometry of worn scars for AA5083, Al-17Si, MMC and HMMC coatings 140
4.6.2 Comparative evaluation of wear mechanism for AA5083, Al-17Si, MMC and HMMC coatings 145
CHAPTER 5: CONCLUSION AND FUTURE WORK 149
5.1 Conclusion 149
5.2 Future Work 149
REFERENCES 152

LIST OF PUBLICATIONS **170**

AWARDS **173**

LIST OF FIGURES

Figure 2.1: The power density range for various laser-material processing and joining (Majumdar & Manna, 2003) 9

Figure 2.2: Application of laser in various manufacturing processes (Majumdar & Manna, 2003) 10

Figure 2.3: The structure of typical laser equipment (Majumdar & Manna, 2003) 10

Figure 2.4: (a) Schematics of the LSC process (b) an Ishikawa diagram of LSC (Mondal et al., 2011) 15

Figure 2.5: Energy absorption of the laser beam for pure aluminum, AA5456 and AA6063 (%). 17

Figure 2.6: Spectral reflectance of aluminum and various other metals. (Reprinted with permission from Elsevier, License no: 3575990476470) (L. Li, 2000) 19

Figure 2.7: Schematics of LSM I – in the area of the laser scanned filet and II – the area between laser-scanned filets. (Reprinted with permission from Elsevier, License no: 3575150149465) (Pariona et al., 2013) 21

Figure 2.8: Vickers hardness of various Al alloys after LSM treatment. 21

Figure 2.9: Schematics of LSA: (a) direct injection of powder and (b) preplaced powder technique. (Reprinted with minor modification taking permission from Springer, License no: 3575790741638) (Singh & Harimkar, 2012) 22

Figure 2.10: Vickers hardness of various Al alloys after LSA treatment. 23

Figure 2.11: Effect of powder flow rate on: (a) surface hardness and (b) mass loss of Ni and Ni-Ti-C alloying as obtained by pin-on-disk wear testing. (Reprinted with permission from Elsevier, License no: 3575180604467) (D'Amato et al., 2014a) 24

Figure 2.12: Evolution of microstructure of Al–Mo surface alloy remelted (a-d) under increased traverse speed. (Reprinted with permission from Elsevier, License no: 3575180909391) (Amélia Almeida et al., 2006) 26

Figure 2.13: Vickers hardness of different laser claddings on aluminum alloys 28

Figure 2.14: LSC application in a) valve seat repair and b) piston ring groove repair. (Reprinted with permission from Springer, License no: 3575181179845) (Arnold & Volz, 1999) 29

Figure 2.15: SEM image of a) cross sectional microstructure 20 wt% Mo and 80 wt% WC laser clad, (b) 100 wt% WC cladded wear track and (c) magnified view of cracks on wear track. (Reprinted with permission from Elsevier, License no: 3575820558488) (Chong et al., 2001).....33

Figure 2.16: (a) Axicon and Plano-convex lens configuration to produce ring beam profile and (b) energy intensity distribution of ring beams in comparison to conventional Gaussian beam (Reprinted with permission from Elsevier, License no: 3575190366744) (Blum & Molian, 2014) 37

Figure 2.17: Schematics of adhesive contact between two surfaces and adhesion leading to the generation of transfer film which is detached from the softer solid and adhered to the harder solid.....39

Figure 2.18: The Vickers hardness of various claddings with and without lamellar based solids lubricant 41

Figure 2.19: Friction coefficient enhancement due to addition of lamellar based solids lubricant.....41

Figure 2.20: Micro hardness of various samples cladded with additions of solid lubricant.....54

Figure 2.21: Reduction in friction coefficient of various samples cladded with additions of solid lubricant 54

Figure 3.1: Schematics of (a) sandblasting of substrate; (b) Powder pre-placement; (c) laser processing 3D- view; (d) cross-sectional view.....71

Figure 3.2: Schematic diagram of the ball on plate tribometer.....81

Figure 3.3: Block diagram depicting the key steps involved in the fabrication and characterization of the MMC and HMMC coatings 83

Figure 4.1: The signal to noise (S/N) response graph for (a) surface hardness, (b) surface roughness 88

Figure 4.2: The XRD pattern of laser composite surfaced AA5083 with Ni-WC coating 94

Figure 4.3: Cross-sectional optical micrograph of single scanned track 95

Figure 4.4: SEM overview of overlay of Ni-WC coating.....95

Figure 4.5: SEM cross sectional images along with EDS spot scanning for (a) top section of Ni-WC coating with a magnified view of Al_3Ni dendritic structure, (b) middle section containing dendrites of Al_3Ni_2 and AlNi 97

Figure 4.6: EDS area scanning for (a) top section of Ni-WC coating with, (b) middle section 99

Figure 4.7: Optical micrograph of Al-17 wt. % hypereutectic piston alloy at 20X magnification..... 100

Figure 4.8: SEM and EDS area mapping of Al-Si hypereutectic alloy 100

Figure 4.9: SEM cross-sectional view of laser composite surfacing of Ni-WC-graphite based composite coating deposited on Al-17Si Substrate 101

Figure 4.10: SEM cross-sectional view of substrate/coating interface of Ni-WC-graphite based composite coating deposited on Al-1Si Substrate 102

Figure 4.11: SEM overview of overlay of Ni-WC-graphite coating overlays..... 102

Figure 4.12: The X-ray diffraction spectrum for Ni-WC coating with graphite content (a) 5 wt. % (b) 10 wt. % and (c) 15 wt. % 103

Figure 4.13: The X-ray diffraction spectrum for Ni-WC coating with TiO_2 content (a) 5 wt. % (b) 10 wt. % and (c) 15 wt. %..... 105

Figure 4.14: The surface hardness profiles for Ni-WC coating with graphite and TiO_2 content..... 107

Figure 4.15: The friction coefficient of (a) AA5083 and (b) Ni-WC coating as a function of cumulative time for 10, 20, 30 and 40 N load 109

Figure 4.16: (a) Steady state friction coefficient of AA5083 and Ni-WC coating under various applied loads, (b) Wear response of AA5083 and laser treated Ni-WC coating. 111

Figure 4.17: Scanning electron micrograph of worn surfaces for (a) AA5083 and (b) Ni-WC coating along with their EDS spectra of (c) area E and (d) area F 114

Figure 4.18: SEM images of debris for (a) AA5083 and (b) Ni-WC coating along with optical micrograph of 440c steel counter-body for (c) AA5083 and (d) Ni-WC coating 115

Figure 4.19: Atomic force microscopy (AFM) images of worn scar morphology of (a) AA5083; (b) Ni-WC coating..... 118

Figure 4.20: The friction coefficient of Al-17%Si and coatings with graphite and TiO_2 additives 119

Figure 4.21: (a) Wear response of Al-17Si and laser treated Ni-WC coating with additives (b) Steady state friction coefficient of Al-17Si and laser treated Ni-WC coating with additives 121

Figure 4.22: Scanning electron micrograph of worn surfaces for Al-Si alloy (a) Debris-scar interface, (b) and (c) at 0.5K and 1.0K magnification along with corresponding (d) EDX elemental mapping of O, Al, Si, Ni and Fe elements 124

Figure 4.23: (a) EDX mapping of images for debris of Al-17%Si debris elemental mapping, (b) and (c) SEM image of debris at 0.5k and 2.0k magnification, (d) EDX elemental mapping of Al, O, Si and Fe and Fe element debris, (e) and (f) optical micrograph of counter body scar at distinctive magnifications 125

Figure 4.24: SEM image of coating wear with their magnified views for (a), (b) 5 wt. % graphite (d), (e) 10 wt. % graphite, (g), (h) 15 wt. % graphite, along with their corresponding EDX carbon element mapping in (c), (f) and (i). 127

Figure 4.25: EDS spot scanning spectrums on worn scars of (a) Ni-WC-5 wt. % Graphite, (b) Ni-WC-10 wt. % Graphite and (c) Ni-WC-15 wt. % Graphite 129

Figure 4.26: Optical micrographic images of counter-body worn tracks at lower and higher magnification for (a), (b) 5 wt. % graphite (c), (d) 10 wt. % graphite, (e), (f) 15 wt. % graphite 130

Figure 4.27: SEM images of counter-body worn debris at lower and higher magnification for (a), (b) 5 wt. % graphite (c), (d) 10 wt. % graphite, (e), (f) 15 wt. % graphite..... 133

Figure 4.28: SEM image of coating with their magnified view for (a), (b) 5 wt. % TiO_2 (d), (e) 10 wt. % TiO_2, (g), (h) 15 wt. % TiO_2, along with their corresponding EDX titanium element mapping in (c), (f) and (i)..... 135

Figure 4.29: EDS spot scanning spectrums on worn scars of (a) Ni-WC-5 wt. % TiO_2, (b) Ni-WC-10 wt. % TiO_2 and (c) Ni-WC-15 wt. % TiO_2..... 137

Figure 4.30: Optical micrographic images of counter-body worn tracks at lower and higher magnification views for (a), (b) 5 wt. % TiO_2 (d), (e) 10 wt. % TiO_2, (g), (h) 15 wt. % TiO_2..... 138

Figure 4.31: SEM images of counter-body worn debris at lower and higher magnification for (a), (b) 5 wt. % TiO_2 (c), (d) 10 wt. % TiO_2, (e), (f) 15 wt. % TiO_2 140

Figure 4.32: 3D surface scans for (a) AA5083, (b) Al-17Si (c) Ni-WC, (d) Ni-WC-15 wt. % Graphite (e) Ni-WC-15 wt. % TiO_2..... 141

Figure 4.33: Surface roughness (R_a) of worn scars in nano-meters for substrates and coatings. 142

Figure 4.34: Surface profilometry scans for (a) AA5083, (b) Al-17Si (c) Ni-WC, (d) Ni-WC-15 wt. % Graphite (e) Ni-WC-15 wt. % TiO_2. 144

LIST OF TABLES

Table 2.1: List of various Al substrate laser surface cladding with different processing parameters. 31

Table 2.2: A summary of tribological testing parameters when lamellar based solid lubricants are incorporated 44

Table 2.3: A summary of tribological testing parameters when halides and oxide based solid lubricants are incorporated 55

Table 2.4: A summary of LSC and tribological testing parameters with the addition of combination of solid lubricants and soft metals 57

Table 3.1: A summary of all material properties of all materials utilized 70

Table 3.2: Laser processing parameters and their levels employed for the fabrication of MMC Ni-WC coating 75

Table 4.1: Laser processing parameters and their levels employed in this experiment .. 84

Table 4.2: The measure values of surface hardness and roughness with their corresponding calculated S/N ratios 86

Table 4.3: The (S/N) response values of laser processed AA5083 for surface hardness and for surface roughness 87

Table 4.4: Pareto-ANOVA analysis for surface hardness 92

Table 4.5: Pareto-ANOVA analysis for surface roughness 93

Table 4.6: The EDS chemical composition (at. %) by spot scan along with corresponding XRD phases detected. 97

Table 4.7: A summary of Tribo-mecahnical properties of substrates and coatings 145

Table 4.8: Comparative analyses of wear mechanisms for substrates, MMC and HMMC coatings based on worn scar, debris and counter-body morphology 147

LIST OF ABBREVIATIONS

Arabic Symbols

f	Frequency	HZ
P	Normal load	N
F_k	Kinetic Frictional Force	N
H	Hardness	MPa
H_v	Vicker's hardness	MPa
R_a	Arithmetic average of roughness	μm
R_{max}	Maximum surface roughness	μm
s	Sliding distance	m
v	Sliding velocity	m/s
V	Volume	mm^3
t	Sliding time	min

Greek Symbols

μ_k	Kinetic Friction	-
ρ	Density	$Kg.m^{-3}$

Abbreviations

LASER	Light amplification by spontaneous emission of radiation
Ni	Nickel
WC	Tungsten Carbide
LSA	Laser Surface Alloying
LSM	Laser surface Melting
LSC	Laser surface cladding
LCS	Laser composite Surfacing

Abbreviations

AA	Aluminum Association
COF	Coefficient of Friction
CTE	Coefficient of Thermal Expansion
SEM	Scanning Electron Microscopy
FESEM	Field emission scanning electron microscopy
EDX	Energy dispersive X-Ray spectroscopy
OM	Optical Microscopy
AFM	Atomic Force Microscopy
XRD	X-Ray diffraction
AISI	American Iron and Steel Institute
ASM	American Society of Materials
MMC	Metal Matrix Composite
HMMC	Hybrid Metal Matrix Composite
AMC	Aluminum matrix composite

CHAPTER 1: INTRODUCTION

1.1 Background

Aluminum (Al) is the first most abundant metal and the third most abundant element (after oxygen and silicon) making about 8-wt% of earth crust. Al having a low density of 2.7 g/cm^3 is currently replacing dense ferrous materials due to relentless pressure in the second half of the 20th century to curb fossil fuels consumption. Aluminum metal has excellent properties such as good machinability, ductility, workability, weld-ability and ease of recyclability (Dursun & Soutis, 2014). Introducing alloying elements in Al matrix such as, chromium, copper, lithium, magnesium, molybdenum, nickel, silicon and zinc intensifies strength, cast-ability and heat resistance. However, Al alloys under specific conditions remains unsuitable for various structural and machinery applications owing to their insufficient resistance to erosion, fatigue and tribochemical wear (Kalita, 2011; Richman & McNaughton, 1990). These properties are associated with near surface regions. Thus without degrading the critical properties of the bulk phase, the modification of composition and microstructure through localized processing or surface engineering serves as a viable solution for widening the application of aluminum alloys.

Surface technology processes such as ion implantation especially with nitrogen (Figueroa et al., 2012; Oñate et al., 1998), cyro-milling (Tang et al., 2008), plasma nitriding (F. Y. Zhang & Yan, 2014) and plasma sintering (Bathula et al., 2012) have been carried out to enhance mechanical properties of Al alloys. In addition, numerous other surface engineering techniques such as anodizing (Sarhan et al., 2013), physical vapor deposition (PVD) Ezazi et al. (2014a), chemical vapor deposition (CVD) (Uhlmann et al., 2014), thermal spraying (Picas et al., 2005) and sol gel coatings (Sepeur & Frenzer, 2014) have been employed to produce tens of micro and nanometer coatings. Nevertheless, owing to the difference in film-to-substrate elastic modulus, the

thin hardened layer is prone to cracking on softer Al substrates, thereby resulting in higher specific wear. Furthermore, poor film-to substrate adhesion leads to adhesion, cohesion and delamination failure in a tribological contact. The aforementioned arguments convincingly demonstrate that a thicker, harder layer will entail far superior tribological characteristics.

Laser surface engineering (LSE) is a non-contact material processing technique and has manifested possibilities for novel material research. Although LSE techniques have been around for the last 35 years (Zhong & Liu, 2010), but the research interest has increased since the past decade (Dubourg & Archambeault, 2008). LSE introduces laser controlled melting in the presence of particulate embedding and composition modifying film to furnish a precise balance of prerequisite properties. With lasers, novel microstructures can be developed due to rapid solidification and incorporation of higher concentration of key elements (Singh & Harimkar, 2012). The coatings developed by conventional means are incapable of generating such microstructures since extended solid solutions or metastable phases are mainly characterized by rapid solidification rates. This localized processing technique allows the fabrication of materials made from a combination of transition metal nitrides, oxides, carbides and borides and incorporates higher metallurgical bond strength owing to laser's high coherence, directionality and high energy density (Pawlowski, 1999). The higher bond strength eradicates the possibilities of film-to-substrate delamination failure and reduction in tribological performance due to the presence of interfacial defects (Biswas, 2006).

Since, wear, friction, and lubrication of material systems are one the most vital characteristics arousing the attention of almost all mechanical engineers in the field of surface engineering. These properties are of utmost importance when determining the tribological characteristics of critical sliding components. With the development of

modern mechanical systems in aerospace, manufacturing and food industries, various components are now operating under severe conditions. Their working conditions may encompass excessive temperature (at 1000°C or above), high stress, fluid contamination, vacuum and corrosive or leakage prone environment. In such situations, the use of conventional or even advanced synthetic lubricants is compromised. Moreover, they cannot be used because of the difficulty in sealing, applying, transporting and other factors. For instance, there are various components employed in the nuclear energy and aviation industries that operate under high-temperature tribological load such as steam and gas power plant turbines, compressor blades (high pressure and temperature), cylinder liners, sidewall seals, exhaust valves and exhaust components, nuclear valves, piping, adiabatic engine bearings etc. (Kathuria, 2000; Miyoshi, 2007; Sexton et al., 2002). Also, there are numerous applications where the presence of lubricants is undesirable, impractical or is forbidden owing to the risk of contamination (food industries). Hence, under the given circumstances, liquid lubricant ceases to perform its function and an alternate solution is required in reducing wear and friction.

The use of solid lubricant in composite coatings becomes a prerequisite in providing a low friction transfer film and protecting the opposing surface (Renevier et al., 2001). As wear is dependent on surface properties, modifying the near surface regions only can enhance it. It is known that for tribological and solid lubricant coatings, the adhesion strength between the composite coating and substrates is the critical property. Thermal spraying and thin film techniques have a distinct interface between substrate and coating. The separated film-to-substrate interface inevitably leads to adhesion and delamination failure under wear (Leyland & Matthews, 2000). In LSC, there is a strong bond not only between the coating and substrate, but also between the matrix and

reinforced phase. In particular, the underlying limitations of plasma-based composite coatings are problems of high porosity, poor inter-particle bonding, and extensive chemical inhomogeneity (Milella et al., 2001). It is worth mentioning that laser remelting can significantly enhance the quality of plasma spray coatings (K. L. Wang et al., 2000).

Laser composite surfacing (LCS) gives the advantage of fabricating in-situ composites by assisting the reactions between added pure elements or compounds (X.-B. Liu, Meng, et al., 2014). In this way, the interface is cleaner and the reinforcements are more compatible with the matrix. LSC easily produces those distinctive phases, which are sometimes difficult to obtain (Singh & Harimkar, 2012). In electro deposition, the volume content of the self-lubricating particulate phase is difficult to control and particles can frequently agglomerate causing deterioration of composite properties (Praveen & Venkatesha, 2008). PTA surfacing technique limits the size of particulates that can be added in the composite coating. LSC allows all types of particle size to be added effectively in the coating. Furthermore, with the careful selection of processing parameters, it also eliminates particle agglomeration, offers sound fusion bonding with the surface, high deposition rates, fine quench microstructures comprising of near isotropic mechanical properties (Farahmand & Kovacevic, 2014; Weng et al., 2014). Only a small percentage (<5%) of all surface engineering techniques are currently using laser based surface modifications (Singh & Harimkar, 2012). Limitations such as poor coupling of Al with laser, surface defects and poor uniformity are common in LSE of Al alloys. A defect free coating with higher hardness, wear and corrosion resistance is a general requirement regardless of modification technique utilized. Researchers have mainly focused on the optimization of the process parameters and design of cladding materials for achieving the desired properties.

The tribological behavior of coating materials has been difficult to be comprehended just by taking into account the surface hardness only. As hard coatings do not sufficiently reduce friction coefficient and may not provide protection from the adjacent surface asperities (Holmberg, 1992). Whereas, in wear, rougher and hard particles from the sliding surface could be easily peeled off and thereby causing aggressive abrasive wear (Kato, 2000). Hence, it is thus quite important to adopt solid lubricant coatings technology or additives that may reduce friction, wear, protect opposing surface and improve mechanical properties of coatings. Under the tribological load, the risk of damage due to inaccessibility of the lubricant can be drastically reduced (Aouadi et al., 2014; Arslan et al., 2015) or eliminated by introducing solid lubricants (Bao et al., 2006) in the material system.

1.2 Problem Statement

Aluminium and its alloys are extremely difficult to be laser engineered owing to their high reflectivity and poor energy absorption. Albeit being in the category of light metals, these alloys gave great potential in replacing steel based heavy components, which are operating under tribological load. Hence, improving the mechanical and tribological properties of near-surface regions of Al-alloys will certainly boost their usage in production and manufacturing of lighter components. Researchers have introduced the laser surface engineering technique but have failed to register lower friction coefficient on hard metal matrix based coatings. Hence, to produce harder and wear resistant coatings in addition to lower friction coefficient is the primary goal that is achievable through the addition of solid lubricants that have never been investigated on Al-alloys.

1.3 Research Objectives

The aim of the present work is to produce in a hybrid metal matrix composite coating (HMMC) layer in the order of micrometres to improve the surface hardness, wear resistance and friction coefficient of aluminium alloys. The composite layer will be expected to exhibit higher hardness and superior wear resistance when compared with the substrate. Moreover, the effects of laser processing parameters and additives (graphite and TiO_2) content on tribo-mechanical properties of Ni-WC MMC coating will be examined.

The objectives of the present study are:

1. To systematically optimize the coating deposition parameters such as laser power, scanning speed and defocus distance by Taguchi optimization and Pareto ANOVA method for the deposition of metal matrix composite (MMC) coatings.
2. To investigate and characterize the effect of solid lubricant additives graphite and TiO_2 on friction and wear resistance of hybrid metal matrix composite (HMMC) coatings.
3. To identify and compare the change in wear mechanism of solid lubricant doped HMMC and un-doped MMC coatings along with the substrates.

1.4 Framework of Thesis

With the introduction of **Chapter 1** wherein, the basis of the this thesis has been defined, it has been succeeded by **Chapter 2**. This chapter provides the theory and literature review to provide an overview of the recent developments in the field of Laser based surface modifications of Aluminium alloys. Further to this, as to how the application of additives such as solid-lubricants affect the tribo-mechanical performance

of laser based metal matrix composite coatings is further discussed. A brief overview of the design of experiment through Taguchi technique has been summarized. Henceforth, a complete summary of the way forward that we obtain from the conducted literature review have been concisely pointed out.

Chapter 3, introduces the coating materials that have been utilized for the fabrication of composite coatings. Their general mechanical properties have been summarized. This chapter further outlines the experimental fabrication techniques and the mechanical and tribological characterization procedures, utilized in the present research work. The working principle of instruments that were used for the characterization of materials have been briefly outlined.

Chapter 4, reports on the fabrication and characterization of MMC based composite coatings. This chapter presents a systematic study of the optimized combinatorial scheme to achieve surface hardness and roughness. Furthermore, the tribological performance of MMC based on pin-on-plate tribometer has been investigated and compared. Later on, in the end, a comparision between wear mechanisms of MMC and HMMC coatings are given.

Finally, the research work reported in this dissertation is summarized in **Chapter 5**. An outlook on future research directions and the current gaps available in this field are also suggested in this section of the chapter.

CHAPTER 2: LITERATURE REVIEW

This chapter details the literature review and theory related to the Laser surface modification of various aluminium alloys. Modern types of the MMC and HMMC coating used in the various aerospace, automotive and petroleum sectors have been presented along with a brief review of the physics underlying the operating mechanism. A brief overview of the laser processing parameters of the composite coatings and modes/principles of laser operation have also been explained, with special focus on laser material interaction. The important aspects which are required to be considered while selecting appropriate MMC coating materials and HMMC solid lubricants, have also been discussed.

2.1 Introduction to Lasers

Laser (Light Amplification by Stimulated Emission of Radiation) is the most influential invention of the 20^{th} century (Zhong & Liu, 2010). The physics behind laser that is based on quantum mechanics those are relatively complex and have been furnished in Ref (Toyserkani et al., 2004). Laser is an electromagnetic radiation including a very broad range of wavelengths ranging from infrared up to ultraviolet, which is monochromatic and is thus able to propagate photons in a straight direction with extremely high coherency and hence, it has been always the hub of attention due to its unexampled applicability in diverse applications. Lasers are capable of delivering very high (110 kW) to extremely low (some milliwatt) focused output power with a precise temporal (spatial) distribution in addition to very accurate spot dimension on almost any material or any kind of medium.

Albert Einstein at initially developed the premise of laser hypothesis, which was along these lines affirmed by trial works of Ladenburg and Kopfermann (Milonni, 2015). Maiman was the creator of the principal laser gear with Ruby medium (Maiman, 2002). Later, an assortment of more current era laser are comprising of: CO_2 gas laser, semiconductor, Nd:YAG, dye laser not withstanding numerous different sorts of more effective lasers were composed and made which had much better unwavering quality, vitality proficiency with lesser size (S. Liu et al., 2015) . In late 1970s, the mass businesses saw the coming of effective laser machines, which made the modern methods, for example, welding, cutting, melting, and boring straight forward (Duley, 2012). The power density range for different laser-material handling is given in Figure 2.1. The continually propelling pattern in laser innovation improvement prompted fruitful utilization of this innovation in different fields, for example, cladding, coating, alloying notwithstanding thin film deposition, which has been presented in Figure 2.2.

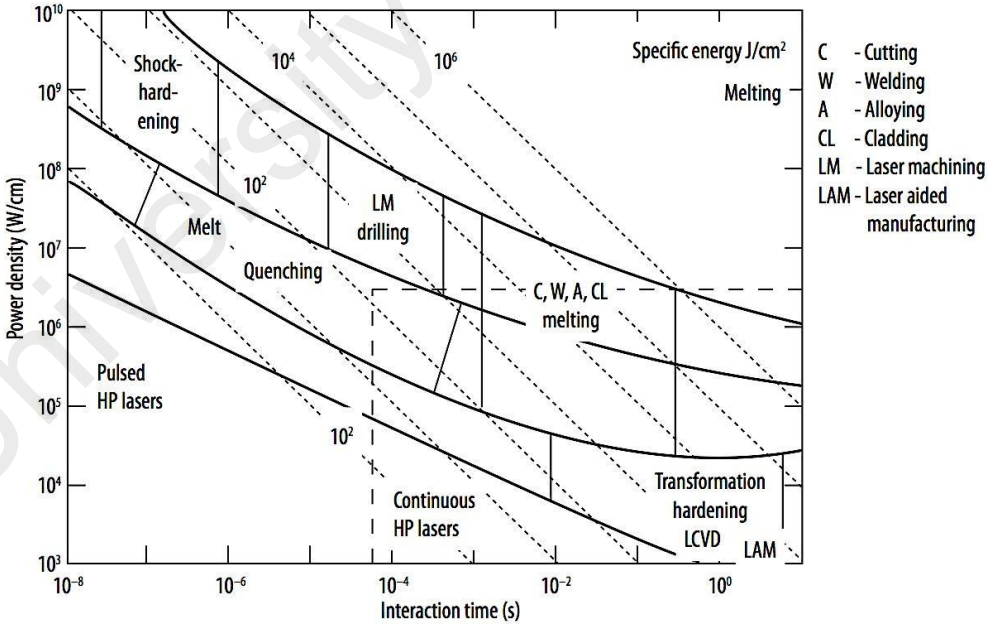

Figure 2.1: The power density range for various laser-material processing and joining (Majumdar & Manna, 2003)

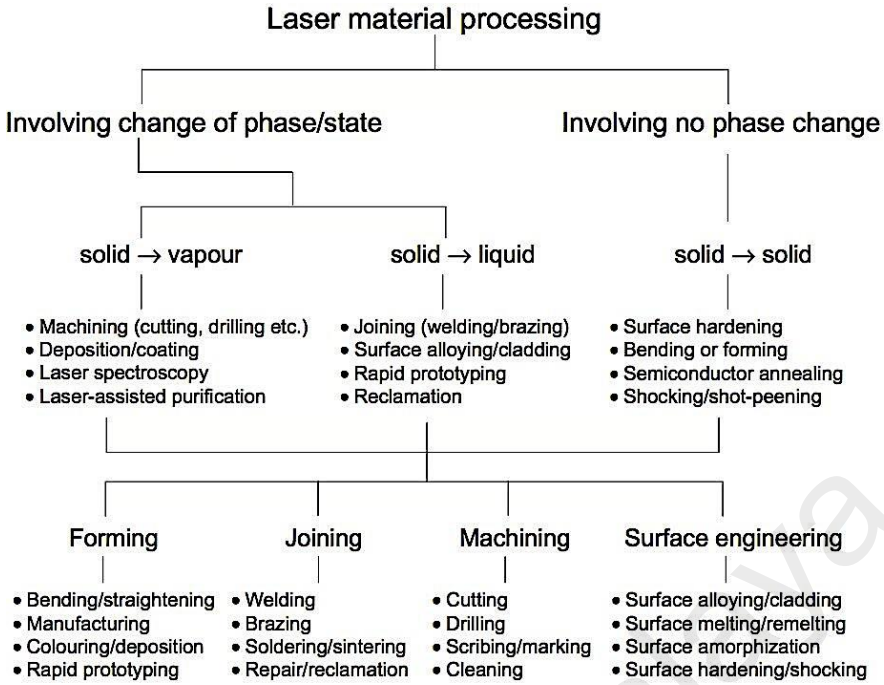

Figure 2.2: Application of laser in various manufacturing processes (Majumdar & Manna, 2003)

2.1.1 Construction of Lasers

A typical laser is made up of the following three major components as it is shown in Figure 2.3:

1. The gain medium, which acts as a means to amplify the light.

2. The pumping source which excites the gain medium to an amplified state.

3. An optical delivery/feedback mechanism.

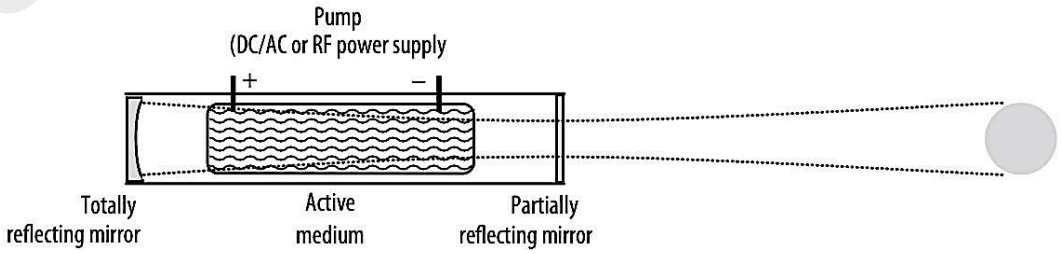

Figure 2.3: The structure of typical laser equipment (Majumdar & Manna, 2003)

The further components in charge of cooling the mirrors, manipulating the targets in addition to guiding the laser beam are indispensable as well in order to assist the materials processing. The quantum mechanics principles state that when an external energy (stimulus) is supplied to the atom, the irradiated atom obtains an excited state (Silfvast, 2004). This excited atom can return spontaneously to the ground level (E1) from the higher energy level (E2) by emitting this difference in energy states as a photon with a frequency equal to (ν):

$$v = (E_2 - E_1)/h \tag{2.1}$$

where "h" is the Planck's constant. This phenomenon is known as spontaneous emission. The photon emitted by spontaneous emission may in turn excite the secondary atom and stimulate it to emit a photon by de-exciting it to a lower energy state. This phenomenon is called stimulated emission of radiation. The latter leads to generation of radiation, which is coherent and has the identical wavelength, phase and polarization leading to generation of laser beam. Moreover, the optical resonator causes the generated light parallel to its axis, to be reflected forth and back through the medium (Steen & Mazumder, 2010). If the light is in fact amplified due to the aforementioned process, and if the gain is equivalent to the round trip loss within the resonator, then both the resonator and amplifier are at the threshold for laser beam production. The produced light in the excited resonator travelling parallel to its axis is amplified multiple times. A small portion of this light is merely released in each pass through a partially transparent mirror. The mirror system positioned in the resonator is a cavity consisted of a partially transmitting mirror at one side in addition to a completely reflective mirror on the other side. In laser equipment, this cavity is occupied by a pumping source and a medium. Despite the main responsibility of the optical resonator, it can also convert the laser radiation into a monochromatic and unidirectional beam.

2.1.2 Classification of lasers

Laser (Light Amplification by Stimulated Emission of Radiation) is the most influential invention of the 20th century. Based on the laser type and required wavelength, the medium of laser can be either in a gaseous, liquid or solid status. Various kinds of laser equipment are typically named according to the state or physical characteristics of their medium, upon which they can be classified into 4 major categories namely: solid state, liquid, gas, in addition to semiconductor (glass) lasers. In the literature, mainly four kinds of high power lasers with optical wavelengths ranging from 248 nm to 10.6 μm are employed. These are CO_2 lasers, neodymium-YAG (Nd: YAG) laser, high power diode laser (HPDL) and fiber laser. The principal difference among these types of lasers is the medium utilized in generating stimulated emissions. In CO_2 lasers, light amplification is achieved by gas discharge which acts as the laser gain medium. Surface processing by these lasers results in larger heat affected zones (HAZ). In Nd: YAG lasers, light amplification is achieved by using ionized neodymium (Nd) and crystal of yttrium-aluminum-garnet (YAG). Nd is the light source and YAG is the host. In HPDL, diodes are used to amplify the light but they have poor beam qualities (L. Li, 2000). The most common diode lasers are GaAs and Al_xGa_{1-x}. Lastly, in fiber lasers, the active gain medium is doped in optical fiber. Some of dopant materials are erbium (Er), dysprosium (Dy), neodymium (Nd), praseodymium (Pr), thulium (Tm) and ytterbium (Yb). As compared to other laser types, fiber lasers produce excellent beam quality (beam parameter product) owing to use of smaller diameter fibers.

2.2 Lasers in Coatings Technology

Laser (Light Amplification by Stimulated Emission of Radiation) is the most influential invention of the 20th century (Zhong & Liu, 2010). LSC has been around for more than 35 years and has numerous advantages in the field of coatings technology (Dubourg & Archambeault, 2008). It offers the formation of unique microstructures and controlled localized heating which leads to smaller heat affected zone (HAZ) and induces lesser thermal stresses (Watkins et al., 1997). In addition, the flexible cladding process, it offers sound fusion bonding with the surface, high deposition rates, and fine quench microstructures with near isotropic mechanical properties (Weng et al., 2014). LSC process is often employed in repairing components and presents tremendous potential for producing protective surfaces (Clare et al., 2012; Nowotny et al., 2015).

In laser surface cladding (LSC), an alloy or composite layer is fused onto the surface of a substrate with the assistance of a scanning laser beam Figure 2.4. The position of the laser beam can be controlled with the help of scanning galvo mirror system, whereas a CNC based or a 3 stages motorized servo controller is utilized for controlling the axis of the worktable. LSC process can be performed out in two ways. In one process, clad material is preplaced onto the substrate as a powder bed and the laser beam scans the powder bed with some degree of overlapping between each bead to form a surface. Alternatively, the powders can be plasma sprayed or electroplated, or fed by wire followed by laser melting (Hung & Lin, 2004; Mendez et al., 2014). The material can also be added by a feeding wire system or else the powder mixture can be blown directly into the melt pool. Though the coating remains chemically different from the substrate, however in order to obtain higher metallurgical bond strength, some degree of reactions and mixing in the interfacial region becomes vital (Sexton et al., 2002). Owing to the application of a Gaussian laser beam energy mode, the thickness of the laser clad

is higher at the centre than towards both sides of the track (Lei et al., 2015). Clad morphology can be segregated in three regions; the clad zone (CZ), the heat affected zone (HAZ) and the unaffected zone or substrate (Buchbinder et al., 2015). The microstructure as well as the composition of the coatings strongly depends on the degree of mixing, which is governed by convection, diffusion, and cooling rates during liquid-to-solid and solid-to-liquid phase transformation (Bergmann & Mordike, 1986; Mondal et al., 2014). LSC requires irradiation of high energy density laser beam (10^2 – 10^4 W/mm^2) on material surface within a very short interaction time (10^{-3} – 1 s). During LSC process, due to the application of extremely high power density, the melt pool temperature can soar as high as 2000 °C (Elhadj et al., 2014). The sudden temperature increase followed by abrupt cooling produces very high thermal gradients (Farahmand & Kovacevic, 2015). These higher cooling rates, up to 1011 K/s results in the formation of hard phases, induces microstructural refinement and leads to solid solution strengthening (Draper & Poate, 1985a). Hence, the parameters controlling these mechanisms are of paramount importance to the laser surface cladding process. Figure 2.4(b), the probable process control parameters on clad quality has been studied (Mondal et al., 2011) and presented in the form of a cause–effect (Ishikawa) diagram. Clearly, the quality of LSC process greatly relies upon a variety of factors such as the laser power, traversing speed, powder feed and spot size etc. It is the combination of some of these parameters that controls the solidification rate and subsequently results in grain refinement and formation of non-equilibrium phases in the cladding. Therefore, optimization of cladding process parameters is important aspect in-terms of coating quality.

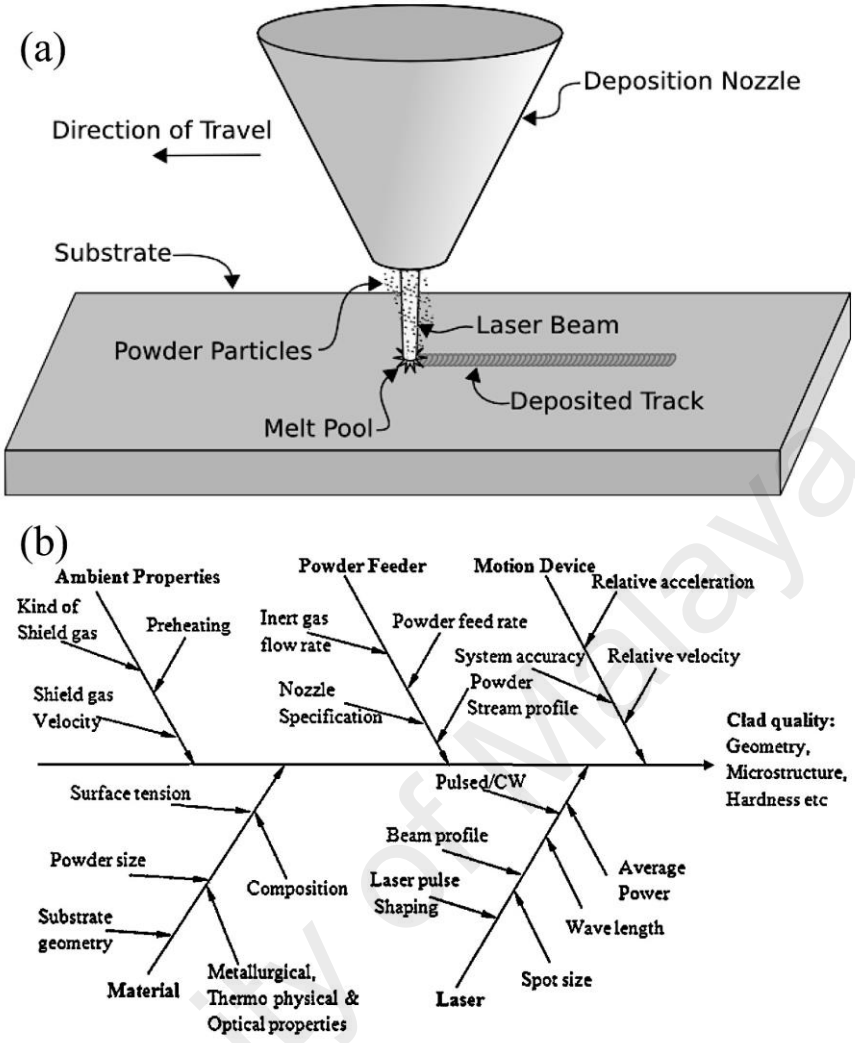

Figure 2.4: (a) Schematics of the LSC process (b) an Ishikawa diagram of LSC (Mondal et al., 2011)

2.3 Laser Surface Modification of Aluminium Alloys

Based on the interaction of materials with high speed photons, laser surface modifications can be classified into five major categories, which comprises of i) laser surface melting, ii) laser surface alloying, iii) laser composite surfacing, iv) laser surface cladding and v) laser shock peening. Laser based surface modifications either involves melting of the substrate with or without filler material except for shock peening. These processes necessitate the use of shielding gas to prevent oxidation, use of filler (except in laser surface melting) and crack stabilizers (during rapid

solidification). The aforementioned processes have some merits and demerits and a suitable process should be approached depending on the properties desired.

Treating Al alloys with laser possesses major constraints of lower melting point of aluminum and the poor absorption of electromagnetic radiation (7%) due to high density of free electrons present, which strongly relate to surface conditions (Touloukian & DeWitt, 1970). Absorptivity relies on band structure, the incident beam wavelength, resistivity of metal and is also a function of the size and nature of the plasma present above the melt pool, concentration and phase of volatile alloying elements in the metal and surface geometry (Miotello & Ossi, 2010). By modifying the surface geometry through increasing surface roughness, higher energy absorption can be attained by virtue of earlier development of keyhole, which further contributes to multiple reflections of the laser beam occurring in the cavities (Ang et al., 1997). Hence, prior to laser processing, sand blasting and rough grinding are performed in order to step-up incidence beam absorption and remove oxide scale. Dispersion of oxide film is essential as it may lead to the formation of a molten pool of Al enclosed in a skin of oxide, thereby promoting additional porosity. Figure 2.5 presents energy absorption of aluminum after various surface treatments signifying considerable increase in energy absorption in case of anodized and sand blasted specimens. Another alternative method to improve laser energy absorption is coating graphite and black paint layer. Apart from enhanced energy absorption, the black paint layer vaporizes and thermal effects are reduced when the work piece surface is exposed to laser beam irradiation (Peyre & Fabbro, 1995). When laser beam scans across an absorber coating such as graphite on a metallic substrate, the absorber may evaporate or burn-off (Kek & Grum, 2010). However, unused graphite from the sample is easier to remove through acetone (Carey et al., 2007). The application of the absorber layer for optimal energy absorbance requires optimization of graphite coating thickness. Depending on the processing

parameters, when graphite is added in excessive amounts, they may survive the laser radiation and can be incorporated in the coating as black particles (D'Amato et al., 2014b).

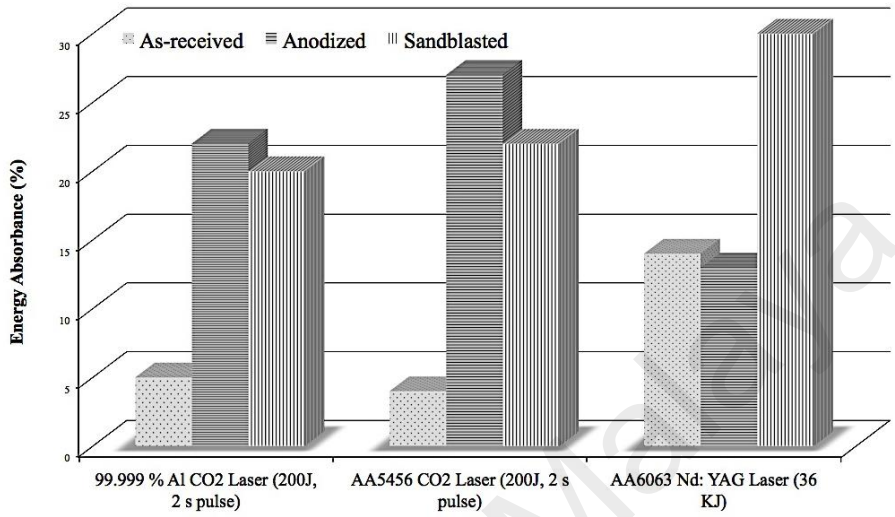

Figure 2.5: Energy absorption of the laser beam for pure aluminum, AA5456 and AA6063 (%).

Since aluminum is highly sensitive to lasing environment, hence various processing factors should be taken into consideration. For example, aluminum is highly susceptible to hydrogen porosity and reacts easily with active gases like oxygen, water vapors in the atmosphere, adsorbed or present as hydrated oxide films (Hatch & Aluminum, 1984). Therefore, careful selection of shielding gas is essential as it may preclude the formation of oxides that may aggravate metallurgical properties. The resulting plume dynamics due to inert environment provided, standoff distance and gas flow rates affect the quality of processing (Sibillano et al., 2006). Another issue in laser material processing is hot and cold cracking as a consequence of rapid solidification. Several researchers have prevented crack formation by employing an additional heat source to decrease thermal shock, while some have defocussed the laser beam (Brückner et al., 2007). In addition, flux and rare earth elements (RE) powders are utilized, which on

application of plasma are activated within the molten pool to restrict surface tension gradients (M. Wang et al., 2011). Similarly, crack stabilizers such as TiO_2 (Ouyang et al., 2001) , CeO_2 (Tao et al., 2000) and La_2O_3 (K. L. Wang et al., 2001) are added to stabilize microstructural evolution and prevent cracking. The extent of issues highlighted above is not complete but is an indication that considerable research is required for achieving defect free optimal coatings.

2.3.1 High Power Lasers suitable for surface modification

In the literature, mainly four kinds of high power lasers with optical wavelengths ranging from 248 nm to 10.6 μm are employed. These are CO_2 lasers, neodymium-YAG (Nd: YAG) laser, high power diode laser (HPDL) and fiber laser. The principal difference among these types of lasers is the medium utilized in generating stimulated emissions. In CO_2 lasers, light amplification is achieved by gas discharge which acts as the laser gain medium. Surface processing by these lasers results in larger heat affected zones (HAZ). In Nd: YAG lasers, light amplification is achieved by using ionized neodymium (Nd) and crystal of yttrium-aluminum-garnet (YAG). Nd is the light source and YAG is the host. In HPDL, diodes are used to amplify the light but they have poor beam qualities (L. Li, 2000). The most common diode lasers are GaAs and Al_xGa_{1-x}. Lastly, in fiber lasers, the active gain medium is doped in optical fiber. Some of dopant materials are erbium (Er), dysprosium (Dy), neodymium (Nd), praseodymium (Pr), thulium (Tm) and ytterbium (Yb). As compared to other laser types, fiber lasers produce excellent beam quality (beam parameter product) owing to use of smaller diameter fibers (Richardson et al., 2010).

Figure 2.6 presents the reflectance of processed aluminum under various radiation wavelengths (L. Li, 2000). Aluminum alloys are very difficult to be laser engineered successfully for the reason that high reflectivity results in poor coupling with the laser beam. Therefore, normal incidence is not employed in order to avoid the risk of beam

reflection, which may cause damage to collimator, mirrors and laser cavity (Dubourg, Pelletier, et al., 2002). Al alloys absorbs the laser energy more readily at shorter laser wavelength. At shorter wavelengths, the more energetic photons can be absorbed by a greater number of bound electrons resulting in higher absorption (Quintino et al., 2007). Clearly, the selection of laser is thus vital. Nd: YAG, HPDL and fiber lasers deliver far better coupling with aluminum than the CO_2 laser (λ = 10.6 µm) due to the delivery of shorter wavelengths of radiation (L. Li, 2000). It is worth mentioning that, diode pumped fiber lasers often termed as "greener lasers", offer multiple advantages, including small beam focus diameters providing high power densities, precise fiber delivery system, compact design, and robust installation.

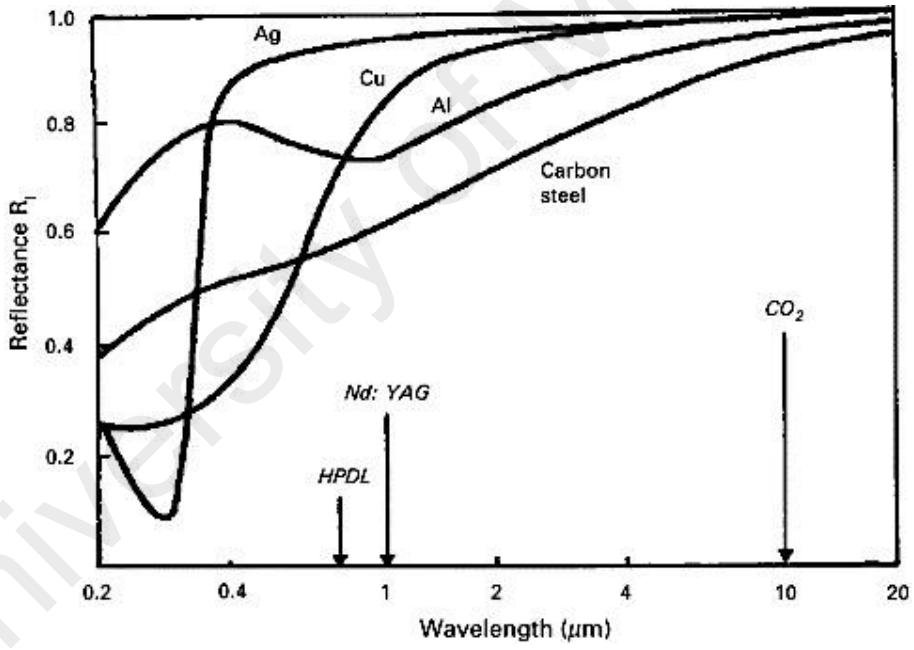

Figure 2.6: Spectral reflectance of aluminum and various other metals. (Reprinted with permission from Elsevier, License no: 3575990476470) (L. Li, 2000)

2.3.2 Laser Surface Melting (LSM)

LSM requires irradiation of high energy density ($10^2 – 10^4$ W/mm^2) on material within a very short interaction time (10^{-3} – 1 s) to cause localized melting at the surface. The schematic of LSM process is illustrated in Figure 2.7. Laser is scanned with a certain percentage of overlap to cover a larger area of surface with microstructural changes confined to near surface regions (Fariaut et al., 2006). The aspect ratio (depth to width ratio) of melt region and grain size (dendrite arms spacing) is a function of beam diameter (irradiation area), scanning speed and applied power. Properties of LSM zone are dependent on the substrate's material composition, microstructure, laser power applied and spatial distribution of energy. The nature and extent of laser material interaction is dictated by thermo physical properties like thermal conductivity, temperature gradients, melting point, absorptivity and surface tension (Elhadj et al., 2014). In addition the amount of material hardening is dictated by the cooling rates at the liquid/solid boundary, the extension of the solid solubility and concentrations of alloying elements present (Bergmann & Mordike, 1986). The Nd: YAG, CO_2 and Excimer lasers are generally utilized with an overlap of greater than 25% to achieve a maximum melt depth of around 2 mm. Greater overlap is required in order to obtain a surface with uniform melt depth. The resulting microstructure and surface properties in the coincided region remain different. Transforming the shape of the incident beam profile can alter the laser beam energy distribution to attain preferred shapes of the molten pools, sustain microstructural and compositional uniformity (Fariaut et al., 2006). A fine-grained homogenous material is expected to resist micro fracturing in tribo-chemical wear (Allen & Ball, 1996). So far, Al alloys containing Fe, Si, Cu and Mg are found to exhibit higher micro-hardness after LSM treatment as showed in Figure 2.8.

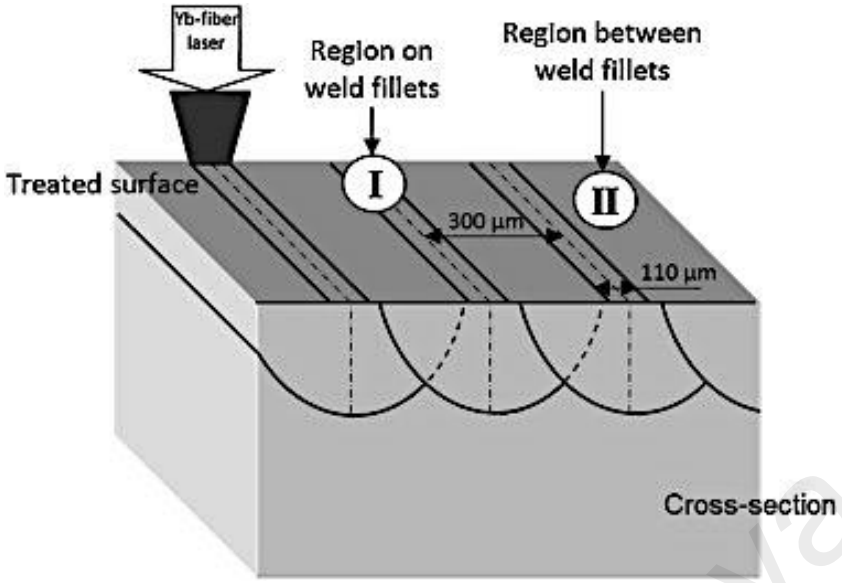

Figure 2.7: Schematics of LSM I – in the area of the laser scanned filet and II – the area between laser-scanned filets. (Reprinted with permission from Elsevier, License no: 3575150149465) (Pariona et al., 2013)

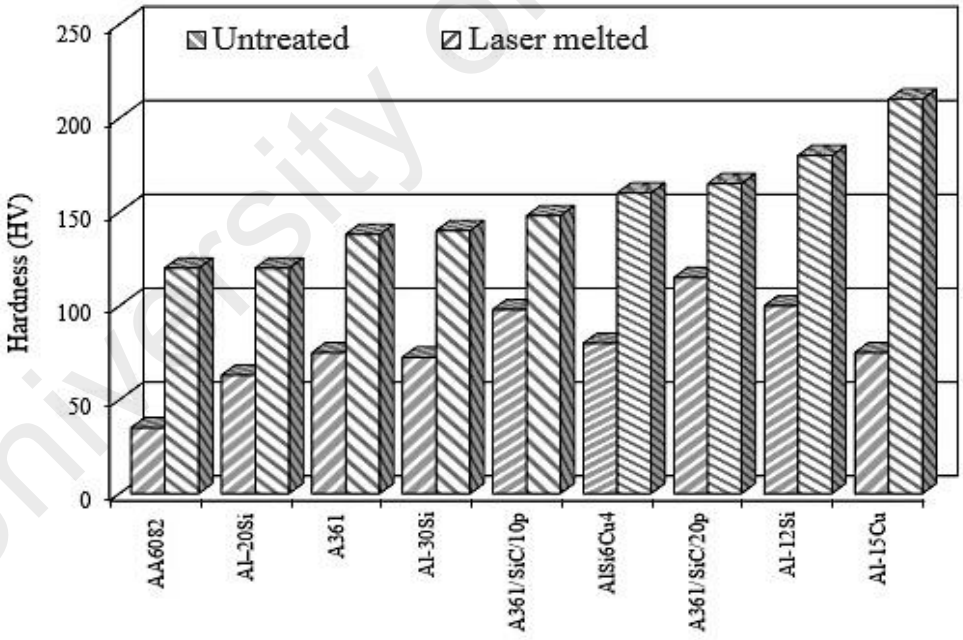

Figure 2.8: Vickers hardness of various Al alloys after LSM treatment.

2.3.3 Laser Surface Alloying (LSA)

LSA is a directed energy beam assisted surface alloying technique wherein various alloying elements can be inserted into the melt pool resulting in formation of alloyed zone. With a very short laser material interaction time (10^{-3} – 1 s), the alloyed zone produced on the surface remains confined to a very shallow depth The alloying element in the melt pool can be added in two different ways: direct injection (fine powder, powder slurries or wire) and preplaced coating (such as foils, powder paste). Figure 2.9(a) and b respectively. Laser beam irradiation (10^2 – 10^4 W/mm^2) with very high energy density and higher cooling rates, up to 1011 K/s results in formation of hard phases, microstructural refinement and solid solution strengthening (Draper & Poate, 1985b). The improvement in micro hardness with the addition of various alloying elements is illustrated in Figure 2.10**,** indicating hardness of around 1000 H_v attained with nickel based alloy additions. The microstructure as well as the composition of the coatings strongly depends on the degree of mixing, which is associated / governed with convection, diffusion, and cooling rates during liquid-to-solid and solid-to-solid phase transformation. In the following sections, the resulting mechanical properties of laser surface Al alloys are discussed.

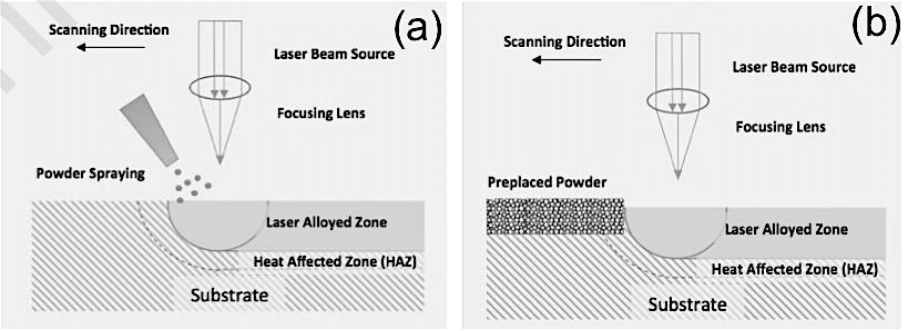

Figure 2.9: Schematics of LSA: (a) direct injection of powder and (b) preplaced powder technique. (Reprinted with minor modification taking permission from Springer, License no: 3575790741638) (Singh & Harimkar, 2012)

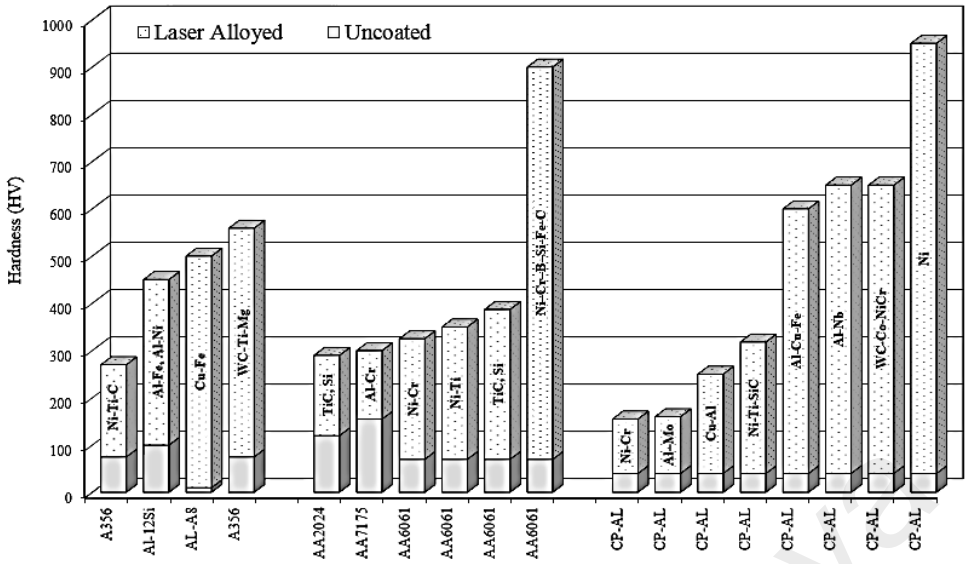

Figure 2.10: Vickers hardness of various Al alloys after LSA treatment.

2.3.3.1 LSA with addition of Nickel (Ni) and Ni based Alloys

The tribological characteristics of automotive aluminum A356 cylinder cast alloy treated by LSA with Ni and Ni-Ti-C compositions were investigated in a study (D'Amato et al., 2014a). Ni-Al intermetallic compound was formed when Ni was added. Al-Si-Ti and Al-Ni intermetallic compounds together with in-situ hard particulates of TiC were formed when Ni-Ti-C was added. As showed in Figure 2.11**,** supplementing more powder flow rate resulted in higher hardness and wear resistance. In another work (Chuang et al., 2006), self fluxing Ni-Cr-B-Si coating was developed on Al matrix resulting in 18 times higher hardness in Al-Ni-Cr amorphous regions. Other authors (Man et al., 2007), studied the corrosion behaviour of AA6061 alloy treated by LSA with Ni-Cr-B-Si composition. The significant improvement in corrosion and protection potential was related to the presence of Ni in the alloyed layer. Wear resistance is primarily decided by the response of the various alloy phases, either independently or in combination, to the volume fraction, size and mean free path of abrasive particles. Another research work (Mabhali et al., 2012) achieved 82%

enhanced wear resistance by alloying with 20 - 40 wt% Ni, Ti and 40 wt% SiC compositions. Hardness portrayed no direct correlation with wear behaviour, which revealed intense plastic deformation and micro fracture of intermetallic phases. Samples containing Ti_3SiC_2 that is known to have higher damage tolerance and Young's modulus along with Al_4SiC_4 having high hardness (1200 HV) showed the highest wear resistance. These phases promoted larger Al mean free path resulting in wear characterized by plastic deformation. Another work (Das, 1994), reported the effect of beam defocus distance when alloying pure aluminum with nickel. The surface roughness is generated due to the formation of ripples. The height of these ripples is a function of the fluid flow due to shear stresses in the melt pool caused by gradients in temperature and surface tension. It was demonstrated that with increasing defocus distance, the power density decreases, and ripples height decreases, which results in a decrease in surface roughness after solidification. The defocussing of laser beam assists in formation of greater concentrations of alloying elements in the melt pool as the temperature gradient falls, causing a decrement in surface tension gradients.

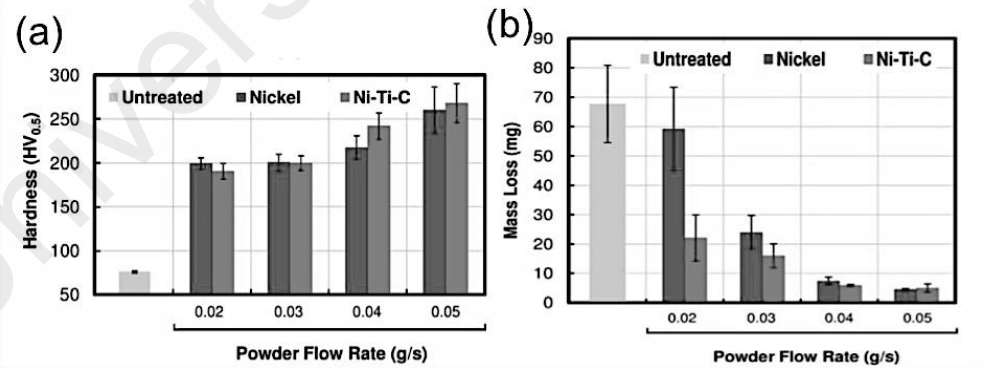

Figure 2.11: Effect of powder flow rate on: (a) surface hardness and (b) mass loss of Ni and Ni-Ti-C alloying as obtained by pin-on-disk wear testing. (Reprinted with permission from Elsevier, License no: 3575180604467) (D'Amato et al., 2014)

2.3.3.2 Addition of Chromium (Cr) and Cr based Surface Alloys

Aluminum alloys exhibit poor fretting wear resistance in machines and aerospace structures. In one study authors (Fu & Batchelor, 1998), used Cr-30Ni for LSA of AA6061 grade alloy and studied the fretting wear resistance. When exposed to fretting conditions, laser treatment prevented excessive ploughing and scratching subsequently mitigating abrasive wear. Similarly in another work (A. Almeida et al., 1995), reported the outcome of chromium (Cr) alloying on α-Al and aerospace AA7175 alloy to investigate corrosion behavior. Formation of passive chromium oxide film delayed pitting and augmented corrosion resistance, thus promoting service life of aerospace alloy.

2.3.3.3 Addition of Copper (Cu) and Cu based Surface Alloys

Wear resistance is largely determined by the volume fraction of alloying phases present, particle size, dispersion, brittleness, and hardness of surface. In one research study (Dubourg, Hlawka, et al., 2002), Al-Cu alloying on pure Al (99.5% Al) surface by using CO_2 laser investigated. Followed by laser surface treatment annealing was carried out for 24 hr at 480°C to obtain a homogeneous microstructure. Raising Cu content up to 40% in the alloyed surface extended mechanical properties such as hardness, elastic modulus, and plasticity index. Subsequently, substantial improvement in wear was realized up to 27% of Cu content, which remained unaffected beyond this percentage.

2.3.3.4 Addition of Molybdenum (Mo) and Mo based Surface Alloy

The evolution of microstructures in LSA is a function of linear energy density supplied by the controlling power and adjusting traverse speed. One study investigated the mechanical and tribological properties of Al-Mo laser alloyed surface on α-Al substrate (Amélia Almeida et al., 2006). The microstructure of the alloyed region consisted of Al_5Mo intermetallic at lower speeds and exhibits transition from acicular morphology that changed to flower like morphology at higher speeds **(**Figure 2.12). In order to

calculate the elastic modulus, Fisherscope ultra-microindenter was employed and load-penetration curves were analyzed with applied loads in between 0.0004 and 0.1 N. Hardness of the Al-Mo coated layer ranges from 85 to 160 Hv and young's modulus varies from 84 to 92 GPa. The increase in Young's modulus was correlated with the higher volume fraction of fine equiaxed intermetallic compounds, which were found to have provided better wear resistance. Wear test using disk on plate configuration revealed main mechanism of wear in Al-Mo coated surface was adhesion, material transfer and oxidation, which are unlike to other laser coated alloys. Larger volume fraction of the intermetallic compounds is the reason postulated for a reduction in the wear rate.

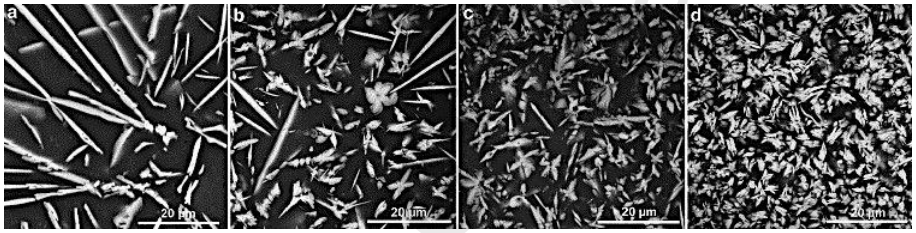

Figure 2.12: Evolution of microstructure of Al–Mo surface alloy remelted (a-d) under increased traverse speed. (Reprinted with permission from Elsevier, License no: 3575180909391) (Amélia Almeida et al., 2006)

2.3.3.5 Addition of Other Surface Alloying Systems

In several studies, the effects of WC-15Co-15NiCr alloy (Nath et al., 2012) and WC-2Ti-2Mg (Staia et al., 2000; Staia et al., 2001) have been investigated on laser alloyed Al substrate. It was reported (Nath et al., 2012), that microstructure, wear and corrosion resistance of pure Al treated by LSA with WC-Co-NiCr. The addition of 15 wt. % Co and 15 wt. % NiCr prevented WC dissociation and improved wettability. The alloyed surface possessed fine-grained microstructure and morphology changed from columnar at the near interface to dendritic and equiaxed towards the middle signifying CET transition. Carbides in the fine-grained Al matrix attributed to lower fretting wear rate

but resulted in higher friction coefficient (0.37) due to removal of softer aluminum matrix. Other authors (Staia et al., 2001) laser treated sand cast aluminum A356 alloy for cylinder bores using 96 wt. % WC, 2 wt. % Ti and 2 wt. % Mg at various transverse speeds, with the aim to avoid delamination wear. It was found that increasing the transverse speed contributed to lower wear rates.

2.3.4 Laser Surface Cladding (LSC)

In LSC, an alloy or composite layer is fused onto the surface of a substrate. Though the coating remains chemically different from the substrate, however in order to obtain higher metallurgical bond strength, some degree of reactions and mixing in the interfacial region becomes vital (Sexton et al., 2002). LSC process is often employed in repairing components and presents tremendous potential for producing protective surfaces. LSC process can be performed out in two ways. In one process, clad material is preplaced onto substrate as powder bed. Moreover, powders can be plasma sprayed or electroplated, followed by melting. Alternatively, material can be added by feeding wire or else the powder mixture can be blown directly in the melt pool. Clearly, the quality of LSC process greatly relies upon a variety of factors such as the laser power, traversing speed, powder feed and spot size etc. The combination of various parameters controls the solidification rate resulting in grain refinement and formation of non-equilibrium phase in the surface. The higher hardness obtained as are result with the addition of various metals and ceramics is presented in Figure 2.13. In the following sections, the process's microstructure, mechanical and tribological properties of different clad layers will be briefly touched upon.

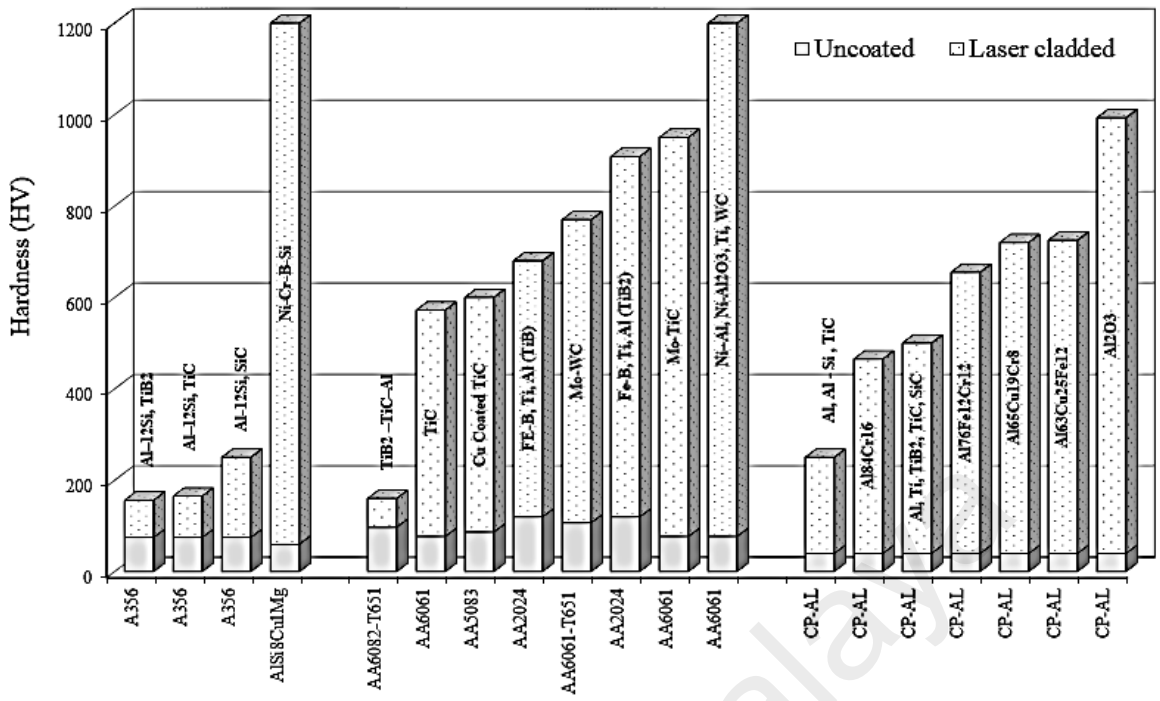

Figure 2.13: Vickers hardness of different laser claddings on aluminum alloys

2.3.4.1 Cladding of Metallic/Alloy Layer

LSC is advantageous in various repairing and maintenance applications (Dong et al., 2007). Figure 2.14 presents a typical example of laser cladding in automotive applications wherein the wear resistant Al-Si-Cu-Ni coating has been cladded to repair seats of automotive inlet and exhaust valves and piston ring grooves (Arnold & Volz, 1999). For repairing piston grooves, an oversized groove is cut followed by laser cladding and thereafter final geometry machining. In another work (A. H. Wang & Xie, 2001), the microstructure of Fe-Al bronze cladding layer on an Al-Si alloy was investigated. Analysis of the cross-section showed clad region and transitional region of the sample after LSC. A twin structure of needle-like and feathery appearance was observed in the clad region. Second phase particles of Cu_9Al_4 were seen in the matrix of clad region. Two areas are termed as transitional regions were identified. The region close to the substrate showed needle-like structure whereas the layer close to clad layer

possessed polygonal crystalline. XRD characterization revealed that the main phases resembling needle-like and polygonal morphology were Cu_3Al, Cu_9Al_4 and $CuAl_2$, α-Al respectively.

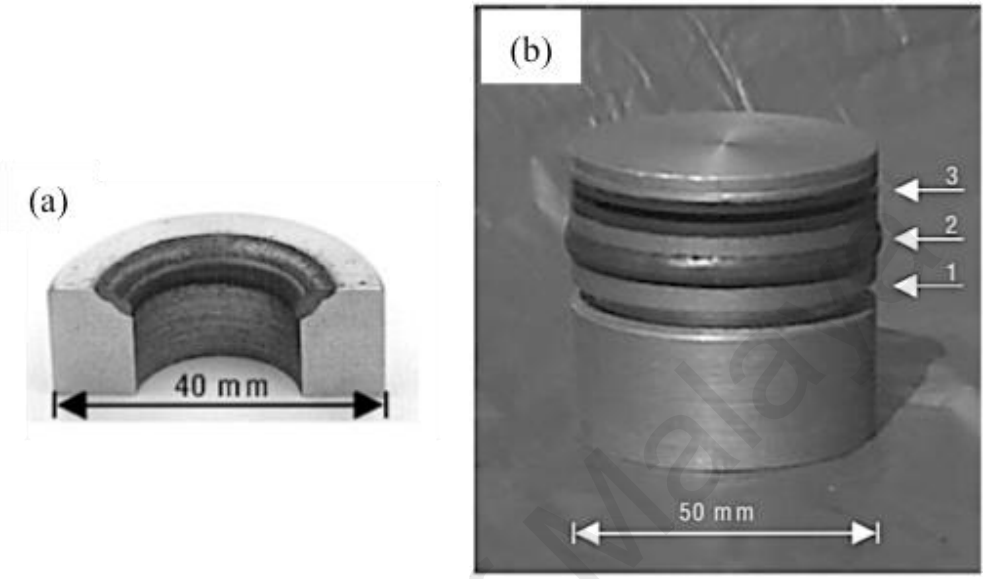

Figure 2.14: LSC application in a) valve seat repair and b) piston ring groove repair. (Reprinted with permission from Springer, License no: 3575181179845) (Arnold & Volz, 1999)

2.3.4.2 Cladding of Ceramic and Composite Layer

Current research in tribological performance of cladded Al alloys has concentrated entirely on wear resistance. The friction coefficient effects have not been incorporated due to detrimental effect of LSC on surface topography. However, there is a current proposition that a sound appreciation of tribological performance of LSC can only be realized by combining friction and wear analysis. Experience will be gained when a short list of materials that will give optimal wear resistance is specified for a given set of conditions. A few aspects of tribological testing conditions and wear enhancement brought by LSC are summarized in Table 2.1. Clearly, higher surface hardness of laser claddings (Figure 2.13**)** correlates with the substantial enhancement in tribological

properties. The wear resistance of laser clad is dictated by stability of added carbide particles. Ceramic particles such as carbides, borides etc. have the tendency to dissociate when high-energy laser beam strikes the particles. Some authors (Anandkumar et al., 2007), studied the influence of SiC cladding on Al matrix. SiC reacted with the substrate matrix when the processing temperature exceeds the melting point of Al inevitably resulting in formation intermetallic compound of Al_4C_3.

Table 2.1: List of various Al substrate laser surface cladding with different processing parameters.

References	Substrate	Coating	Substrate wear	Coating wear	Wear Resistance
(Wong et al., 2000)	AlSi8Cu1Mg	Ni-Cr-B-Si	10.5 mm^3	0.9 mm^3	10
(Anandkumar et al., 2011)	A356	Al–12Si-TiB_2	4.53 e-5 mm^3/Nm	2.65 e-5 mm^3/Nm	1.7
(Anandkumar et al., 2012)	A356	Al–12Si-TiC	4.5 e-5 mm^3/Nm	2.2 e-5 mm^3/Nm	2.1
(D'Amato et al., 2014a)	A356	Ni-Ti-C	68 mg	4 mg	17
(Anandkumar et al., 2007)	A356	Al-12Si-SiC	25 e-5 mm^3/m	4.3 e-5 mm^3/m	5.8
(Xu, Liu, Kan, et al., 2006)	AA2024	Fe coated B, Al, TiC	1.5 mg	0.1 mg	15
(Xu et al., 2007)	AA2024	FE-B, Ti, Al (TiB/Al)	0.060 mg/s	0.045 mg/s	1.3
(Tomida et al., 2001)	AA5083	Cu Coated TiC	3 e-4 mm^3/Nm	5 e-5 mm^3/Nm	6
(Katipelli et al., 2000)	AA6061	TiC	Seizure	Seizure	-

Table 2.1: continued

References	Substrate	Coating	Substrate wear	Coating wear	Wear Resistance
(Man et al., 2004)	AA6061	Ni–Al, Ni-Al_2O_3, Ti, WC	540 mg	20 mg	27
(Chong et al., 2002)	AA6061	Mo-TiC	0.45 g	0.016 g	20-28
(Chong et al., 2001)	AA6061-T651	Mo-WC	0.1982 gm	0.0031 gm	64
(Ravnikar et al., 2013)	AA6082-T651	TiB_2–TiC–Al	2.5 mm^3	0.22 mm^3	8
(Huang et al., 2008)	AA7075-T6	Al_2O_3	178.5mg/s	27.9 mg/s	10
(Dubourg et al., 2005)	CP-AL	Al, Al-Si, TiC	35 mm^3/m	0.73 mm^3/m	48
(Huang et al., 2008)	CP-AL	Al_2O_3	36.5 mg/s	5 mg/s	7
(Uenishi & Kobayashi, 1999)	CP-AL	Al, Ti, TiB_2, TiC, SiC	120 e-14 m^2/N	11 e-14 m^2/N	10

Formation of Al_4C_3 deteriorated the anticorrosive properties of the composite layer. Thus, to overcome this difficulty, Al-12Si matrix was incorporated instead of pure Al matrix. Experimental results implied that preplacing powders resulted in higher wear resistance as greater concentration of SiC particles was incorporated than those in laser assisted powder injection. As in the case of SiC, WC particulates have good strength, higher hardness and superior stability at higher temperatures. Some authors (Chong et al., 2001), preplaced 20 wt% Mo and 80 wt% WC powder to promote abrasion resistance of AA6061 to exceptionally 40 folds. Wettability and bond strength of WC with Mo-Al matrix was assisted by the formation epitaxially grown W_2C dendrites on the surface of partially melted WC **(**Figure 2.15(a)). Uniformly distributed hard particulates limited SiC abrasive ploughs and resisted micro cutting process. Whilst, it was revealed that 100% WC particles exhibited exceptional wear resistance, however owing to potential of severe cracking and coating peel off in weak overlapped regions **(**Figure 2.15(b) and (c)), the clad layer was not recommended for long term wear applications.

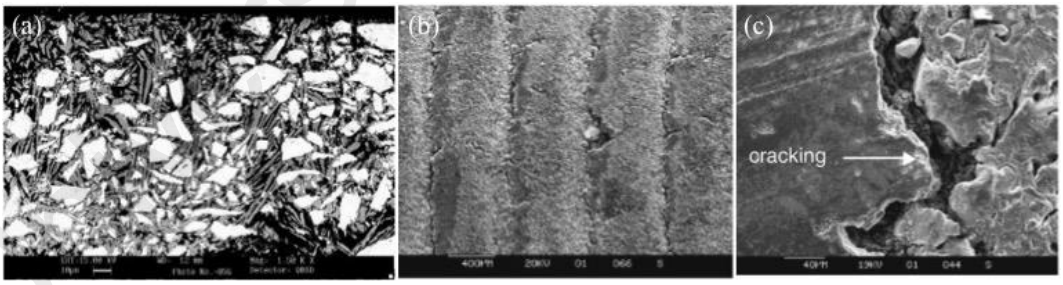

Figure 2.15: SEM image of a) cross sectional microstructure 20 wt% Mo and 80 wt% WC laser clad, (b) 100 wt% WC cladded wear track and (c) magnified view of cracks on wear track. (Reprinted with permission from Elsevier, License no: 3575820558488) (Chong et al., 2001)

In-situ cladding has been reported to overcome the problem of chemical dissociation of ceramic phases. In situ carbide dispersion was carried out during cladding by forming a

paste of Ti, C, and W on an AA6061 surface (Man et al., 2004). Using Nd: YAG laser Ni-Al and Ni-Al_2O_3 powders were delivered by a nozzle during LSC process. Exothermic reactions of Ni-Al, W-C and Ti-C expedited the cladding to produce homogeneous distributions of fine dendrite phases and white intermetallic particles in the Ni-Al matrix. Owing to higher hardness of the formed TiC, WC and Al_2O_3 in Ni-Al intermetallic matrix, the wear performance promoted to around 27 times. Apart from TiC and WC, TiB_2 owing to its extremely hard nature has been employed in improving wear resistance of automotive aluminum alloys. Automotive components such as brake rotors, pistons, cylinder head and liners and engine blocks are now reinforced with ceramic particulates. In another in situ process (Xu, Liu, Kan, et al., 2006), a powder mixture of Ti, Al and Fe coated B to clad AA2024 alloy was used. TiB_2, Ti_3B_4, Al_3Ti, Al_3Fe particles were identified in α-Al matrix. No clear boundary was observed between the substrate and clad layer, which indicated excellent metallurgical bond. Increment in hardness of the clad layer is correlated with the dispersion of TiB_2 and Ti_3B_4 particles in the matrix with the contribution of intermetallic Al_3Ti and Al_3Fe compounds.

2.3.5 Laser Composite Surfacing (LCS)

In LCS, a composite layer is formed by the addition micro and nanometer sized ceramic particles in the melt zone created by the laser beam. LCS is carried out by either blowing powders into the melt pool or by pre-placing powder mixtures onto the substrate. For reinforcing nano-scale particles, the blown injection method remains unsuitable as higher kinetic energy of particles moves the particles away from the irradiated area and particles float to agglomerate. The maximum depth of penetration of micro sized particles is often less than half of total melt depth. The preplaced ceramic powders having high absorption coefficients and absorb considerable amount of laser energy and transfer the heat energy to the Al substrate to provide higher penetration depths and better uniformity of composite microstructure. Ceramics have completely

filled valance shell and no valance electrons are available, resulting in laser radiation energy absorbed by photons. The preplaced powder layer, by virtue of its porous structure exhibit low thermal conductivity guaranteeing unnecessary melting of the substrate material and prevents vaporization of elements from melt pool (Lo et al., 2003). The effects of the addition micron sized and nanometer-sized particles in Al alloys by LCS are discussed in the following sections.

2.3.5.1 Addition of Micron Sized Particles

Addition of second phases and particulates are essential in order to improve strength of metal matrix. These added particulates should be uniform in size and shape, coherent with the matrix phase and homogenously distributed (Allen & Ball, 1996). Nevertheless, Al alloys does not provide sufficient matrix strength to hold the hard particles and thus require a strong alloy or intermetallic matrix with sufficient strain capacity. Due to poor wettability of carbide ceramics with group III elements, it becomes necessary to add additives of transition elements in the powder mixture. The transition elements provide good wettability with ceramic carbides during partial powder melt. LCS by the addition of micro sized SiC, WC and TiC particles have been reported to provide substantial improvement in bulk phase properties. Some authors (Viswanathan et al., 2012), obtained crack free TiC particulate reinforced $Al_{11}Fe_4$ matrix composite layer on sand blasted Al–12 wt% Si alloys with CO_2 laser energy of $50J/mm^2$. The potential applications of Al-Si alloys lie in cylinder blocks, cylinder heads, piston, piston pins and valve lifters in automobile components because of their high specific strength, low density and thermal conductivity (Chandrashekharaiah & Kori, 2009). It was noted that TiC particles were partially melted in $Al_{13}Fe_4$ matrix, to improve the wettability, cohesion, micro hardness (750 HV) and friction coefficient (0.05). Block-on-ring tribometer revealed 10 times improvement in wear rate (3.98×10-7 mg/m) owing to absence of plugging and loose debris in composite coating. In

contrast, the Al-Si alloy revealed significant asperity penetrations. Similarly, other authors (Vreeling et al., 2000), observed de-cohesion of larger aluminum carbides particles from the matrix when laser injected SiC particles onto Al substrate. Furthermore, during in situ tensile testing, the SiC particles are prone to cracking. Once research was focused on the development of globular SiC particulate reinforced graded composite on commercially available pure aluminum to produce hardened layer (150-240 VHN) and promoted wear resistance up to three times (Dutta Majumdar et al., 2006). However, mainly due to presence of Al_4C_3 phase, the corrosion resistance of the composite in a 3.56 wt% NaCl solution was lowered (Dutta Majumdar et al., 2006). Similarly, (Man et al., 2000) LCS of AA6061 alloy with Si_3N_4 and a mixture of SiC + Si_3N_4 stated improvement in cavitation and erosion resistance. However, pitting corrosion resistance deteriorated, which aforementioned authors also observed.

Apart from SiC particulate reinforced aluminum matrix (Labisz, 2014), showed raising laser power resulted in increasing hardness and grain refinement of Al-Si-Cu alloy modified with WC particulates. Similarly, it was revealed that due to the large difference in specific mass between WC and SiC (15.6 and 3.2 g/cm^3), WC particles sunk in the bottom layer of AA6061 alloy (Jendrzejewski et al., 2009). Moreover, preheating the substrate above 600K maximizes the penetration depth of the particles. It is pertinent to state that the likelihood of crack development due to difference in thermal expansion coefficient, causing severe stress build-up is usually present. Hence, by introducing graded microstructures, where gradual change in composition with melt depth produced a functionally gradient coating may help contain defect formation. Although considerable increase in wear resistance through LCS has been realized, the addition of carbon nanotubes (Sinnott & Andrews, 2001) and Nano particles, graphene and transition metal dichalcogenides as self-lubricating phase may result in a decrease in friction coefficient (Choi et al., 2010; Y. Li et al., 2012; Sorkin et al., 2014).

2.3.5.2 Addition of Nanometer sized particles

One particular interesting development surrounding LCS of Al alloys includes addition of nanometer-sized particles and use of ring beam laser spot profile. In one work the effect of nanometer sized diamond particulates on aluminum A319 substrate during LCS using a CO_2 beam profile of diffraction free ring (Blum & Molian, 2014). The research work was targeted to improve the tribological properties of A319 cylinder bores. The annular ring beam was generated using rotationally symmetric prism and special optics Axicon conical lens. The conical lens transforms the Gaussian beam profile into a diffraction-free Bessel beam. The advantage of diffraction-free Bessel beam is that it prevents this "balling" phenomenon, as it does not spread when propagated as showed in Figure 2.16.

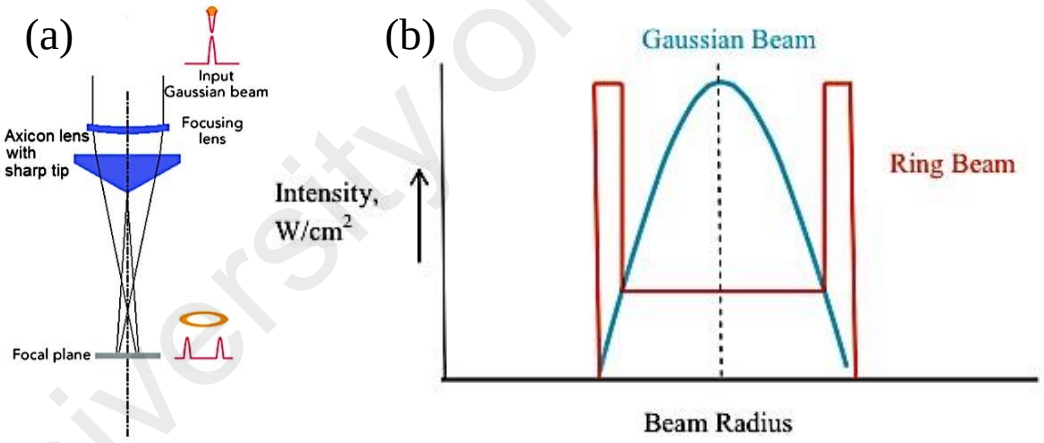

Figure 2.16: (a) Axicon and Plano-convex lens configuration to produce ring beam profile and (b) energy intensity distribution of ring beams in comparison to conventional Gaussian beam (Reprinted with permission from Elsevier, License no: 3575190366744) (Blum & Molian, 2014)

The laser Gaussian beam produces steep temperature gradients from the centre towards the edge of the treated zones. In contrast, lesser maximum temperature is attained in the ring beam with higher energy concentrated in the annular region. This leads to the

conduction of heat towards the inner and outer circumference of the annular region. As a result, lesser convection currents are produced and the melt pool depth remains shallower. In addition, ring beam prevents surface tension gradients and provides uniform heating effects (Belanger & Rioux, 1978). A thin layer of Al substrate was melted in a controlled fashion to transform nanodiamond to form a 50-60 μm thick nanodiamond/diamond-like carbon (DLC) coating. Considerable work has been carried out to observe substantial enhancement in surface roughness, friction, and wear of coating nanodiamond/DLC.

2.4 Laser coatings incorporating solid-lubricants

The need for solid lubrication arises in applications involving high temperature, extreme pressure, high vacuum, radiation zones, and cryogenic conditions, corrosive and extremely dusty environments. Under extreme conditions, vacuum pressure may vary from 10^{-2} Pa to gas density of 10^{-12} molecules/cm^3s. Furthermore, the limitation of liquid lubricants is that they vaporize at temperatures extending beyond 523 K and may solidify at temperatures as low as 0 K (Reeves et al., 2013; H. Z. Yang et al., 2015). The dust particles in cement and process industries may adhere to the lubricants thereby forming a paste, which may lead to failure by adhesive wear. Hence, solid lubricants possess the benefits of carrying substantially lesser weight in lieu of liquids, are un-affected by dust, radiation and pressure and they eliminate the need for lubricant pumping and cooling systems. The addition of solid lubricants in coatings has tremendous potential to target advanced tribo-system applications. During tribological wear, the solid lubricant enters in between the contact of the relative surfaces. They can shear to reduce friction and form protective transfer layer to reduce wear. Below is a description of friction reduction mechanisms involved and classifications of solid lubricants.

2.4.1 Friction Reduction Mechanism

Under tribo-contact sliding conditions, when either of the sliding substrate has a solid lubricant surface, third bodies (wear particles and debris) are generated at asperity contact. These particles have the ability to be partly transferred to the counter surface hard body by adhesion, then relative displacement takes place (Kato, 2000). As showed schematically in Figure 2.17, the transfer layer is thus formed between the tribo-contact as a result and the less shear strength of transfer layer. The relative displacement of transfer layers thereby promotes lesser friction ultimately leading to lesser wear rates (Scharf & Prasad, 2013).

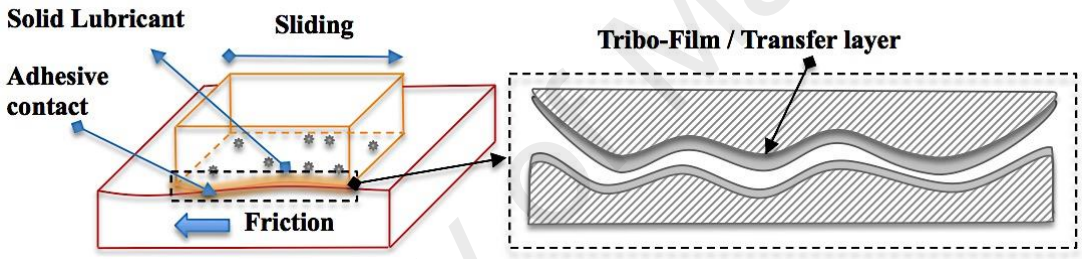

Figure 2.17: Schematics of adhesive contact between two surfaces and adhesion leading to the generation of transfer film which is detached from the softer solid and adhered to the harder solid.

In the following sections a brief overlook of classification of solid lubricants is made based on their assimilation with laser based coatings.

2.4.2 Classification of Solid-Lubricants

The solid lubricants that have been incorporated in laser-clad coatings can be categorized into three groups. One group contains lamellar solid materials encompassing graphite, hexagonal boron nitride (hBN) and transition metal dichalcogenide compounds (e.g. MoS_2 and WS_2). The second group comprises of metal

oxides fluorides (e.g. CaF_2, BaF_2) and the third group encompasses soft metals (e.g. Ag, Cu, Sn) and other material systems. There are also various other types of materials available with self-lubricating capabilities such as mixed oxides, sulfates of alkaline earth metals, carbon based solids and organic polymers (Scharf & Prasad, 2013). But their usage has hardly been noted in the literature of laser-based coatings.

2.4.3 Lamellar based solids

Lamellar based solid lubricating materials have layered crystal structure. These materials include lamellar solids such as transition metal dichalcogenides (WS_2 and MoS_2), graphite and hexagonal boron nitride (hBN) etc (Erdemir, 2005). They possess inherently lower shear strength, lower friction and wear as to when they are applied on the surface or when they become a part of the coating system. The ability of these materials to lubricate a given system entirely is dependent on the operating conditions. For instance, graphite works effectively in moist and humid conditions whereas; MoS_2 is widely employed in airspace and vacuum environments (Donnet & Erdemir, 2004; Savan et al., 2000). When assimilated in a metal matrix, it is often beneficial for improving hardness. As showed in Figure 2.18, the addition of most of the solid lubricants has resulted in increase in coating hardness. The reduction in friction coefficient values due to the addition of lamellar based solid lubricants is presented in Figure 2.19

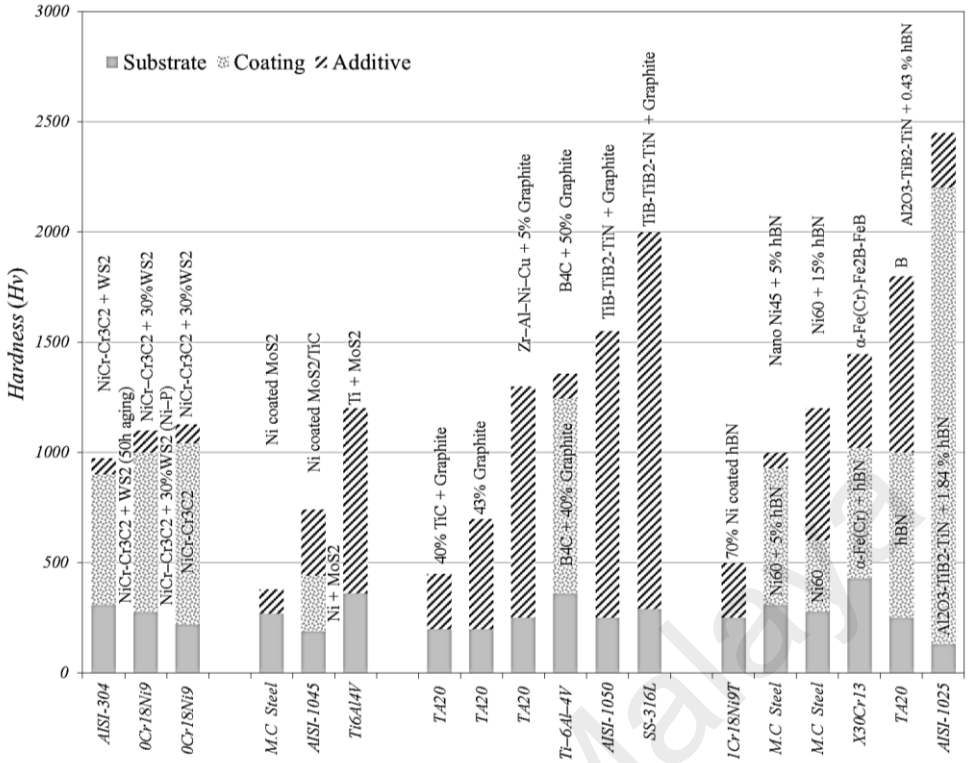

Figure 2.18: The Vickers hardness of various claddings with and without lamellar based solids lubricant

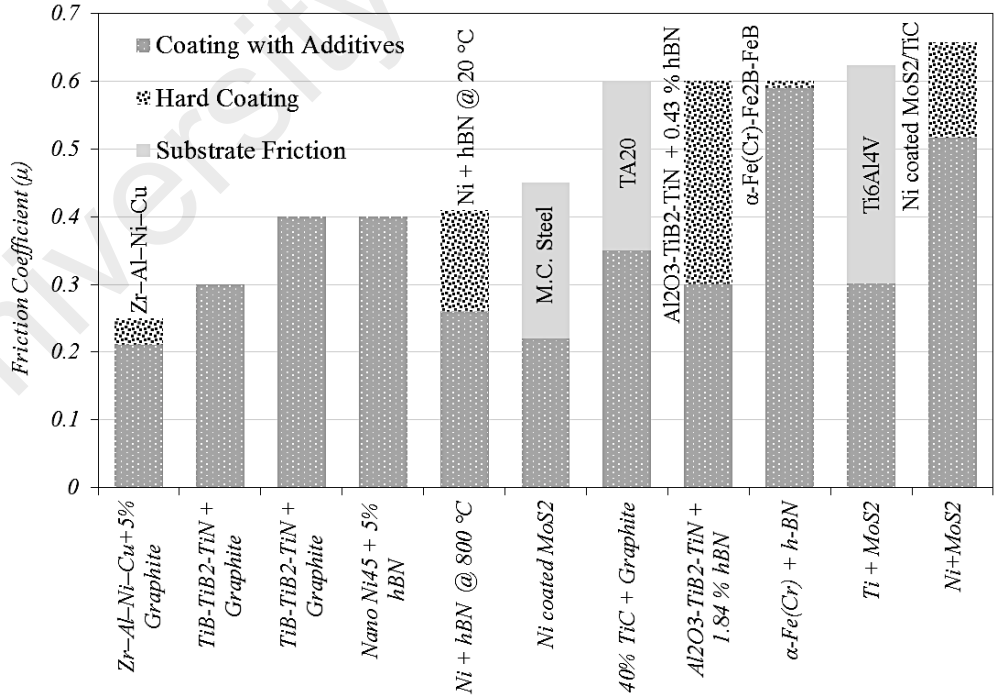

Figure 2.19: Friction coefficient enhancement due to addition of lamellar based solids lubricant

Wear is not entirely a function of hardness but is depended on various other factors such as friction coefficient (Kato, 2000). The lowest friction coefficient values have been reported in the range of experiments conducted by each author. The laser clads containing MoS_2 and graphite has lowered friction to a lowest value of around 0.21-0.22. The operating temperature may limit the use of graphite and MoS_2 in high temperature applications but hexagonal boron nitride exhibits favorable lubricating properties at high temperature environments. Furthermore, when lubricating powders are encapsulated to prevent chemical decomposition upon laser beam irradiation, the hardness improves further. The LSC has been carried out by CO_2, Nd: YAG and diode lasers under the influence of argon and nitrogen as shielding gas to prevent oxidation and porosity inclusion in coatings. With the application of circular and rectangular beam diameter modes, coating thickness in the range of 300-1200 µm has been produced. The tribological testing conditions corresponding to the solid lubricant coating, wear rates and their targeted applications are summarized Table 2.2. In general, the tribological properties of these coatings have been assessed by pin-on-disk, pin-on-ring and ball-on-disk tribo-pair configurations. Most of the experiments have been carried out at normal operating temperatures, but some researchers have conducted trials at temperatures as high as 800 ºC to gauge the ability of solid lubricant to preserve its lubricating properties at extreme operating conditions. For each research work, the tribological examining conditions such as applied load and sliding velocity differ. Apart from varying testing conditions, the wear rates have also been computed differently, which are presented either as mass loss, volume loss, and relative wear resistance or in terms of specific wear unit. Hence, it is difficult to make a comparison of coating tribological performance based on wear rates. Certainly, with the introduction of these types solid lubricants in the cladding material systems, an enhancement in wear resistance to about 1.07-6.5 times can be observed for particular tribological conditions. Various types of

substrates and counter bodies were used as tribo-pairs during tribological experiments. Both ferrous and non-ferrous materials have been used as counter-bodies. Some of the commonly employed non-ferrous counter body material includes ruby or aluminum oxide (Al_2O_3), silicon nitride (Si_3N_4), tungsten carbide (WC), tungsten carbide particulate reinforced nickel composite (WC_p/Ni), and tungsten carbide-cobalt cemented carbide (WC/Co).

Table 2.2: A summary of tribological testing parameters when lamellar based solid lubricants are incorporated

Substrate Material	Type of Coating	Tribometer Type	Wear of substrate$^{(s)}$/hard coating$^{(c)}$	Wear with solid lubricant	Improvement in wear resistance
Addition of Graphite					
Titanium (B. Courant et al., 1999)	TiC + Graphite	Pin-on-disc	-	-	-
TA20 (Yanfang Wang et al., 2014)	Zr–Al–Ni–Cu + Graphite	Ball on disk	-	-	-
AISI-1050 (Choudhury et al., 2008)	TiB-TiB_2-TiN + Graphite	Pin-on-disc	1.25 e^{-4} $mm^3/Nm^{(s)}$	9 e^{-5} mm^3/Nm	1.33
SS-316L (Choudhury et al., 2008)	TiB-TiB_2-TiN + Graphite	Pin-on-disc	1.2 e^{-4} $mm^3/Nm^{(s)}$	6 e^{-5} mm^3/Nm	2.1
Addition of MoS_2					
Ti6Al4V (Yang et al., 2013)	MoS_2/Ti	Pin-on-disc	-	-	-

Table 2.2: Continued

Substrate Material	Type of Coating	Tribometer Type	Wear of substrate[(s)]/hard coating[(c)]	Wear with solid lubricant	Improvement in wear resistance
1045 Steel (Xu, Liu, & Zhong, 2006)	MoS_2/TiC/Ni	Pin-on-disc	3.25 mg[(s)]	0.5 mg	6.5
M.C. Steel (Fe-0.45C-0.3Si-0.6Mn) (Niu et al., 2011)	MoS_2/Ni	Pin-on-ring	6 mg[(s)]	2 mg	3
1045 Steel (Han et al., 2012)	Ni/MoS_2	Pin-on-disc	90 mg[(s)]	70 mg	1.28
Addition of WS_2					
0Cr18Ni9 (M.-S. Yang et al., 2012)	NiCr/Cr3C2, NiCr/Cr3C2 + 30%WS2	Ball-on-disk	22.5 e^{-6} mm^3/Nm @ 300°C[(c)]	15 e^{-6} mm^3/Nm @ 300°C	1.5
0Cr18Ni9 (X.-B. Liu, Zheng, et al., 2013)	NiCr–Cr3C2 /30%WS2 and NiCr–Cr3C2 /30%WS2 (Ni–P)	Ball-on-disk	48.5 e^{-6} mm^3/Nm @ 600°C[(c)]	45e^{-6} mm^3/Nm @ 600°C	1.07

Table 2.2: Continued

Substrate Material	Type of Coating	Tribometer Type	Wear of substrate(s)/hard coating(c)	Wear with solid lubricant	Improvement in wear resistance
Hot-rolled AISI304 Steel (X.-B. Liu, Liu, et al., 2014)	NiCr/Cr3C2 + WS2	Ball-on-disk	39.32 e^{-6} mm^3/Nm(c)	40.59 e^{-6} mm^3/Nm @ 50 h aging	-
Addition of hBN					
X30Cr13 (Avril et al., 2006)	α-Fe (Cr)-Fe2B-FeB & α-Fe (Cr)-h-BN	Pin-on-disc	275 e^{-15} m^3/Nm(s)	115 e^{-15} m^3/Nm	2.4
1Cr18Ni9T (S. Zhang et al., 2008)	Ni/hBN	Ball-on-disk	2.5 @ 100°C(c)	0.05 @ 600°C	5
M.C. steel (Fe, 0.45C, 0.3Si, 0.6Mn) (H. Yan et al., 2010)	BN, (Nano-hBN)	Pin-on-ring	-	-	-
AISI 1025 (Chatterjee et al., 2012)	Al_2O_3-TiB_2-TiN	-	-	1.03 e^{-4} mm^3/Nm	-

2.4.3.1 Addition of Graphite

The addition of graphite in laser clads is not only beneficial for reducing friction but considerable improvements in hardness, wear and toughness have been witnessed by some authors (Scharf & Prasad, 2013). Graphite not only serves as a solid lubricating phase in the hard composite matrix but it has been added in excess quantities in laser clad powder blends to synthesize in-situ reaction based hard coatings. Owing to the lamellar structure of graphite, as low as around 0.21 value of friction coefficient has been reported **(**Figure 2.1). The amount of graphite present in the cladding entirely depends on the laser processing parameters. In one study (Fouilland-Paille et al., 1997) cermet Ti/TiC coating on α-titanium foil by pulse radiation of a Nd-YAG laser was fabricated. It was found that by applying low power and higher scanning speed, cracks appeared and a part of pre-placed powder remained un-melted. Whereas, at higher power and lower scanning speeds, the amount of dilution increased which caused insufficient hardness in clad region. Similarly, at 20 μm of pre-placed powder thickness, immeasurable amount of surface roughness was observed. For a 10-μm pre-placed powder thickness, higher hardness was obtained which was attributed to dispersion of non-stoichiometric TiC_{1-x} or $Ti_{1-x}C$ in grain refined titanium matrix. In another study (Bruno Courant et al., 2005; B. Courant et al., 1999), researchers established a relationship between the parameters of pulse laser radiation on thickness of the laser melt zone (LMZ) and percentage of graphite included in LMZ. It was found that graphite prevented the transfer of titanium to the counter body by adhesion. The study was carried out based on relations of heat transfer with pulse radiation parameters. The two parameters characterizing each laser pulse were surface density of deposited energy (F, J/mm^2) and pulse power (P, W).

$$F = \frac{E}{2\tau Vr + \pi r^2} \tag{2.2}$$

$$P = \frac{E}{\tau} \tag{2.3}$$

Where E is the pulse energy, τ is pulse duration, V is motion speed and r is the laser beam radius. Moreover, additional parameters describing the succession of laser pulses were time ratio of laser beam emission (B) and superposition ratio of two areas successively irradiated (R).

$$B = \tau f \tag{2.4}$$

$$R = \frac{2r+(\tau-(1/f))V}{2r+\tau V} \tag{2.5}$$

It was established that the higher hardness of coating was directly related to the greater atomic percentage composition of carbon present in the least thick LMZ. The amount of carbon mixed was associated with titanium carburizing and higher superposition ratio (R), lower time ratio (B) and pulse power (P) which result in a gradual heating (Bruno Courant et al., 2005). Further research works (Choudhury et al., 2008), concentrated on preplaced TiO_2 nano-particles, B_4C and graphite powder on medium carbon steel and stainless steel by using K-bar or K-Hand coater. Laser based nano-structured metal matrix composite (MMC) coating was synthesized with the nano-particulate phases comprising of TiB_2 and TiB producing hardness in the range of 800 to 2000 H_v. Inclusion of remnants of graphite resulted in reduction of friction of base material from 0.6 to 0.37. Analogous results were obtained when some researchers (J. X. Yang et al., 2012) included graphite in Ni-60 super hard alloy to reduce friction coefficient from 0.55 to 0.20. This coating could be utilized as a medium temperature abrade-able sealing coating in compressor and turbines where blade clearance is kept very low.

Further works examined the influence of graphite composition (0 to 10%) on the tribological properties of amorphous Zr-Al-Ni-Cu cladding on Ti substrate for bulk metallic glasses (BMGs) application (Yanfang Wang et al., 2014). BMGs have been known with high glass-forming ability, higher strength and hardness. The addition of 5% graphite was considered to be optimal for producing higher hardness and least friction coefficient (0.20–0.27) owing to the lubricious effect of graphite and amorphous content of coating. More works (Tian et al., 2006) therefore reported that the addition of graphite and silicon on Ti-6Al-4V resulted in reduction of friction coefficient from 0.5 to 0.37 and ultimately led to 5 times improvements in wear resistance. Some investigators (H. X. Zhang et al., 2014), synthesized TiC, TiN, TiB and TiB_2 coating by LSC of B_4C and 40-50% graphite. When the mass ratio of graphite was up to 50%, a reduction in wear to about 3 to 5 times was observed. The addition of graphite in laser-based coatings to fabricate hybrid metal matrix composite using laser engineered net shaping (LENS) has showed a balance of mechanical properties and it has been patented (Gopagoni et al., 2013). Similarly composite materials systems for laser claddings with the addition of graphite have also been patented (Denney & Whitehead, 2014).

2.4.3.2 Addition of Molybdenum di sulphide (MoS_2)

MoS_2 has very strong covalent bond between Mo and S atom within the lamella, while the van der Waals forces hold each lamella together. These weaker inter-lamellar van der Waals bond are thus easily shear-able and give rise to low friction coefficient during sliding experiments (Spalvins, 1987). Upon laser irradiation, MoS_2 has been found to decompose and react with the constituent elements in the melt pool (Lei et al., 2015). XRD results of MoS_2/TiC/Ni based composite cladding on 1045 low carbon steel revealed the formation of multi-element sulfide phases (Xu, Liu, & Zhong, 2006). The

MoS_2 and TiC powder was partially dissociated due to their low melting point of 1185 °C and 3200 °C. The free carbon thereafter combined with the dissociated Mo to form Mo_2C carbide. According to them, MoS_2/Ni coating reduced the friction coefficient of substrate from 0.82 to 0.37 due to transfer of solid lubricant film to counter body, however the cladding was completely worn off under 10 min due to low hardness which contributed to high specific wear. Ni/MoS_2/TiC coating exhibited better TiC particulates to matrix adhesion owing to partial dissolution of TiC. The addition of TiC in Ni-MoS_2 presented improved wear performance and resisted plastic deformation in addition to groove formation when compared with MoS_2/Ni coating. The higher sulfide content and hard particulate TiC reinforced composite Ni/MoS_2/TiC coating revealed 6 times greater wear resistance (Xu, Liu, & Zhong, 2006). Ti/MoS_2 composite coatings on Ti6Al4V and showed that MoS_2 decomposed (Yang et al., 2013) in the following way.

$$MoS_2 \rightarrow Mo_xS_{x+1}(x=2, 3, 5) + S \quad (2.6)$$

$$Ti + MoS_2 \rightarrow Ti_3Mo_{0.75}S_5 + Ti_2S + Mo_xS_{x+1}(x = 2, 3, 5) + TiS_{0.5} \quad (2.7)$$

The wear and friction are dependent on the percentage composition of the solid lubricant added. As MoS_2 percentage composition increases in Ni-based alloying powder, wear and friction were reduced (0.52 to 0.40) (Han et al., 2012). LSC on AISI 1045 steel led to formation of Cr_xS_y, MoS_2 and FeS phases. Since FeS and MoS_2 are close-packed hexagonal structure, hence they assist in the slippage along the sliding surface to produce excellent anti-friction effect. The Gibbs free energy of Cr_xS_y is higher than MoS_2 and at the same temperature the free Cr and Fe reacts with S to form Cr_xS_y. Similarly some researchers (Niu et al., 2011), developed MoS_2/Ni coatings on carbon steel with Ni60/50 wt. % nickel coated MoS_2 and reported the formation of

spherical Cr_xS_{1+x} and white dotted Fe_xS_{1+x} lubricating phase which was found to be dispersed in a metal matrix complementing to a reduction in friction coefficient.

2.4.3.3 Addition of Tungsten di sulphide (WS_2)

Just like graphite and MoS_2, WS_2 also has a lamellar structure and low shear strength, which enable WS_2 to form lubricious transfer films under tribological contact (Prasad et al., 1999). More importantly, WS_2 has relatively higher oxidation temperature (539 °C) than graphite (325 °C) and MoS_2 (370 °C) (Scharf & Prasad, 2013). Hence, it is able to sustain its lubricity at relatively higher temperatures. Several works that have been carried out to fabricate self-lubricating WS_2 based coatings suggest that WS_2 can effectively reduce wear at around 300 ºC. The addition of 30 wt. % WS_2 in NiCr–Cr_3C_2 coating was examined (M.-S. Yang et al., 2012). X ray diffraction analysis revealed that only minor phases of WS_2 and CrS were present. Hence, WS_2 was reported to have significantly decomposed and oxidized upon high-energy beam radiation. However, it was stated that the formation of CrS phase was favorable as it has lubricating properties (He et al., 2011). The addition of WS_2 produced thicker coatings by virtue of its high-energy absorptivity, improved metal wettability and reduced the mass rate of Cr_3C_2 phase. Furthermore, it contributed to a lesser amount of material splattering during laser beam and powder interaction. Ball-on-disk wear test revealed that the coating wear with WS_2 was reduced only at 300 ºC as black traces of lubricious film of CrS and WS_2 were visible, thereby reducing the amount of both abrasive and adhesive wear. The wear mechanism of coating was generation and breakdown of transfer film at 300 ºC, however at higher temperatures of 600 ºC, the lubricating phase was oxidized and the transfer layer was not formed (M.-S. Yang et al., 2012).

Since WS_2 cannot survive the laser radiation, it can either be encapsulated with nickel by high-energy ball milling or else Ni or Ni-P electro-less plating can be performed to

improve its chemical and thermal stability. Ni–P electro-less plating of WS_2 particles showed the decomposition of WS_2 particles dispersed in the ductile γ-(Fe, Ni)/Cr_7C_3 matrix was reduced (X.-B. Liu, Zheng, et al., 2013). During the friction process, at about 300 ºC, certain amounts of WS_2 were released forming transfer layer lubricating film between the sliding bodies. In another of study, it was found that aging treatment had no profound effect on wear resistance of NiCr–Cr_3C_2–WS_2, however the friction coefficient was reduced after 50hrs of aging treatment at 600 ºC (X.-B. Liu, Liu, et al., 2014).

2.4.3.4 Addition of hexagonal boron nitride (hBN)

Hexagonal boron nitride (hBN) is white in color and is often termed as a clean lubricant. Since the black color of MoS_2 and graphite gives the coatings a dirty appearance. Hexagonal boron nitride exhibits high chemical inertness, oxidation resistance and thermal conductivity (Kimura et al., 1999; Kostoglou et al., 2015). In contrast to MoS_2 and graphite, which have demonstrated detrimental frictional characteristics at elevated temperatures, the graphite like lamellar hBN institutes lowers the friction in high temperature applications (B. Podgornik et al., 2015). Their use in high temperature applications includes metalworking, nuclear-based valves and pipefittings and aerospace industries (Eichler & Lesniak, 2008).

In one study (S. Zhang et al., 2010), researchers produced NiAl/hBN on Ni-based super alloy substrate and found coating had high micro-hardness and superior tribological properties at temperatures up to 1000 ºC. In another work (Chatterjee et al., 2012) researchers performed in-situ SHS laser treatment followed by laser surface remelting. Laser remelting not only diminished the unfavourable effect of hBN on hardness, but it augments the gainful effect of free hBN on wear resistance. Hexagonal boron nitride in surplus quantity was added in precursor mixture (as per Eq. 7) to obtain free hBN

available in the final matrix as a lubricating phase.

$$4Al + 3TiO_2 + 2BN = 2Al_2O_3 + TiB_2 + 2TiN\ (2303K) \quad (2.8)$$

2.4.4 Halides and metal oxides based materials

Alkali fluorides are characterized not only by their low shear strength but they possess stable and favorable thermal properties (Libo Wang et al., 2007). These materials undergo brittle to ductile transition in the event the temperatures rises, and hence become easily shear-able (Sliney, 1993). Oxide (sub-stoichiometric TiO_2) and fluorides of alkaline earth metals (CaF_2, BaF_2, SrF_2, LiF_2, and MgF_2) based solid lubricants are advantageous when tribo-pair components operate at elevated temperatures (Aouadi et al., 2014). Until now, the effect of addition of only CaF_2 and TiO_2 on surface hardness (Figure 2.20) and friction coefficient **(**Figure 2.21**)** is reported for Al_2O_3 structural ceramic, titanium, copper and steel alloys. With the addition of 10-20 wt. % CaF_2, friction coefficient in the range of 1.9-2.2 is observed. A summary of tribological testing conditions and some applications of these halide and oxide based LSC are presented in Table 2.3. Nickel and cobalt based coatings are usually utilized as material for high temperature wear resistant coating to protect relatively wear prone substrates. Their tribological properties have been evaluated by block-on-ring, ball-on-disk, pin-on-wheel and pin-on-disk tribo-pair configurations. The counter-body material selected have been silicon nitride Si_3N_4, hardened 0.45 wt. % carbon steel and GCr15 steel. A summary of the tribological properties of the halides and oxides based coating materials are given in Table 2.4.

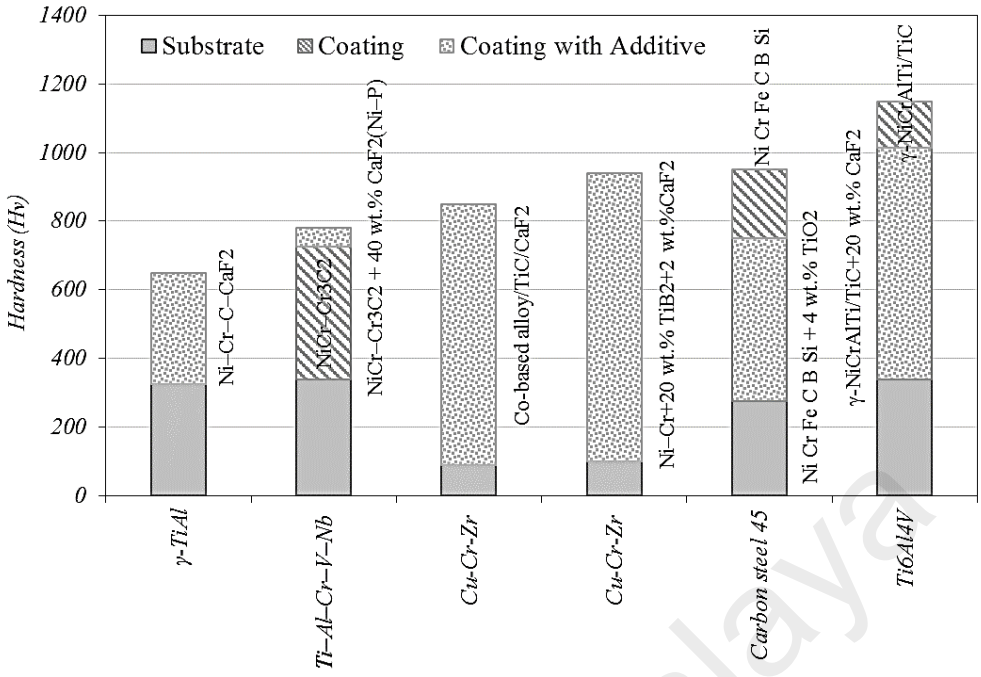

Figure 2.20: Micro hardness of various samples cladded with additions of solid lubricant

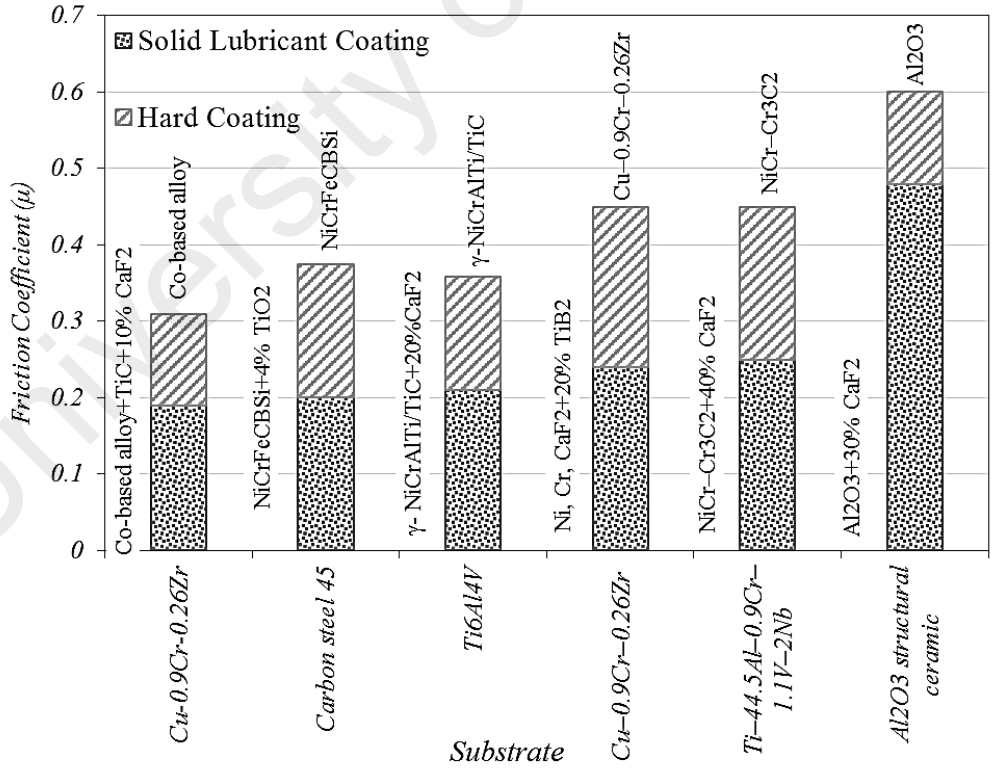

Figure 2.21: Reduction in friction coefficient of various samples cladded with additions of solid lubricant

Table 2.3: A summary of tribological testing parameters when halides and oxide based solid lubricants are incorporated

Substrate	Coating	Tribometer	Counter body	Load (N)	Speed (m/s)	Wear	Target Applications
Ti–44.5Al. 0.9Cr, 1.1V, 2Nb Alloy (X.-B. Liu et al., 2009)	NiCr/Cr_3C_2+CaF_2 (Ni–P electro-less plated)	Block-on-ring	Hardened 0.45% C steel	98	0.84	2.9	Aerospace - elevated temperature self-lubrication composite coatings
Ti6Al4V (Xiang et al., 2014)	γ-NiCrAlTi/TiC, γ-NiCrAlTi/TiC+CaF_2	Ball-on-disc	Si_3N_4	5	0.28	2.5 e^{-5} mm^3/Nm	Compressor blades and exhaust nozzle
γ-TiAl (W.-G. Liu et al., 2009)	Ni–Cr–C+CaF_2	-	-	-	-	-	Aerospace
Al2O3 structural ceramic (H. M. Wang et al., 2002)	CaF_2+Al_2O_3	Pin-on-wheel	Hardened 0.45%C steel	98	0.92	0.0014	High temperature wear resistance
Cu-0.9Cr-0.26Zr (wt.%) (Hua Yan et al., 2013)	Co-based alloy+TiC+CaF_2	Pin-on-disk	GCr15	100	4	0.8 e^{-5} g/Nm @ 20 % CaF_2 (W D C I)	Continuous casting molds and electrical contacts

Table 2.3: Continued

Substrate	Coating	Tribometer	Counter body	Load (N)	Speed (m/s)	Wear	Target Applications
Cu–0.9Cr–0.26Zr (Hua Yan et al., 2012)	Ni–Cr+TiB_2	Pin-on-disk	GCr15	100	2	77.1 mg @ 20%	Continuous casting molds and electrical contacts
Carbon steel 45 (Chao & Liang, 2004)	Ni Cr Fe C B Si+ TiO_2	Block-on-ring	GCr15	300	0.9	-	-

Table 2.4: A summary of LSC and tribological testing parameters with the addition of combination of solid lubricants and soft metals

Substrate Material	Coating	Tribometer Type	Counter Part	Load (N)	Speed (m/s)	Wear of substrate(s)/ hard Coating(c)	Wear with Additive	Improvement in wear	Wear mechanism when solid lubricant are incorporated
1Cr18Ni9Ti (Lingqia Wang et al., 2012)	NiCr/Cr_3C_2+Ag +BaF_2/CaF_2	Ball-on-disk	Si_3N_4	10	0.21	100 e^{-6} mm^3/Nm @ 24 hrs milling	6 e^{-6} mm^3/Nm @ 4 hrs milling	16.66	Abrasive wear
1Cr18Ni9Ti (X.-B. Liu, Liu, et al., 2013)	NiCr/Cr_3C_2, NiCr/Cr_3C_2+WS_2+CaF_2	Ball-on-disk	Si_3N_4	2, 5 & 10	0.048	19 e^{-5} mm^3/Nm 300°C(s)	2 e^{-5} mm^3/Nm 300°C	9.5	Formation of transfer layer, mild oxidation and slight ploughing.
M.C. Steel (Fe, 0.45C, 0.3Si, 0.6Mn) (A. H. Wang et al., 2008)	Ni45+WS_2+CaF_2 & Ni60+WS_2	Ball-on-disk	AISI E52100	20	2	23.5(c)	7.5	3.13	Formation of thin lubricating film.

Table 2.4: Continued

Substrate Material	Coating	Tribometer Type	Counter Part	Load (N)	Speed (m/s)	Wear of substrate(s)/ hard Coating(c)	Wear with Additive	Improvement in wear	Wear mechanism when solid lubricant are incorporated
45 Steel (Zhu et al., 2014)	Ni+Ag/TiC	Ring-block	GCr15	200	-	-	-	-	Abrasive wear marks and some ploughing traces.
AA2024-T531 (Blum & Molian, 2014)	Nano-diamond	Ball-on-disk	440C Steel	5	13.1	11.85 e^{-3} mm^3/Nm (s)	3 e^{-3} mm^3/Nm	3.95	Formation and spallation of chemical layer on the worn surface.

2.4.4.1 Addition of calcium di fluoride (CaF_2)

CaF_2 is a widely utilized solid lubricant due to its superior physical, chemical and microstructural characteristics. It prevents adhesive wear and instigates tribochemical wear due to its ease of shear-ability at elevated temperatures (Sliney, 1993). CaF_2 has a lamellar structure and shears along the basal plane of the hexagonal crystalline structure (DellaCorte & Wood, 1994). Under the action of higher temperatures, the CaF_2 will shear and a transfer film will be formed (Xiang et al., 2014). The higher chemical stability, heat resistance and low shear strength makes CaF_2 soft with low hardness that influences the tribological contact and hence is used to produce anti-wear self-lubricating composite coatings for high temperature applications (Bi et al., 2013).

2.4.4.2 Addition of Titanium di oxide (TiO_2)

LSC of with TiO_2 powders has rarely been reported in open literatures (Y. Chen et al., 2013). Recently, LSC of carbon steel with doping of TiO_2 has been reported in one instance to augment both friction coefficient and fracture toughness. It is reported the effect of 0–4 wt. % TiO_2 doping on LSC of stellite NiCrFeBSiC coating (Chao & Liang, 2004). With increasing percentage of TiO_2 the hardness of the layer decreases owing to formation of Cr_3Ni_2SiC intermetallic compounds and escalation in amount of eutectic formed. In addition, new phases such as TiC and TiB_2 upon the TiO_2 doping were detected which reduced the formation of holes and craters on the worn surface. Increasing weight percentage of TiO_2 addition resulted in a decrease of porosity and crack sensitivity as a result of microstructural refinement. One study (Gardos, 2000), demonstrated the beneficial effects of oxygen vacancies in rutile TiO_2 that enhances the shearing mechanism by forming lubricious oxide film.

2.5 Applications of laser based self-lubricating composite coatings

There are extensive numbers of application involving solid lubricants in various specialized industries, which has been dealt with broadly in ref (Kathuria, 2000; Roberts, 2012; Scharf & Prasad, 2013; Voevodin & Zabinski, 2005). The main goal of incorporating solid lubrication is to increase the durability of the system without sacrificing the reliability thus resulting in improved fuel efficiency and reduced emissions. Solid lubricants have been successfully incorporated in biomedical and aerospace applications (Kazuhisa, 2007) and in materials for heavy duty and advanced heat engine components such as piston ring/cylinder wall contacts and valve guides. Similar components for automotive and power generation applications have also been investigated such as sterling engines, cylinder kits for heavy duty diesel engines, side wall seals of rotary engines and various exhaust components applications. Journals in foil gas bearings, brush seal shaft in turbine engines, process components in process industries such as valves, and fittings are some typical components requiring application of solid lubricant coatings.

When it comes to laser claddings comprising of solid lubricants, quiet fewer amount of literature related to their direct applications is available. Albeit laser-cladding technology has been around since the past 50 years, with the passage of time, cost, ease of availability and maintenance of lasers, the scope of laser claddings is now broadening and the quantity of related publications is increasing (Dubourg & Archambeault, 2008). Some of the patents related to the application of solid lubricants in laser claddings are now available covering a broad range of applications. The application of laser cladding of soft metal cooper was realized much earlier in 1988 by Kawasaki et al. (Kawasaki et al., 1988) for protection of the valve seat surface in the cylinder head portion. Furthermore, it was proposed (Adachi & Inami, 1998) that the valve seat could be

bonded with the cylinder head using Fe, Cu and Ni based alloys. Cu in laser claddings could be added due to its good heat-conductivity and self-lubricating properties and aims to enhance high temperature wear resistance (Kawasaki et al., 2004; Kawasaki et al., 2009). Furthermore, another patent related to the valve seat repair material selection comprising of borides of Mo have been reported (Sawada et al., 2008). Another invention relates with composite self-lubricating coating aimed at turbojets specifically relating to the assemblies of the blade to rotor disk (Vigneau et al., 2006). Materials systems involving laser claddings have been patented for piston rings (Herbst-Dederichs, 2005), coated rolling element bearing cages (Doll et al., 2006), composite bearing structure (Ecer, 1984), ceramic-particle-dispersed metallic systems (Arato et al., 1996), metal-clad hybrid coatings (McCrea et al., 2014), ultra-low friction coatings for drill stem assemblies (Jin et al., 2013), friction reducing amorphous coating (Scruggs, 1988), joint and bone replacement (Bose & Bandyopadhyay, 2015).

2.6 Statistical experimental design techniques

A test or series of tests wherein, process input variables are changed to identify and observe change in the variation of response or output is called an experiment. Design of experiment (DOE) methodology is utilized to determine the minimum number of trial experiments, which are to be carried out so as to obtain comprehensive information on the factors influencing performance parameters for laser surface processing . It thus possesses a viable and efficient methodology, in which the laser processing parameters will be tailored and optimized. Additionally, DOE is employed to design a set of experiments whereby all related factors are systematically varied and maximizes effectiveness of data collection in conducting trials. Amongst various DOE's formulations, Taguchi method specifies an efficient and systematic approach to process

parameters for optimization and requires identification of an orthogonal array (OA) by careful selection of control factors (D.-X. Peng, 2011).

The Taguchi methodology (Taguchi & Phadke, 1989) is one such approach, which employs main effects and interaction plots together with analysis of variance (ANOVA) to calculate the relative influence of individual test factors and the corresponding sensitivity of the associated levels in relation to selected response measures.

2.6.1 Taguchi Design of Experiment

Taguchi is an widely known powerful design of experiment technique that can significantly improve the quality of product fabricated by employing an experimental design that is easy to follow and systematic in terms of time and cost. The objective thereafter is to devise a methodology that will result in an optimum setting of control factors leading to the formation of a product that is insensitive to the noise factors. Design of experiment (DOE) is a process of experimental planning used to determine the least number of experiments to be performed so as to acquire the comprehensive information on the factors influencing performance parameters (Taguchi, 1987). It is also used to design a set of experiments whereby all related factors are systematically varied and maximizes efficiency of data acquisition in conducting experiments. Amongst various DOE's formulations, Taguchi is one of the significant DOE methods, providing a systematic and efficient approach for the optimization of the process parameters. The most important stage in the design of an experiment using Taguchi approach lies in the selection of control factors and identifying the orthogonal array (OA), a reliable approach to evaluate several design parameters simultaneously with fewer experiments (Ezazi et al., 2014b). The OA forms a stand of design (e.g. for 2 or 4 levels factors L4, L8, L16, L32 are applied and for 2 or 3 for L12, L18 & L9, L27 for 3 levels factors are applied). Thereafter the assignment table and following analysis is utilized.

Taguchi devised S/N ratio as the quality-determining factor (Taguchi, 1987). S/N ratio is used as a measurable value instead of standard deviation due to the fact that as the mean decreases, the standard deviation also decreases and vice versa. The S/N equation relies on its optimization of quality characteristics. The methods for calculating the S/N ratio are classified into three main categories, depending on whether the desired quality characteristics are smaller the better, larger the better or nominal the better. In the case of surface roughness, the smaller values are always preferred whereas in case of surface hardness larger values are required. The equation for calculating the S/N ratio characteristics (in decibel) is as follows. In the S/N ratio calculation (Eq. (1) & (2)), the "larger-the-better" and "smaller-the-better" characteristic formula were used to identify the combination of optimum factors to enhance the coating hardness and surface roughness respectively.

Smaller the better characteristics:

$$\frac{S}{N} = -10 \log \frac{1}{n} \left(\sum y^2\right) \tag{2.9}$$

Larger the better characteristics:

$$\frac{S}{N} = -10 \log \frac{1}{n} \left(\sum \frac{1}{y^2}\right) \tag{2.10}$$

Where n is the number of observations performed for each sample, which is three; and y is the measured response value of i^{th} experiment. For each characteristic type, the result is better with a higher S/N ratio in the above transformation. The S/N values serve as performance measurement, which enhances processes that are insensitive to noise factors. The degree of a process or product's predictable performance in the presence of noise factors could be defined from S/N ratios. After the determination of S/N rations, which are plotted for each factor, the level at which optimum value for each factor

comes up, is utilized. To identify the importance of each factor and its corresponding percentage influence on the output quality response, ANOVA technique is employed.

2.6.2 Analysis of variance Pareto (ANOVA) technique

The analysis of results obtained by experiments is further carried out by the analysis of variance technique called ANOVA. More details can be found in the reference (Miller Jr, 1997). This technique involves the division of the total variability of a output response into its individual components. It further compares the variance in the mean of an individual factor with intrinsic trial error. Later on, a confirmation test is performed in order to validate the conclusions drawn from the analysis.

2.7 Summary and conclusion

The following conclusions can be drawn from the literature review carried out so far in this study:

1. As laser processing itself is a highly sensitive process, hence stringent control of lasing parameters such as incident beam quality and wavelength, interaction time, temperature gradients, and power density are vital. Thus, the selection and optimization of these process parameters are essential to obtain defect free coatings. So far, researchers have focused on understanding the effect of the processing parameters and design of cladding systems, however various optimization methods such as Taguchi, fuzzy logic approach, grey relational analysis and genetic algorithm have not been taken into account.
2. The addition of solid lubricants in coatings has tremendous potential to target advanced tribo-system applications. During tribological wear, the solid lubricant enters in between the contact of the relative surfaces. They can shear to reduce friction and form protective transfer layer to reduce wear. Their use has been very limited owing to the difficulties encountered in laser processing.
3. The incorporation of a low temperature range based lamellar graphite, in general, has been beneficial in reducing the friction coefficient, as it does not decompose. MoS_2, WS_2, and hBN, when subjected to higher heat inputs can be partially prevented from decomposition by nano-encapsulation and Ni-P electroless plating technique. However, they have a tendency to react with other elements in melt pool. It is to be noted that hBN exhibit better tribological properties at higher temperatures range.
4. Although halide based lubricants are also prone to thermal decomposition, but they can effectively reduce the friction coefficient at high-temperatures when they are protected from thermal radiation. Their effective operating temperature range and

tribo-mechanical properties are further improved when WS_2 and CaF_2 are incorporated together.

5. Laser composite surfacing allows the development of a composite layer on the surface, which on the other hand remains extremely difficult with conventional processing. The formation of metal matrix composite layer improves surface hardness, elastic modulus, cavitation erosion resistance and wear/corrosion resistance. Numerous prospects of fabricating “hybrid metal matrix composites” comprising of oxide, sulfide and halide based solid lubricating phase and hard ceramic phase are available. Another, unique opportunity lies in the addition of nano-sized particulates and nano material components. Slight additions of nano particles (0.5–2 Vol.-%) produce more pronounced effects. These materials may act as nuclei agents to produce extremely fine microstructures. Hence, it would be interesting to see their interaction with lasers for fabrication of aluminum based nano composites and metal-ceramic systems.

It is challenging to cover all the literature related laser claddings comprising of solid lubricants in a limited length review article. Nevertheless, the associated reviews, research articles, proceedings, technical articles, book chapters and patents that are under the scope of this review have been included. It is quite essential to accommodate solid lubricant growth in the industrial sectors through a sustainable manner. Solid lubrication is exceptionally important for tribological applications where components are operating under extreme environment. With the technological advancement in laser processing technology, it is imminent that their demand is expected to rise for many more years to come. In addition, with the involvement of advanced tribo-systems in industrial applications, this study will become much more critical in reaping the advantages of laser cladding technology.

CHAPTER 3: MATERIALS AND EXPERIMENTAL METHODS

The physical properties of the substrates, MMC powders and solid lubricant materials that have been utilized for the fabrication of self-lubricating wear resistant metal matrix composite coating in the present work have been presented herein. Additionally, general procedures for sample preparation, powders preplacement, laser processing techniques have been explained. The microstructure, mechanical and tribological characterization techniques have been discussed. The data acquisition procedures have also been explained. A brief introduction to Taguchi design of experiment is given in the last section.

3.1 Substrate Materials

In this experimental work, two types of aluminium alloys have been utilized. The one being wrought Al-Mg AA5083 series and the other being as-cast Al-Si hypereutectic piston alloy. The MMC Ni-WC coating was deposited on AA5083, whereas, HMMC coatings were deposited on Al-17Si substrate. The chemical composition of these alloys is given below.

3.1.1 AA5083-O Aluminium Wrought Alloy

Laser composite surfacing was performed on commercially available sheet of wrought AA5083 (Al–Mg) aluminium alloy in O-temper state (4.9 wt% Mg, 0.4 wt% Mn, 0.13 wt% Si, 0.3 wt% Fe, 0.03 wt% Ti, 0.08 wt% Cu, 0.13 wt% Cr, bal. Al). The samples were cut in dimension 15 mm breadth and 6 mm thickness using electro-discharge wire cutting (EDWC).

3.1.2 Al-17Si Hypereutectic Cast alloy

The material Aluminum-Silicon alloy having chemical composition consisting of

0.11% Zn, 0.07% Mn, 1.64% Cu, 0.06, 17% Si, 0.09% Cr, 0.8% Ni and Al balance (in wt.%) were cut in dimension 15 mm breadth and 6 mm thickness using electro-discharge wire cutting (EDWC).

3.2 Coating Materials

Since, in this work three kinds of coatings were prepared. One being MMC Ni-WC coating and the other were being HMMC Ni-WC-Graphite and Ni-WC-TiO_2 coatings. Hence, the composite coatings were fabricated by procuring Ni, WC, Graphite and TiO_2 separately in powder form. The specifications of these powders, their sizes, compositions etc. are given below. Furthermore, at the end of this section a summary of the properties of all materials that were utilized in this research are tabulate.

3.2.1 MMC coating powders

The MMC coating powder mixture was comprised of nickel (Ni) and tungsten carbide (WC) powders. The details of these powder mixtures for the fabrication of Ni-WC MMC coatings are given below.

3.2.1.1 Nickel as Matrix phase

Due to the difference in physical and thermal characteristics, the solid solubility of nickel in aluminium is not more that 0.04%. Fortunately, when this amount exceeds, Al_xNi_y intermetallic phases are formed which provokes a significant increase in mechanical properties. Al_xNi_y based intermetallic compounds have been synthesized as a matrix composite material for reinforcing harder carbide phases. Various authors have added nickel as strengthening phase in laser claddings on aluminium alloys. Raw powder size used were 75-150 µm nickel powders from Wako (assay ≥99%).

3.2.1.2 WC as Particulate phase

Apart from alloying, the remarkable improvement in the wear resistance of the alloys can also be brought with the additions of hard ceramic particulate reinforcements. The addition of silicon carbide (SiC) particulates results in dissolution of the carbides under high heat input during laser treatment. Free carbon reacts with aluminium to form aluminium carbide phases that inflict detrimental effect on mechanical properties. In contrast to SiC, tungsten carbide (WC) has higher hardness and toughness, good radiation absorption and does not dissociate considerably during the laser treatment (Bartkowski et al., 2015). In the case of aluminum alloys, if the matrix phase of an MMC coating is not resilient, the added carbide phase will be drawn out of the matrix during the wearing process. An MMC coating with aluminium-nickel intermetallic as the metal matrix and WC as the hard-facing particles offers a unique combination of high hardness (WC), high toughness (Ni), good wear resistance, excellent thermal stability, and good wettability of Ni on the WC surface. The properties of coating such as micro-hardness, homogeneity and porosity are linked to the amount of WC particles present. In one study, volume fraction roughly above 50% WC resulted in porosity, whereas below this percentage, a crack-free homogenous clad layers were obtained (Tobar et al., 2006). Raw powder size used were 1-10 μm tungsten carbide from Sigma-Aldrich (assay ≥99%).

3.2.2 HMMC coating powders

The HMMC coating powder mixture was comprised of nickel and tungsten carbide powders but with the addition of graphite and TiO_2 powders. The details of these additives powder mixtures to fabricate HMMC Ni-WC-Graphite and Ni-WC-TiO_2 based coatings are given below.

3.2.2.1 Graphite as solid lubricant phase

Graphite not only serves as a solid lubricating phase in the hard composite matrix but it has been added in excess quantities in laser clad powder blends to synthesize in-situ reaction based hard coatings. Raw powder sizes used for graphite were in the range of 100-150 μm from Sigma-Aldrich (assay ≥99%).

3.2.2.2 TiO_2 as solid lubricant phase

TiO_2 rutile is a white odourless powder (< 5 μm) was added. TiO_2 was added with the purpose of improving wear resistance and reducing friction coefficient. Further to this increasing the heat capacity of melt pool and reducing crack formation due to the larger difference in thermal conductivities of Al, Ni and WC. Summaries of some of the selected physical, thermal and mechanical properties of all materials that have been used in this research work are given below Table 3.1.

Table 3.1: A summary of all material properties of all materials utilized

Physical Properties	***Counter-Body***	***Substrates***		***Matrix Phase***	***Carbide Phase***	***Additives***	
Material	**AISI 52100**	**AA5083**	**Al-17Si**	**Ni**	**WC**	**Graphite**	**TiO_2**
Density (g/cm3)	7.81	2.66	2.7	8.908	15.6	2.26	4.23
Elastic Modulus (Gpa)	200	70.3	81.2	200	686	7-26	288
Poison Ratio	0.3	0.33	0.33	0.31	0.22	0.17-0.23	0.29
Hardness Vickers (H_v)	848	87	92	65.06	2600	7–11	894–974
Melting Point (°C)	1424	570	507 - 649	1435-1446	2785–2830	3677	1843
Thermal Conductivity (W/mk)	46.6	121	134	70.2	110	85	11.8
Crystal System	FCC	FCC	FCC	FCC	HCP	HCP	Tetragonal

3.3 Experimental Methods

In this section, the substrate pre-processing, powder pre-placement, laser-processing steps will be discussed in details and the experimental methodology will be defined. The sample preparation, pre-deposition process for MMC and HMMC coatings and the laser surface treatment process are shown in the schematic drawing of Figure 3.1. In the following sections each of these steps will be discussed in details.

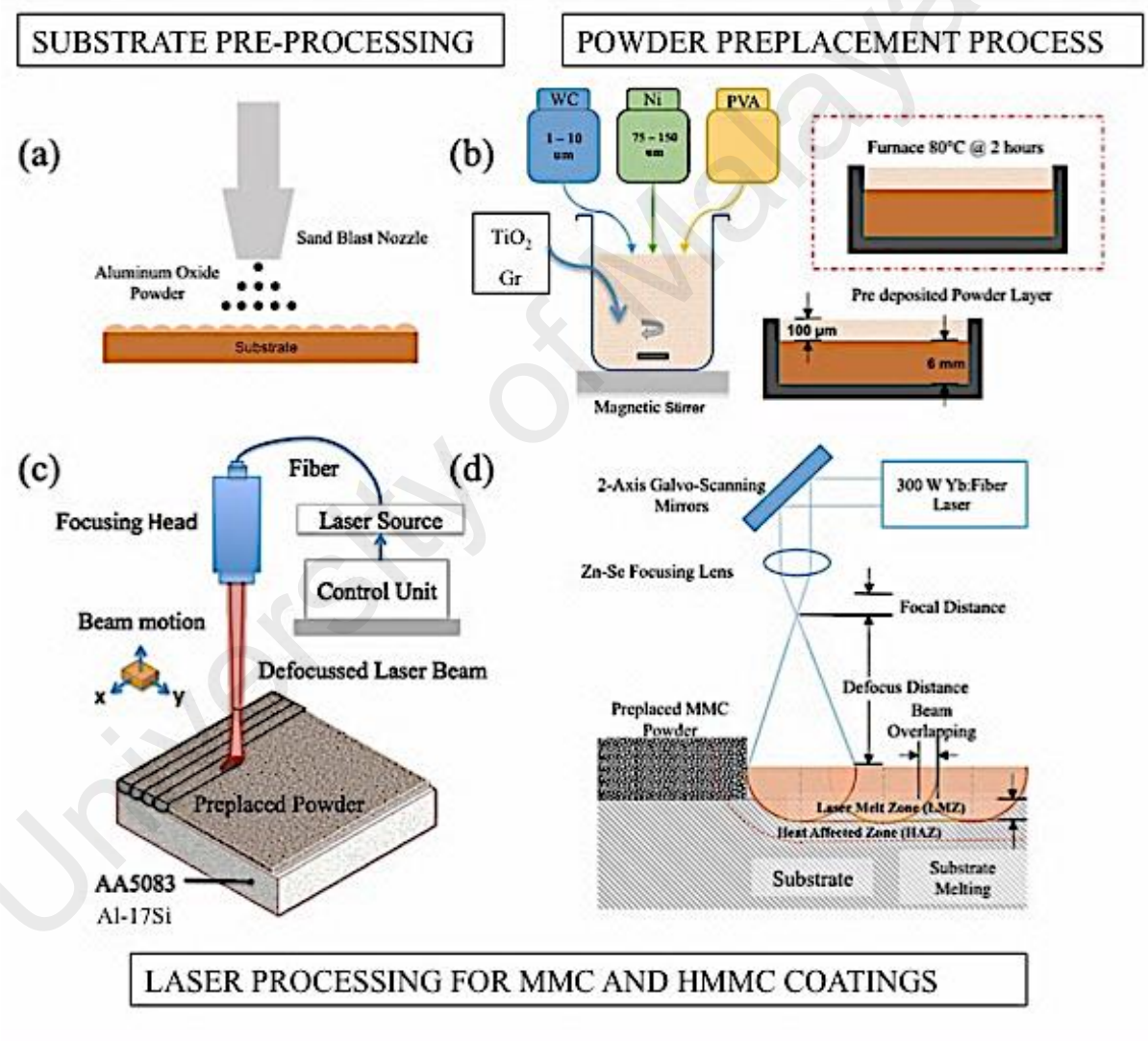

Figure 3.1: Schematics of (a) sandblasting of substrate; (b) Powder pre-placement; (c) laser processing 3D- view; (d) cross-sectional view

3.3.1 Substrate pre-processing

Treating aluminium alloys with laser possess two major constraints. The first factor being lower melting point of Al alloys and the second factor exhibited by aluminium alloys is the poor absorption of laser beam energy (0.07) even for laser light of ytterbium fiber laser radiation wavelength (λ = 1.07 μm, near infrared spectrum). This poor coupling of laser energy is by virtue of excellent reflectivity exhibited by Al due to the high density of free electrons present. Laser beam energy absorption is dependent on the band structure, incident beam wavelength and resistivity of metal. It is further a function of the size and nature of the plasma present above the melt pool, concentration and phase of volatile alloying elements in the metal and surface geometry (Ang et al., 1997). Hence, prior to laser processing, the controllable parameter, which is surface roughness of AA5083 and Al17Si, was therefore increased to 2 μm by sand blasting. The schematic representation of samples being sandblasted is shown in Figure 3.1(a). Not only does sandblasting increase incidence beam absorption, but also it removes the oxide scales and enhances pre-placed powder adhesion. Without dispersing and removing the oxide film, may result in the formation of a molten pool of aluminum enclosed in a skin of oxide and may cause additional porosity. The increase of surface roughness prior to laser processing assists in the earlier development of a keyhole and the enhanced absorption is ensured by the multiple reflections of the laser beam occurring in the cavity. In order to select range of parameters, initial laser surface treatments are carried out with a range of different the laser parameters resulting in crack free and least porous surfaces of low roughness were selected.

3.3.2 Powder Pre-placement

In order to avoid excessive melting of the substrate, alloying powder with higher melting points were pre-placed onto the substrate for composite surfacing as the pre-

placed powder layer exhibit far better absorption of laser energy than solid Al because of the pores present in the layer. Pre-placed powder layer due to its porous structure exhibit low thermal conductivity and the major portion of incident beam energy is absorbed in the layer (Lo et al., 2003) guaranteeing unnecessary melting of the substrate. The schematic representations of composite coating powder mixture pre-placement steps are presented in Figure 3.1(b). The powder to be pre-placed in proportion was mixed with acetone and thereafter mixed in a magnetic hot plate and stirred for one hour. A special die was prepared with internal depth of 6.1 ± 0.05 mm. Hence sample 6mm thickness inside the die gives a remaining thickness of around 100 µm. Therefore, the pre-placed coating was applied onto the sample with a pre-deposition thickness of around 100 µm under an ultrasonic bath apparatus for the vibrations to further assist and ensure thorough powders mixing. The binder was thereafter dried in the furnace (80º C for 2 hours).

3.3.2.1 MMC coating composition

The powder mixtures for laser composite surfacing, composed of 56 wt. % of Ni and 44 wt. % of WC. Raw powder size used were 1-10 µm tungsten carbide from Sigma-Aldrich (assay ≥99%) and 75-150 µm nickel powders from Wako (assay ≥99%). The MMC powders were preplaced on the wrought alloy AA5083 substrate.

3.3.2.2 HMMC coating composition

The powder mixtures for hybrid metal matrix coatings (HMMC) for the fabrication of Ni-WC-Graphite and Ni-WC-TiO_2 were composed of 56 wt. % of Ni and 44 wt. % of WC with the addition of graphite (100-150 µm) and TiO_2 (< 5 µm) in concentration of 5, 10 and 15 wt. % of the total Ni-WC mixture. The HMMC powders were preplaced onto the cast alloy Al-17Si substrate.

3.3.3 Laser Surface Processing

A 300 W, ytterbium (Yb) doped fiber-optic laser (Rofin-Star Fiber-300) is operated at a wavelength of 1070 nm in continuous wave mode. By employing ZnSe lens with focal length of 350mm and the smallest beam spot size of 79 μm, the laser beam was defocused onto the samples. The beam parameters were set in defocussed condition as larger melt pools develop at negative defocussing at a given spot size and heat input than for positive defocusing. Transverse electromagnetic mode (TEM_{00}) beam with an intensity profile of a Gaussian distribution was utilized to propagate the beam with the lowest divergence angle at any given beam waist diameter. Fiber lasers have typical beam quality M^2 value of less than 1.05 (mm.rad). This excellent beam characteristic sets apart Yb-doped fiber lasers from CO_2 and Nd: YAG lasers for achieving higher power densities with beam focusing on much smaller irradiation areas.

In LSC, an alloy or composite layer is fused onto the surface of a substrate with the assistance of a scanning laser beam (Figure 3.1(c) and (d)). The position of the laser beam can be controlled with the help of scanning galvo mirror system, whereas a computer numerical control (CNC) based or 3 stages motorized servo controller is utilized for controlling the axis of the worktable. LSC process can be performed out in two ways. In one process, clad material is preplaced onto the substrate as a powder bed and the laser beam scans the powder bed with some degree of overlapping between each bead to form a surface. For an applied power of 300 W, a max power density of about 6.12 MW/cm^2 can be obtained. The overlapping between each laser scan was kept at 30 % for all experiments carried out in this research.

3.3.3.1 Laser processing parameters for MMC coating

The selected parameters and their levels for the experimental trials are highlighted in Table 3.2. Subsequently, Taguchi's experimental trials were devised as L_{16} OA (3^4) to

realize the influence of processing parameters on the surface quality. The designed OA was taken into account due to its ability to examine the synergy among factors. The OA comprises of sixteen experimental trials with three distinct factors and four levels with ascending values of the experimental condition.

Table 3.2: Laser processing parameters and their levels employed for the fabrication of MMC Ni-WC coating

Parameters		**Levels**			
		1	**2**	**3**	**4**
A	Defocus distance (mm)	2	4	6	8
B	Laser power (W)	75	150	225	300
C	Scanning speed (mm/s)	3	6	9	12

3.3.3.2 Laser processing parameters for HMMC coatings

Based on the results obtained from the optimization of laser processing parameters as obtained in the fabrication of MMC coatings, the laser processing parameters were kept similar. However, the concentration of additives was changed. Both graphite and TiO_2 were added as concentrations of 5, 10 and 15 wt. % in Ni-WC coatings.

3.4 Characterization and microstructural analysis

The more popular surface characterization techniques include scanning electron microscope (SEM) and atomic force microscopy (AFM). Each of these techniques is efficient in providing atomic level quantitative analysis of the morphological properties coating surfaces. It is possible to characterize coating properties like surface roughness, particles size, matrix bonding and defects from these techniques.

3.4.1 Scanning Electron Microscopy (SEM)

Scanning electron microscopy is an analytical technique that exploits the electrons and x-rays generated by the interaction between an electron beam and specimen, to generate information on surface topography and specimen composition (Todokoro & Ezumi, 1999).

3.4.1.1 Beam-Specimen Interactions

The interaction between the beam electrons and the specimen atoms can occur by either an elastic or inelastic process. In the elastic process, a beam electron interacts with an atom and is deflected without losing a significant amount of its initial kinetic energy. The angle over which deflection occurs is large, ranging from average values of 2-5º up to 180º. Through this process, incident beam electrons can interact with the specimen and escape back out of the surface, being detected as "back scattered" electrons. During inelastic scattering an incident beams electron interacts with a substrate atom, giving up some of its initial kinetic energy. The beam electron is deflected, typically over angles <0.1º and continues into the sample. Of the various mechanisms of beam electron-substrate atom interactions generated through inelastic scattering, those most relevant to this work involve the transfer of energy to the outer band of electrons, and ejection of an inner shell electron from the atom by the beam electron. Following this interaction, the atom is in an "excited" state, relaxation of the atom resulting in the formation of "secondary" electrons and "characteristic x-rays" respectively (Goldstein, 2012).

3.4.1.2 Equipment Details

For microstructural analysis, optical and scanning electron microscopy, LCS samples were sectioned, polished by polishing and grinding machine. The samples were ground with 800 to 2200 grit SiC grinding paper and mirror polished with polycrystalline

suspended diamond liquid (Buehler). Subsequently, the samples were ultrasonically cleaned in acetone bath. Olympus BX 61 was used for light optical microscopy (OM). The surface morphology, cross-sections and elemental characterizations were investigated by scanning electron microscope (SEM) using “Hitachi 3400N” equipment integrated with energy dispersive x-ray spectroscopy (EDX). EDX quantitative analysis was performed on at least two different locations on each sample so as to ensure that the measurements were indicative of the entire microstructure as well as to assess the degree of sample variability.

3.4.2 Atomic Force Microscopy (AFM)

AFM is used to characterize coating morphology and surface information surfaces in both wet and dry environment. An atomic force microscope operates using a combination of principles from the scanning tunneling microscope and the stylus profilometer (Binnig et al., 1986). Surface morphology and/or surface interactions are measured based on the vertical deflection of the cantilever. The resolution of the AFM is determined by the sharpness of the tip and typically approaches the atomic scale. Thus, AFM may be used to provide high-resolution information regarding coating surface morphology in addition to other characteristics. Nevertheless, despite the many advantages of AFM and its success in characterizing coating surfaces a number of limitations exist.

3.4.2.1 Equipment Details

Atomic force microscopy “Digital instruments, USA” in contact mode was employed to identify surface topographical features of the wear scars. Measurements were performed on samples under ambient atmospheric conditions. The surfaces were imaged in tapping mode. Surface scan area was kept 30 μm by 30 μm and the data of surface roughness

(R_a) which is described as the arithmetic mean of the height deviations from profile mean value was extracted.

3.4.3 Xray-Diffraction (XRD)

X-ray Diffraction technique is primarily used for phase identification of crystalline materials and provides information pertaining to unit cell dimensions.

3.4.3.1 Fundamentals

X-ray Diffraction exploits the similarity in magnitude between the wavelength of X-rays and the inter-atomic spacing of the planes of atoms in crystals that enable X-rays to be diffracted (Warren, 1969). X-rays of a fixed wavelength are projected onto a sample. They penetrate the surface and are scattered by the regular array of planes of atoms, only those traveling out of the specimen in the same direction as the incident beam being detected. Within a crystal, diffraction occurs if the different distances travelled in the direction of the detector by the scattered x-rays are equal to a whole number of wavelengths. If so, the wavelengths reinforce each other through constructive interference, generating a very large intensity signal. If the variation in distance travelled does not fit this criterion, diffraction does not occur and the detector registers only a low “back ground” signal of X-rays randomly scattered in this direction. The peaks in intensity based on the inter-atomic spacing are characteristic for a specific set of planes of atoms for each compound. As a compound typically has several families of crystallographic planes that may diffract X-rays, several peaks occur at different incident angles. Scanning a range of incident angles and measuring the X-ray intensity generate a spectrum. The peak positions within this spectrum are related to the inter-atomic spacing, d, the wavelength of the X-rays, λ, and the angle of the incident beam to the surface. Bragg’s Law, equation 3.1, describes the relationship between these variables.

$$\lambda = 2d \sin\theta \quad (3.1)$$

Results are typically presented as spectra of intensity versus 2θ. Identification of the compounds within a spectrum is achieved by comparing the relative intensities of the various peaks and their peak positions with standard spectra within the JCPDS (Joint Committee on Powder Diffraction Standards) database (Klug & Alexander, 1954). Where mixtures of phases are present, the amount of each component is proportional to the intensity and the area underneath the peaks for that compound. Intensities for a given composition are dependent upon the atomic number for that compound and are also affected by the mass absorption of x-rays by the material (Cullity & Weymouth, 1957).

3.4.3.2 Equipment Details

The phase formation of the coating was investigated by X-Ray Diffraction (XRD) analysis using a "PANanlytical Empyrean" X-Ray diffractometer with a Cu-source (λ=0.15406 nm) using a Bragg-Bentano configuration, step-scanned in the 2θ range of 20°-80° with a scan rate of $0.1°s^{-1}$ and step size of 0.026°. The "PANalytical X'Pert HighScore Plus" software was utilized to check and match the XRD patters with the standards as obtained by Joint Committee of Powder Diffration and Standards (JCPDS).

3.5 Surface analysis

The surface properties that were measured in our experiments were mainly surface hardness and surface roughness.

3.5.1 Vickers Micro-hardness

The micro-hardness of the composite layer was measured on the top surface as well as along the cross-sectional plane by using Vickers micro-hardness tester "HMV Micro

Hardness Tester Shimadzu". Minimum 3 tests were carried out across each sample and the average values were collected. The duration of the hardness tests was set to 20 seconds and the applied load was 980.7 mN ($Hv_{0.5}$). All tests were performed in laboratory ambient temperature of 28˚C.

3.5.2 3D surface scan, surface profilometry and roughness Testing

In order to investigate the worn scar morphology, the "Alicona Infinite Focus" 3D scanning system was used for topographical observations. Moreover, the "Mitutoyo surftest SJ-210" tester was employed in order to examine the surface roughness.

3.6 Tribological Testing

The wear response of laser composite surfaced samples was compared to that of the as-received AA5083 by a high-frequency linear-oscillation "DUCOM ball-on-plate reciprocating friction monitor TR-282" under the dry sliding condition as presented in Figure 3.2**.** Dry-sliding tests were initiated when the counter-body ball slides to produce wear against a stationary plate. The normal load was applied using dual cantilever beam and the reciprocating motion was generated via an electro-motor. The load cell sensor recorded the kinetic frictional force, subsequently calculated in terms of root mean square value.

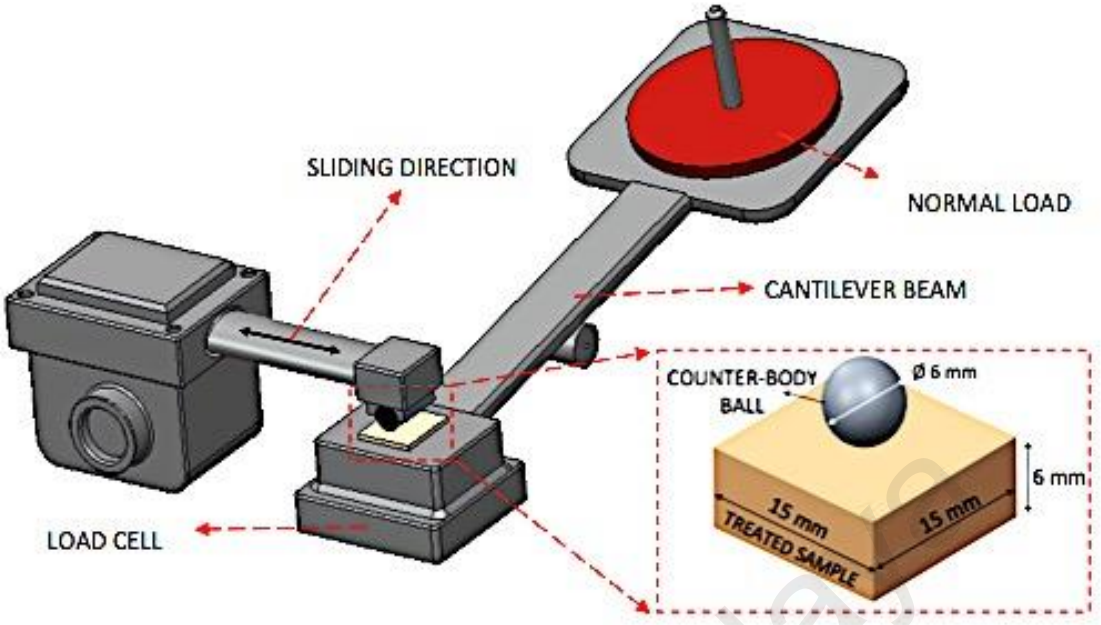

Figure 3.2: Schematic diagram of the ball on plate tribometer

The load cell sensor built into the tribo-tester recorded the kinetic frictional force. During the tribological test it was subsequently calculated in terms of root mean square value. The machine software displayed kinetic coefficient of friction (μ_k) value calculated based on recorded frictional force divided by the applied normal load. Besides, for weight loss measurement, a high precision weight balance "Denver Instrument" with an accuracy of 0.1 mg was utilized in order to calculate the wear rate. In order to analyse the damage mechanisms of coatings as well as substrates, high-carbon chromium 440C-bearing steel balls with lower thermal conductivity (24.2 W/m.k) were utilized as counter-body materials. The local heat dissipation decreases when the thermal conductivity of a material is lower thereby attaining critical transition temperature much earlier. At this critical temperature, the material re-crystallizes and thermally activated deformation starts, thus leading to severe wear. Therefore, to gain a better understanding of damage mechanisms, a contact of flat aluminum alloy against a moving steel counter-body was utilized in this study (Cai et al., 2010). The counter-

body balls of 6 mm diameter were obtained from AISI 440C quenched and tempered tool steel (800 H_V) containing C 1.2 wt%, Cr 16 wt%, Mn 1 wt%, Si 1 wt%, Mo 0.75 wt%, S 0.030 wt%, P 0.040 wt% and Fe balance. The laser treated samples were grounded after surface treatment to produce an acceptable smooth surface. Before commencement of wear testing, samples and balls were washed ultrasonically in acetone for 10 min.

3.6.1 Tribological testing parameters for AA5083 and MMC coating

The experiments for evaluating tribological properties for MMC Ni-WC coating were carried out under normal loads of 10, 20, 30 and 40 N with a reciprocating frequency of 10 Hz and amplitude stroke of 2 mm for 1 hour. The total sliding distance measured by machine software was 144 meters. For each applied normal load, three tests were carried out and the average value was taken. The samples were grounded to a surface roughness of 100 nm before tribo-testing.

3.6.2 Tribological testing parameters for Al-17Si and HMMC coating

The experiments for evaluating tribological properties for HMMC Ni-WC with varying concentrations of graphite and TiO_2 coating were carried out under normal loads of 20 N with a reciprocating frequency of 10 Hz and amplitude stroke of 2 mm for 1 hour. The total sliding distance measured by machine software was 144 meters. For each applied normal load, three tests were carried out and the average value was taken. Hence, a common load of 20N with similar testing conditions has been used for comparing MMC and HMMC coatings.

3.7 Comparative evaluations between MMC and HMMC coatings

In this research work comparative evaluations were made between MMC and HMMC coatings. The comparative evaluations were made keeping in view of similar processing

parameters to be utilized and similar tribological testing parameters being employed. The samples were laser processed with 150 W power, 4 mm defocus distance and 12 mm/s scanning speed that were the best combination parameters for best surface hardness for the case of MMC coatings. Hence, HMMC coatings were fabricated based on similar parameters. Additionally, the tribological testing parameters were also kept similar with normal applied loads of 20 N with a reciprocating frequency of 10 Hz and amplitude stroke of 2 mm for 1 hour. A complete summary of processing steps, characterizations involved and tribological evaluations made are now presented in Figure 3.3.

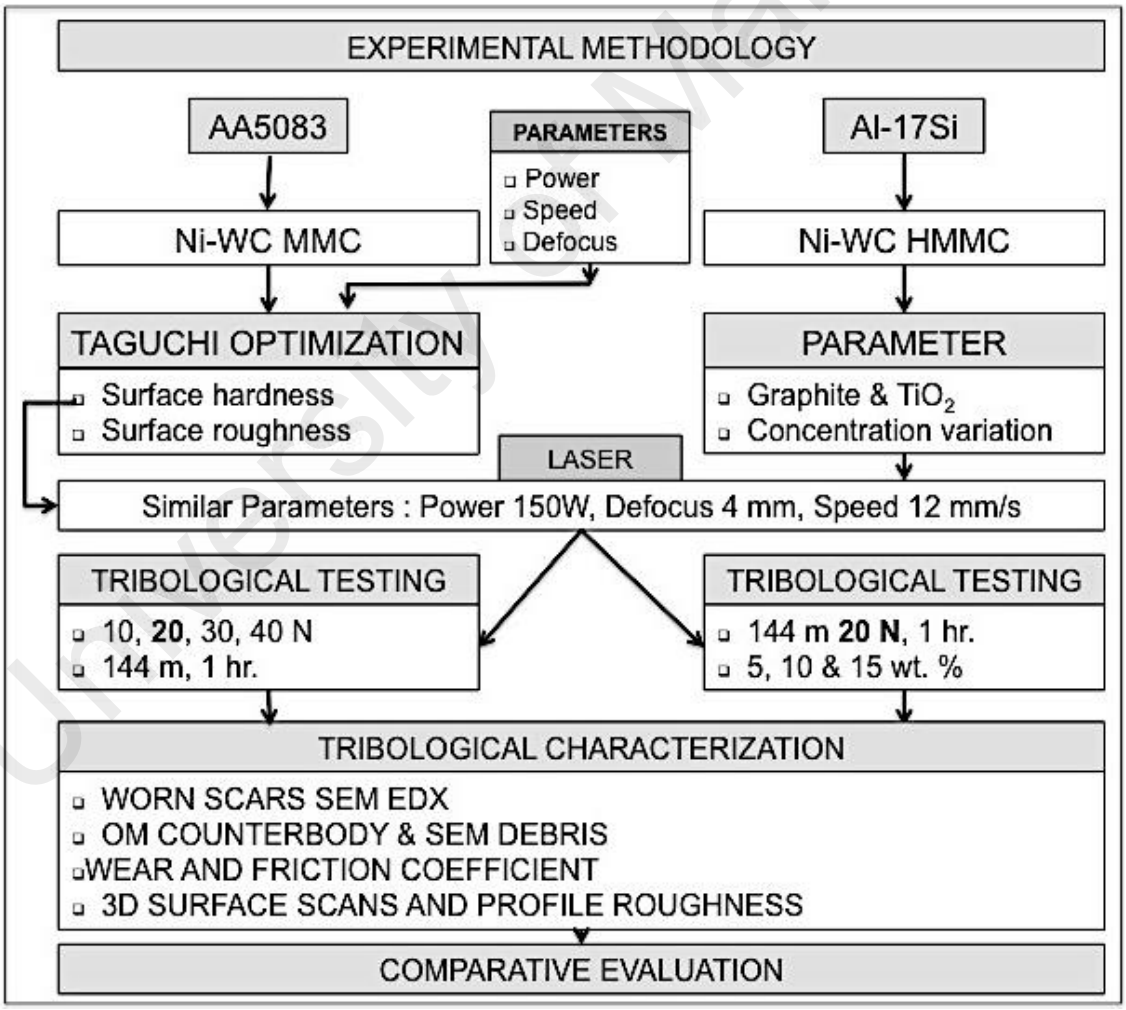

Figure 3.3: Block diagram depicting the key steps involved in the fabrication and characterization of the MMC and HMMC coatings

CHAPTER 4: RESULTS AND DISCUSSION

In this section, all results pertaining to optimization through Taguchi technique, mechanical performance of coatings and their tribological properties will be discussed.

4.1 Optimization of Ni-WC MMC coating

In this section, the design of experiment (DOE) in terms of Taguchi orthogonal array will be defined for our experiments. This will be followed by analysis of signal to noise ratio. A brief review of the effect of laser processing parameters on surface hardness and surface roughness shall be made and their influence shall be analysed quantitatively with the aid of PARETO ANOVA analysis technique.

4.1.1 Design of experiment

The selected parameters and their levels for the experimental trials are highlighted in Table 4.1. Subsequently, Taguchi's experimental trials were devised as L_{16} OA (3^4) to realize the influence of processing parameters on the surface quality. The designed OA was taken into account due to its ability to examine the synergy among factors. The OA comprises of sixteen experimental trials with three distinct factors and four levels with ascending values of the experimental condition.

Table 4.1: Laser processing parameters and their levels employed in this experiment

Parameters		**Levels**			
		1	**2**	**3**	**4**
A	Defocus distance (mm)	2	4	6	8
B	Laser power (W)	75	150	225	300
C	Scanning speed (mm/s)	3	6	9	12

4.1.2 Taguchi method: analysis of the signal-to-noise ratio

Subsequent to the identification of DOE orthogonal array, experiments were conducted using the Taguchi optimization method. The measurements were replicated three times for surface hardness and roughness and their values are recapitulated in Table 4.2. Following the experimental runs, data analysis was conducted for parameter optimization and to identify the statistically significant process parameters signal/noise (S/N) response analysis and Pareto ANOVA. For the sake of data analysis, Taguchi devised S/N ratio as the quality-determining factor for performance measurement. Instead of standard deviation, S/N ratio is applied as quantifiable value as with the decrease in mean values, standard deviation also decreases and vice versa. Depending on desired quality characteristics, S/N ratios fall into three distinct categories as nominal the better, smaller the better and larger the better. Therefore, smaller values are preferred in the case of surface roughness and higher values preferred for coating hardness. For the S/N ratio calculation measured in decibel, the "smaller-the-better" and "larger-the-better" characteristic formula was used to identify the combination of optimum factors to enhance the coating hardness and surface roughness respectively (Eq. (1) and (2)).

Smaller the better characteristics:

$$\frac{S}{N} = -10 \log \frac{1}{n} \left(\sum y^2\right) \tag{4.1}$$

Larger the better characteristics:

$$\frac{S}{N} = -10 \log \frac{1}{n} \left(\sum \frac{1}{y^2}\right) \tag{4.2}$$

Table 4.2: The measure values of surface hardness and roughness with their corresponding calculated S/N ratios

	Measured Surface Hardness (Hv)					Measured Surface Roughness (um)				
Exp	**1st**	**2nd**	**3rd**	**Avg.**	**S/N Ratio**	**1st**	**2nd**	**3rd**	**Avg.**	**S/N Ratio**
1	689	599	645	644	56.14	4.047	3.319	3.216	3.527	11.00
2	890	873	874	879	58.88	3.664	3.196	3.604	3.488	10.87
3	301	330	277	303	49.55	2.654	2.883	2.306	2.614	8.38
4	588	545	529	554	54.84	4.634	5.524	6.306	5.488	14.86
5	409	515	540	488	53.57	0.891	0.984	0.933	0.936	0.57
6	800	798	814	804	58.1	2.792	3.438	6.522	4.251	13.16
7	696	781	684	720	57.11	1.919	1.921	1.97	1.937	5.74
8	556	551	589	565	55.03	5.121	2.618	6.574	4.771	14.05
9	381	367	320	356	50.95	1.186	1.463	0.861	1.17	1.55
10	888	872	885	882	58.91	0.991	0.959	1.983	1.311	2.89
11	653	657	689	666	56.47	9.627	10.365	12.219	10.737	20.66
12	533	526	515	525	54.4	12.962	13.07	12.394	12.809	22.15
13	311	485	401	399	51.59	2.685	2.796	3.466	2.982	9.55
14	605	733	721	686	56.63	1.395	2.359	1.969	1.908	5.79
15	401	450	424	425	52.54	1.835	1.504	2.624	1.988	6.2
16	290	303	310	301	49.56	3.926	2.189	2.317	2.811	9.31

Where n is the number of observations performed for each sample, which is three; and y is the measured response value of i^{th} experiment. The S/N values serve as performance measurement, which enhances processes that are insensitive to noise factors. Table 4.2 also highlights computed (S/N) ratios for surface roughness and

surface hardness, while Table 4.3 summarizes the calculated ratio and response values for each level against each parameter that are plotted in Figure 4.1. The S/N response value *Ai* as shown in Figure 4.1(a) and (b) was calculated by taking average values of all the S/N ratios indicated in Table 4.2. Hence, calculations were made similarly for the remaining response values. For instance, to obtain the optimum laser parameters for higher hardness, the desired characteristic "larger the better" entails that the maximum S/N ratio will result in the lowest noise in the experimental setup. As illustrated Figure 4.1(a) and Table 4.3, the significant parameters affecting surface hardness are laser power, defocussing distance followed by scanning speed. The optimum parameter combination, to obtain higher value of surface hardness are laser power (B2), defocus distance (A2), and scanning speed (C4). Thus, the optimum recipe for higher surface hardness becomes B2A2C4 within the examined range. Similarly the optimal combination for a lower surface roughness comes out to be B1C3A4.

Table 4.3: The (S/N) response values of laser processed AA5083 for surface hardness and for surface roughness

Parameters	**a) Calculated S/N Ratios for surface hardness**			
	1	**2**	**3**	**4**
Defocus Distance (mm)	54.85	55.95	55.18	52.58
Laser power (W)	53.06	58.13	53.92	53.46
Scanning Speed (mm/s)	55.07	54.85	53.04	55.61
Parameters	**b) Calculated S/N Ratios for surface roughness**			
	1	**2**	**3**	**4**
Defocus Distance (mm)	11.28	8.1	11.81	7.71
Laser power (W)	5.38	8.18	10.25	15.09
Scanning Speed (mm/s)	13.53	9.66	7.45	8.26

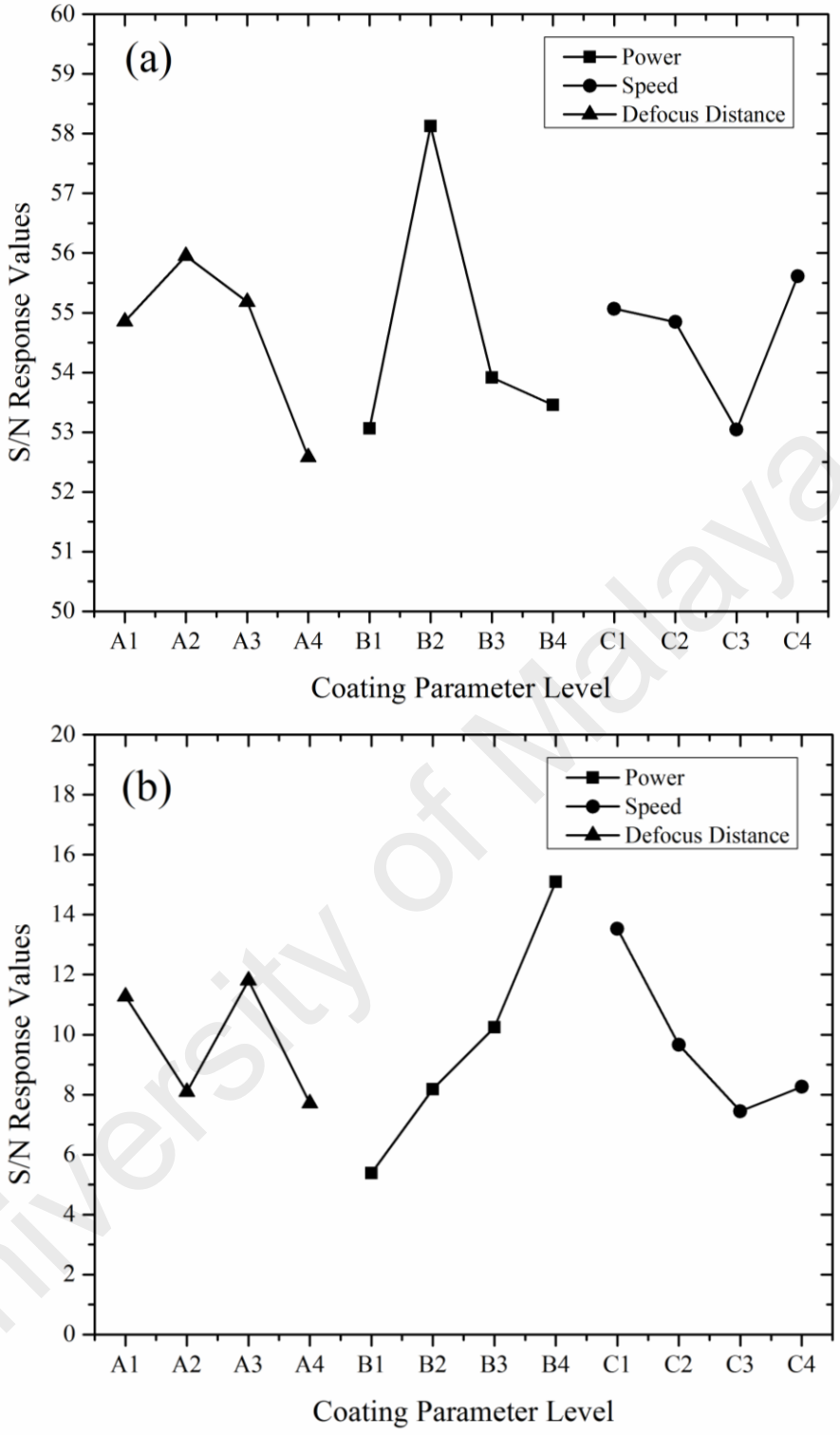

Figure 4.1: The signal to noise (S/N) response graph for (a) surface hardness, (b) surface roughness

4.1.3 Influence of processing parameters on hardness and roughness

The selections of processing parameters are essential for fabricating surfaces to reduce both friction and wear. For improving surface hardness, the WC particle distribution should be uniform and density in the melt pool should be greater. During laser processing, the pre-placed powders will mix with the molten pool at the substrate surface through fluid flow mechanism by convection current. The degree of mixing will depend on the laser material interaction time and heat input. From experimental and optimization results, the effect of Ni-WC coating on AA5083 was observed in dissimilar conditions to produce the best surface hardness and is obtained with parameter and their levels combination of B2A2C4. Surface hardness increases when laser power was reduced from 300W to 150W and decreases when power decreases from to 150 W to 75 W. At higher heat inputs, larger depths of alloyed zone are created. Hence, WC particles sink and leave the surface of the substrate with lesser distribution of hard particulates. Therefore, lower applied power and higher scanning speeds will create smaller depths of melt pool and WC particles will float onto the surface with higher distribution in the metal matrix. Under these conditions, WC particles gain enough interaction time with lesser surface tension gradients to prevent particle agglomeration (Staia et al., 2001).

Similarly, Taguchi design of experiment identified the significant variables for surface roughness being applied power and scanning speed. The outcome of Ni-WC coating deposited on AA5083 was regarded in various conditions for obtaining lower surface roughness with the best parameter combination of B1C3A4. As it can be observed in Figure 4.1(b), the surface roughness of specimens was lowest when power was 75 W. Surface roughness decreased when scanning speed was increased from 3 mm/s to 9 mm/s but increases when scanning speed increases from 9 mm/s to 12 mm/s. This

directs to the fact that average surface roughness increases with increasing applied power and decreasing scanning speed (Nath et al., 2012). The increase in surface roughness results from the rapid intermixing and melting of powder mixtures due to higher energy density (= power density × beam diameter/scan speed). Higher power leads to higher heat input. The resulting evaporation effect thence produces rougher surfaces. The effect of beam defocus distance when alloying pure aluminium with nickel has also been reported (Das, 1994). The surface roughness is generated due to the formation of ripples. The height of these ripples is a function of the fluid flow due to shear stresses in the melt pool caused by gradients in temperature and surface tension. It was demonstrated that with increasing defocus distance, the power density decreases, and ripples height decreases, which results in a decrease in surface roughness after solidification. The defocussing of laser beam assists in formation of greater concentrations of alloying elements in the melt pool as the temperature gradient decreases causing a decrease in surface tension gradients.

4.1.4 Pareto-ANOVA Analysis

Following S/N response analysis, the results were analyzed using ANOVA statistical analysis of variance with a Pareto chart to demonstrate and analyze data the effect of control parameters in Ni-WC coating process. Pareto ANOVA determines the percentage of factor influence on each parameter and determines which parameters are significant in determining the predicted value to be assessed (Aghayan & Narayanswamy, 2015). The main reason for employing this analysis was to investigate the Ni-WC coating parameters to obtain higher hardness, which in turn leads to superior surface integrity and wear resistance. The sum of the squares of the differences between the levels of A and S_a, for instance, is as follows:

$$S_a = (A_1 - A_2)^2 + (A_1 - A_3)^2 + (A_2 - A_3)^2 \quad (4.3)$$

Thereafter, S_b and S_c were also computed in a similar manner. The contribution ratio was computed from the percentage of the sum of squares of differences for each parameter to the total of the sum of squares of differences. Thereafter, the Pareto diagram was charted based on ascending order of contributing factors with significant factors starting from the origin of the Pareto diagram, that sum up to more than 90%. Pareto ANOVA values for the resultant coating hardness and roughness are tabulated in Table 4.4 and Table 4.5**,** with S/N values taken from Table 4.3. As illustrated in Table 4.4, laser power (factor B, 62.31%), defocussing distance (factor A, 23.71%), and scanning speed (factor C, 13.97%) have a prominent effect on surface hardness. The best combination for higher surface hardness is thus B2A2C4. Similar results were also detected with the ones acquired via (S/N) response analysis. Similarly, Table 4.5 implies that laser power (factor B, 58.77%) is the most influential parameter that affects the surface roughness. This is trailed by scanning speed (factor C, 25.51%) and defocussed distance (factor A, 15.72%). The best combination for lower surface roughness is thus B1C3A4, which also coincides with the results found through (S/N) response analysis. At this point, confirmation test was carried out to validate the best parameter combinations and values measured are reported as an average of three runs. From the confirmation test, the surface hardness value obtained is 953 H_V, showing an enhancement of 9.27% as compared with values measured during the experiments. The surface roughness result achieved from this confirmation test is 0.81 um, an improvement of 13.14% when compared to the lowest value reached during the experiments. It is also stressed that the optimal levels obtained from these experimental results are only near optimal, having taken the parameters and their levels into consideration.

Table 4.4: Pareto-ANOVA analysis for surface hardness

Factor and interaction		**Defocus Distance (A)**	**Laser Power (B)**	**Scanning Speed (C)**
Summation at the level of input parameter	1	54.85	53.06	55.07
	2	55.95	58.13	54.85
	3	55.18	53.92	53.04
	4	52.58	53.46	55.61
Total of summation at factor level		218.57	218.57	218.57
Summation of squares of differences (S)		25.24	66.32	14.87
Total of summation of squares of differences St=Sa+Sb+Sc		106.43		
Contribution ratio (%)		23.71	62.31	13.97
Pareto Diagram				
Cumulative contribution ratio		62.31	86.03	100.00
Optimum combination		B2	A2	C4
Remarks on optimum condition	The significant factors are chosen from the left-hand side in the above Pareto diagram which cumulatively contribute up to 90 %			
Overall optimum conditions for all factors	B2A2C4			

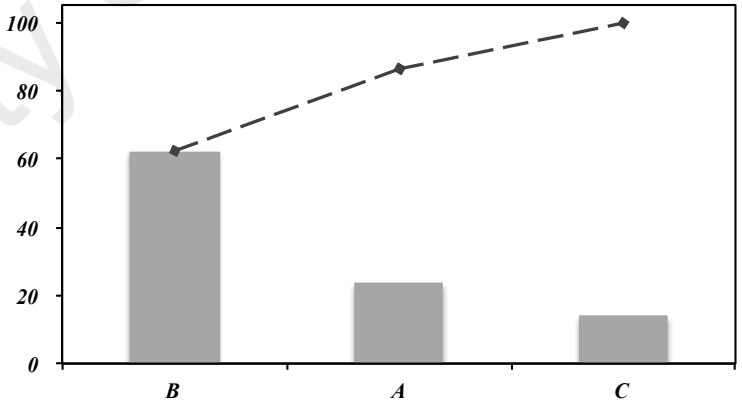

Table 4.5: Pareto-ANOVA analysis for surface roughness

Factor and interaction		**Defocus Distance (A)**	**Laser Power (B)**	**Scanning Speed (C)**
Summation at the level of input parameter	1	11.28	5.38	13.53
	2	8.10	8.18	9.66
	3	11.81	10.25	7.45
	4	7.71	15.09	8.26
Total of summation at factor level		38.90	38.90	38.90
Summation of squares of differences (S)		53.85	201.32	87.38
Total of summation of squares of differences St=Sa+Sb+Sc		342.55		
Contribution ratio (%)		15.72	58.77	25.51
Pareto Diagram 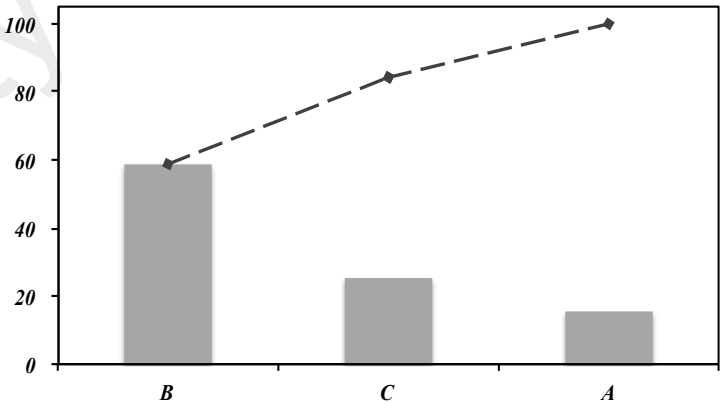				
Cumulative contribution ratio		58.77	84.28	100.00
Optimum combination		B1	C3	A4
Remarks on optimum condition	The significant factors are chosen from the left-hand side in the above Pareto diagram which cumulatively contribute up to 90 %			
Overall optimum conditions for all factors	B1C3A4			

4.2 Microstructure and Phase identification

4.2.1 Microstructure and Phase identification of Ni-WC coating

Laser composite surfacing of pre-placed Ni-WC coating led to the dispersion of WC carbide particles in strong intermetallic NiAl fine-grained matrix**.** Figure 4.2 shows X-ray diffraction plot of laser composite coating on AA5083 obtained from "Panalytical Xpert Pro". XRD scan was carried across the cross-section of the sample. Upon XRD spectrum evaluation, the presence of WC, Al, Al_3Ni, Al_3Ni_2, NiAl, Ni_3Al and Ni phases was revealed.

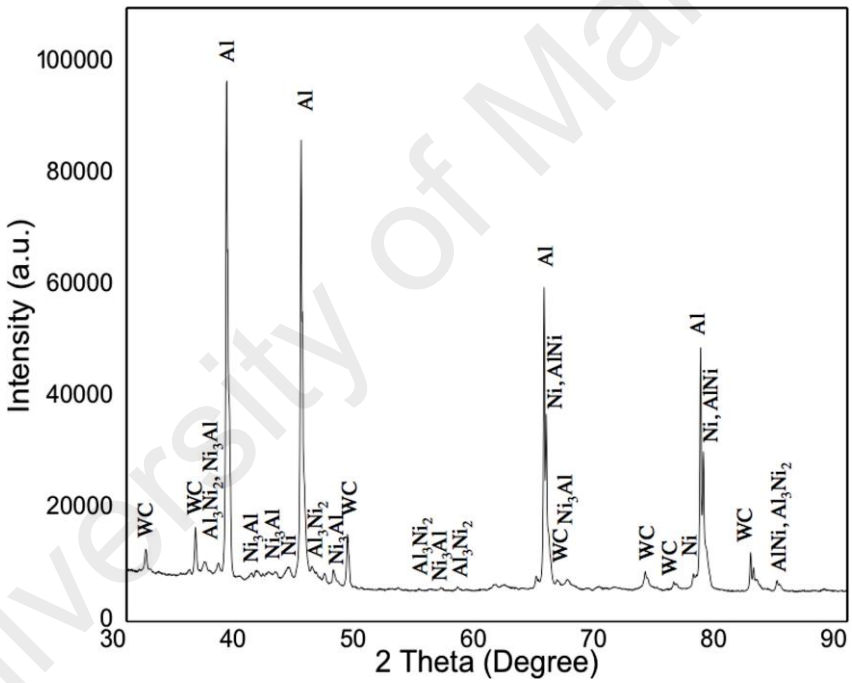

Figure 4.2: The XRD pattern of laser composite surfaced AA5083 with Ni-WC coating

In order to reveal the coating interface, the samples were sectioned, polished and etched using Keller's re-agent (100ml distilled water + 5ml HNO3 + 3ml HCl+2ml HF). It is to be noted that the cross-sectional clad remained free from coating interfacial cracks and defects. As an example, the cross-sectional image of an approximately 400μm wide and 200μm deep single pass scan track is presented in Figure 4.3. The cross-sectional image

and XRD scan conditions match to those provided in experiment number 16 as presented in Table 4.2. By employing an overlapping ratio of 20%, these tracks were scanned simultaneously. The SEM overview of the Ni-WC coating lay on the AA5083 substrate is showed in Figure 4.4.

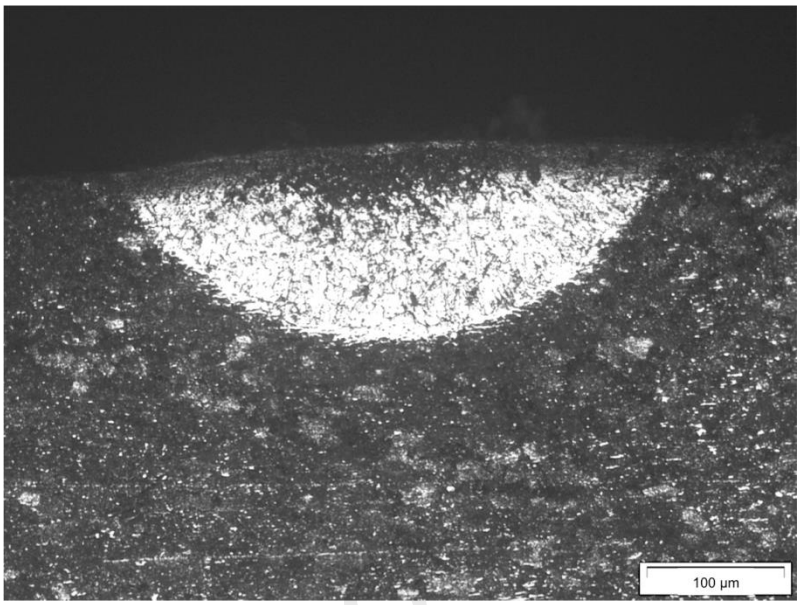

Figure 4.3: Cross-sectional optical micrograph of single scanned track

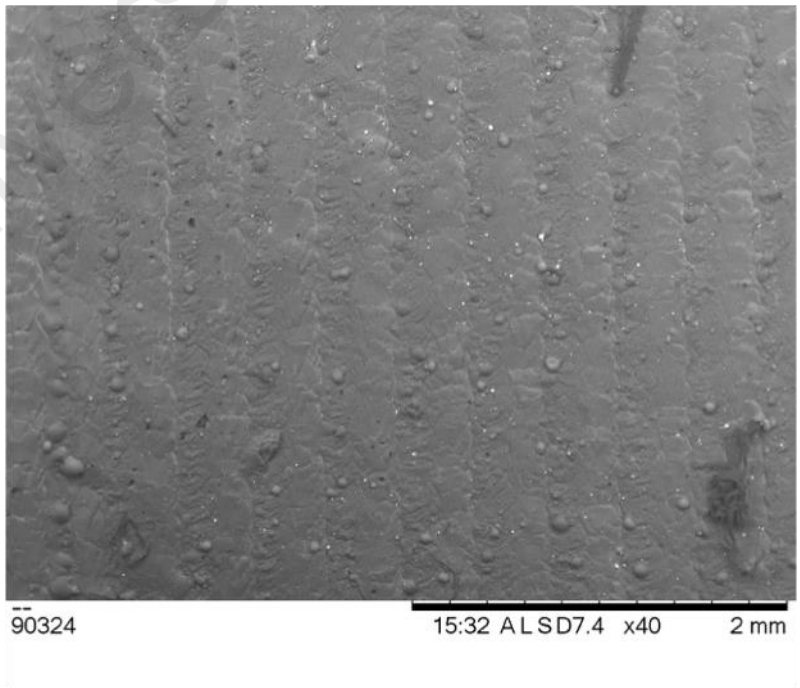

Figure 4.4: SEM overview of overlay of Ni-WC coating

Combining with corresponding micro compositional analysis as showed in Table 4.6, EDS spectrum at area A, B, C and D identified various phases present in the marked SEM micrographs of the top and middle sections of the composite which have been showed in Figure 4.5(a) and (b) respectively. There were white block like WC particles that were distributed in the fine dendritic phase within the matrix phase. As showed in the SEM magnified view in Figure 4.5(a), in the uppermost section of the alloyed surface, there exist coral-like eutectic dendrites. These dendrites at higher image magnification appear as fine laminar structures with inter-lamellar spacing. The inter-lamellar spacing was in the order of a fraction of micrometres. EDS spectrum at area A as showed in Figure 4.5(a), confirms that these coral-like patches comprised mainly of Al_3Ni phase. Furthermore, the SEM micrographs in Figure 4.5, and EDS scans at area A, C and D gives the indication that higher concentration of aluminium exists in the near surface regions, whereas the concentration of Ni and W tends to increases as they sink towards the middle. In addition, the carbide phases present were distributed within the coating and had sharp corner particles like structure that were also reported (Man et al., 2001). It was concluded in their findings that difference in powder composition, material densities, melting points of phases, the viscosity of the metals plays a significant part in the distribution of Al-Ni intermetallic and WC particles throughout the depth of the composite surface.

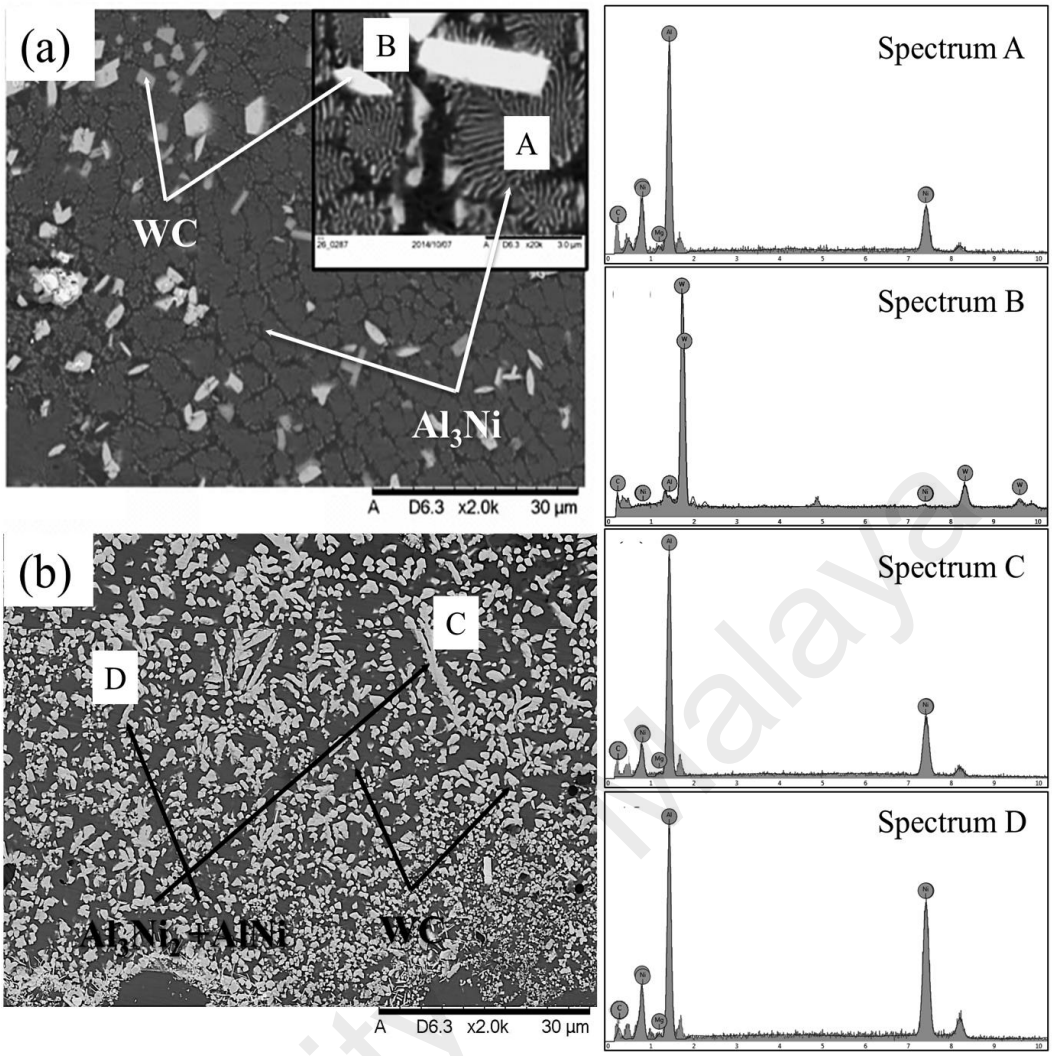

Figure 4.5: SEM cross sectional images along with EDS spot scanning for (a) top section of Ni-WC coating with a magnified view of Al_3Ni dendritic structure, (b) middle section containing dendrites of Al_3Ni_2 and AlNi

Table 4.6: The EDS chemical composition (at. %) by spot scan along with corresponding XRD phases detected.

Spot Location	Al	Ni	W	C	Mg	XRD Phase
A	52±4	45±3	-	3.8	<1	AlNi
B	63±2	37	-	7.1	1.1-1.4	Al_3Ni_2
C	76±3	24±2	-	6.5	<2	Al_3Ni
D	1-2	1-2	46.4	51.7	-	WC

EDX area mapping identified various phases present in the marked SEM micrographs of top and middle sections of the composite that have been showed in Figure 4.6. Figure 4.6 indicates that the major concentrations of alloying elements are present in the middle section of the melt pool. This is due to the density of tungsten carbide ceramic being 5.78 times higher that of aluminium metal. The difference in densities contributes to the sinking of heavy WC particulates into the molten aluminium pool. Hence, there exists a secondary region wherein higher concentrations of both nickel and WC are present in the midsection of the alloyed layer. The fine dendritic structure of Ni-Al intermetallic with interdendritic spacing between 1–2 μm was present. As showed in EDS spectrum of point C and D in SEM micrograph of Figure 4.5(b) dendrites of Al_3Ni_2 along with eutectic phase of Al_3Ni_2 and AlNi are present. These dendrites with a higher concentration of nickel in the aluminium matrix have promoted the hardness of the coating. The presence of these dendrites and higher concentration of WC round particles in the subsurface region has been reported in other studies as well (Man et al., 2004). The higher concentrations of WC particles in subsurface regions may be advantageous in a way that under real industrial applications, the claddings are machined to eliminate the irregularities and humps formed during material processing. Therefore, the removal of the top portion will result in the exposure of a harder coating with a higher concentration of particulates (Jendrzejewski et al., 2009).

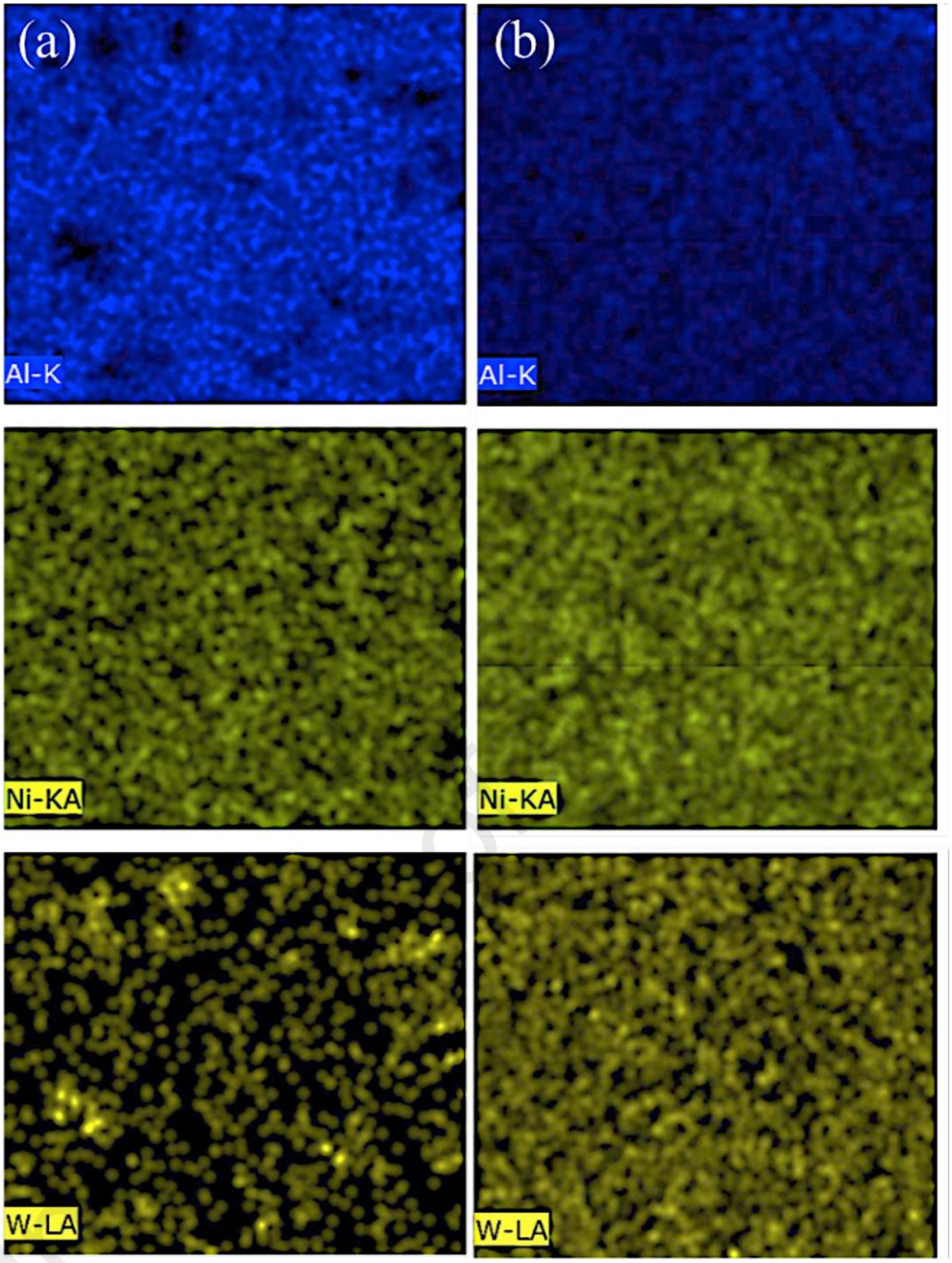

Figure 4.6: EDS area scanning for (a) top section of Ni-WC coating with, (b) middle section

4.2.2 Microstructure of substrate Al-17Si hypereutectic alloy

The microstructure of LM 28 Al-17 wt. % Si hypereutectic piston alloy as showed in Figure 4.7 comprises of coarse polyhedral shaped primary silicon crystals in eutectic matrix. EDS area mapping as showed in Figure 4.8 shows Al and Si distribution.

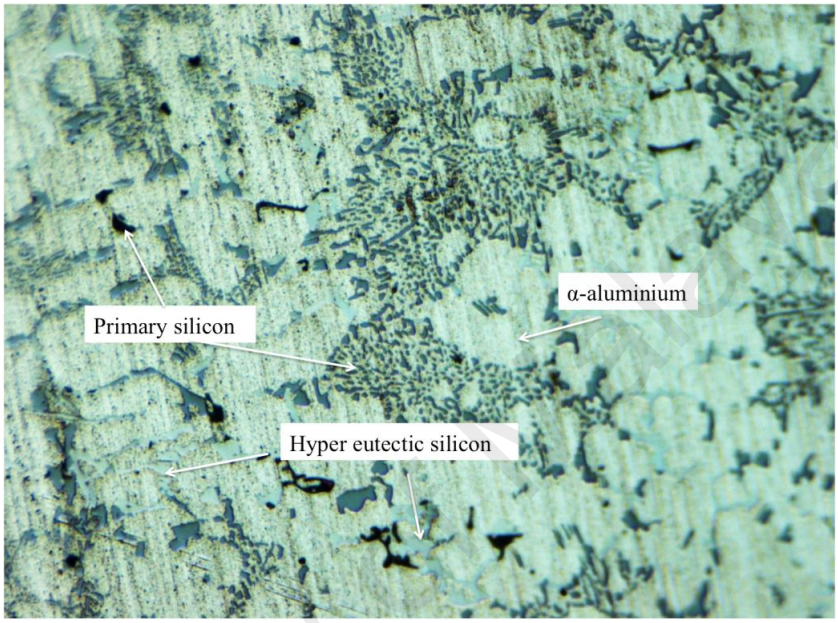

Figure 4.7: Optical micrograph of Al-17 wt. % hypereutectic piston alloy at 20X magnification.

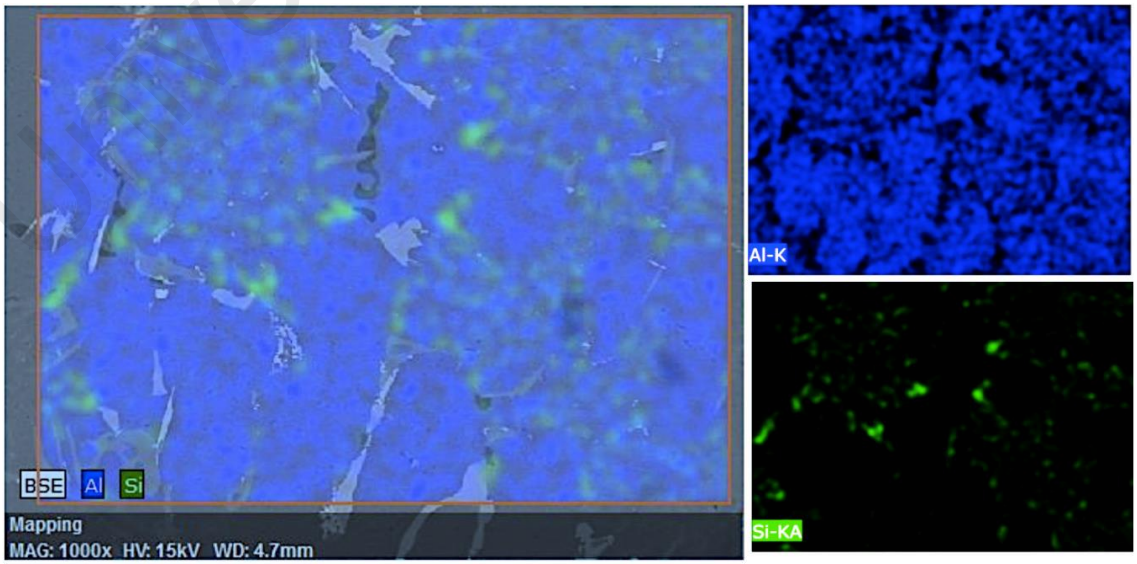

Figure 4.8: SEM and EDS area mapping of Al-Si hypereutectic alloy

4.2.3 HMMC coating deposited on Al-17Si

As an example, the cross-sectional SEM micrograph of Ni-WC-5 wt. % graphite coating deposited on Al-17Si substrate is showed in Figure 4.9. Simultaneous tracks with an overlapping percentage of 20% were scanned to obtain a coating thickness greater than 200 μm were obtained with each overlay being 400 μm wide. Furthermore, Figure 4.10 shows the cross-sectional substrate to coating interface. It is visible that the coating interface is free from defects such as oxides and cracks that may be formed. However, some forms of porosities were inevitable. An SEM overview of the Ni-WC-5 wt. % graphite coating laid on Al-17Si alloy is given in Figure 4.11.

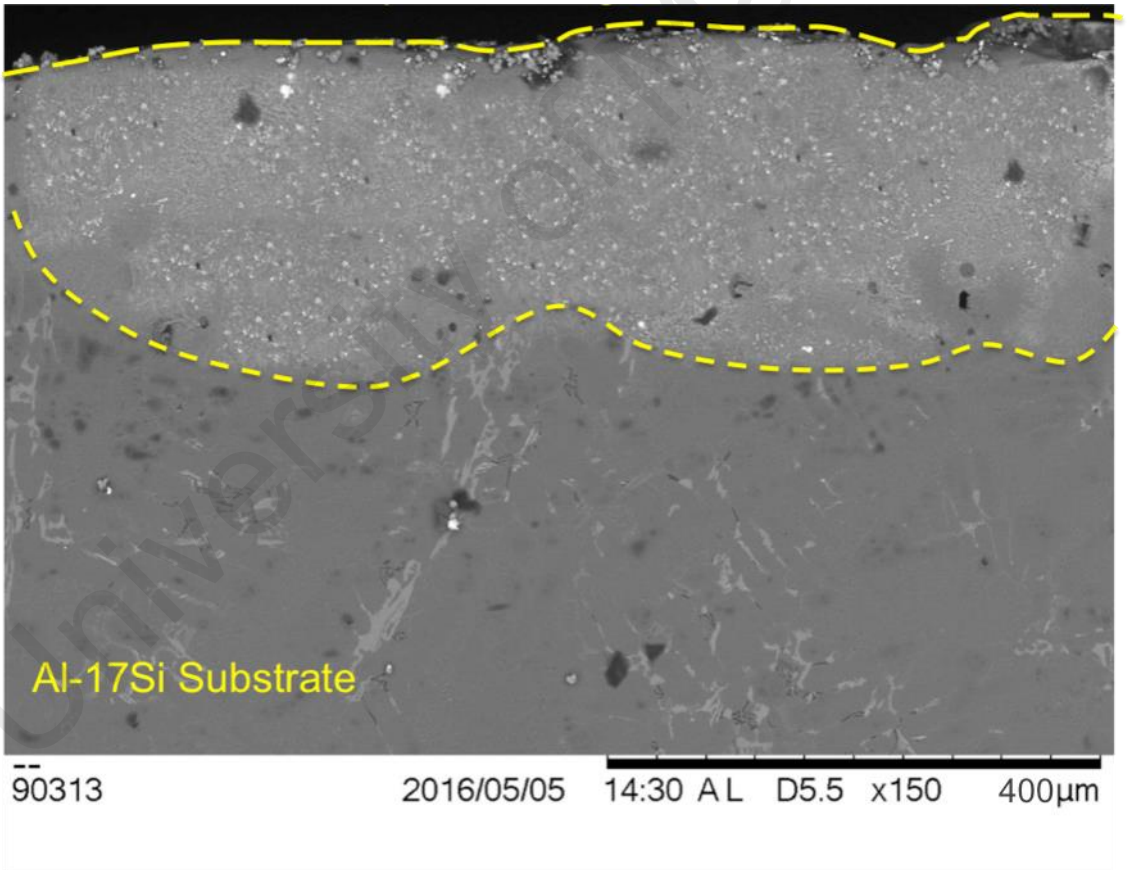

Figure 4.9: SEM cross-sectional view of laser composite surfacing of Ni-WC-graphite based composite coating deposited on Al-17Si Substrate

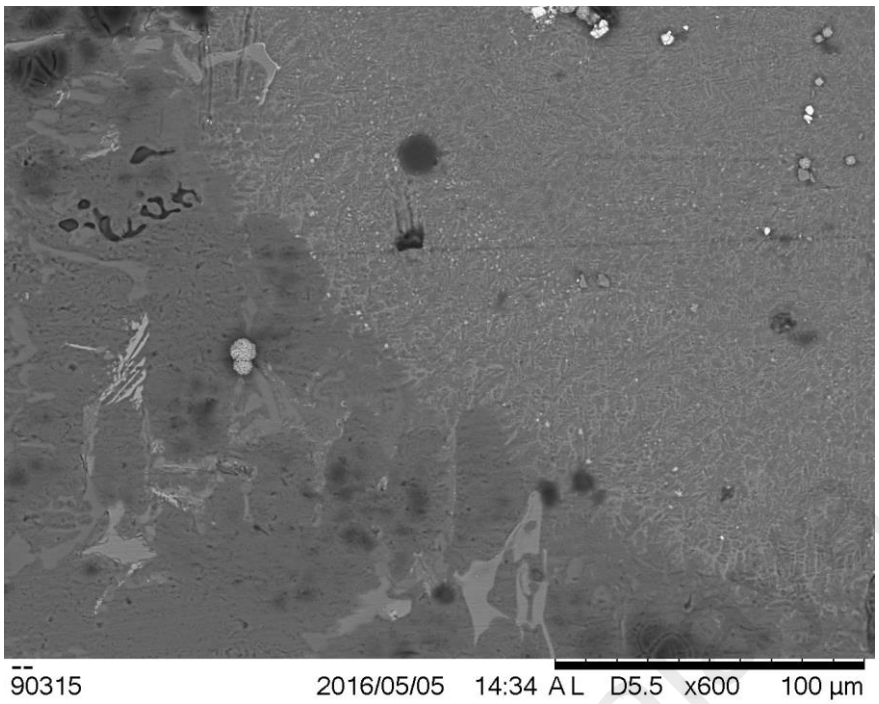

Figure 4.10: SEM cross-sectional view of substrate/coating interface of Ni-WC-graphite based composite coating deposited on Al-1Si Substrate

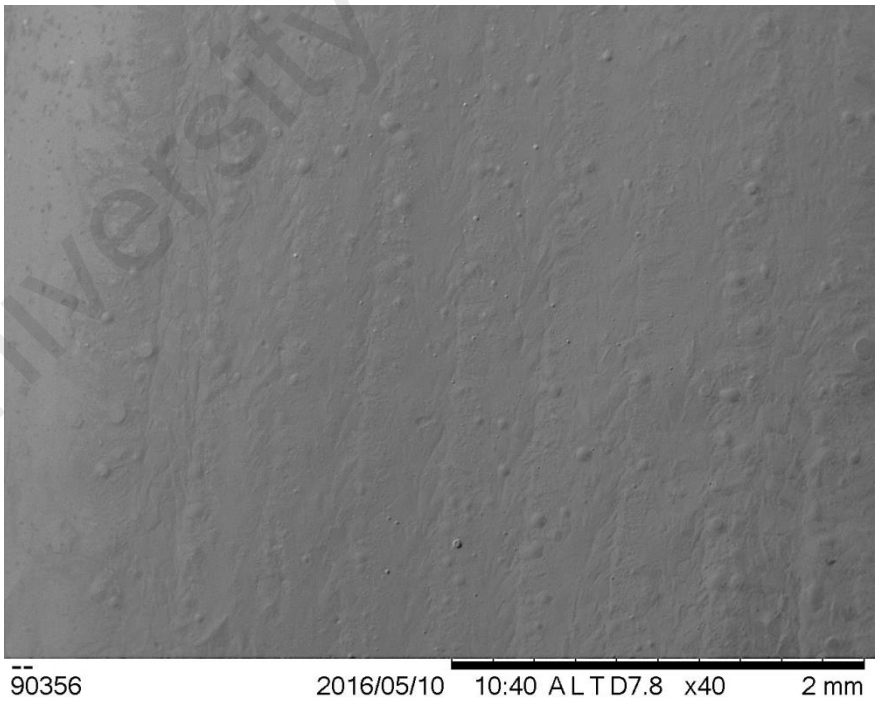

Figure 4.11: SEM overview of overlay of Ni-WC-graphite coating overlays

4.2.4 Phase identification of Ni-WC-Graphite coating

The X-ray diffraction pattern of Ni-WC-graphite composite coating with varying concentration of graphite content is shown in Figure 4.12. Since the 2θ scan was carried out on the metallographic sample cross-section, hence visible higher intensities peaks of Al and Si are present. The coating is composed of WC phase embedded in the Al-Ni intermetallic phase. The intermetallic phase was formed based on the concentration of the nickel in the coating comprising of AlNIi, Al_3Ni, Al_3Ni_2, Ni_3Al and an oxide form of nickel aluminide Al_2NiO_4 was found to be present. It is observed that characteristics reflection of the graphite phase in the form of carbon (C) is also present which increases in intensities as graphite content is raised as depicted in Figure 4.12(a), (b) and (c). Some of the reflections comprise of double peaks or peaks with shoulders wherein multiple compounds are formed are the same is presented in the Figure 4.12. The addition of untransformed graphite has been reported in open literature (Choudhury et al., 2008).

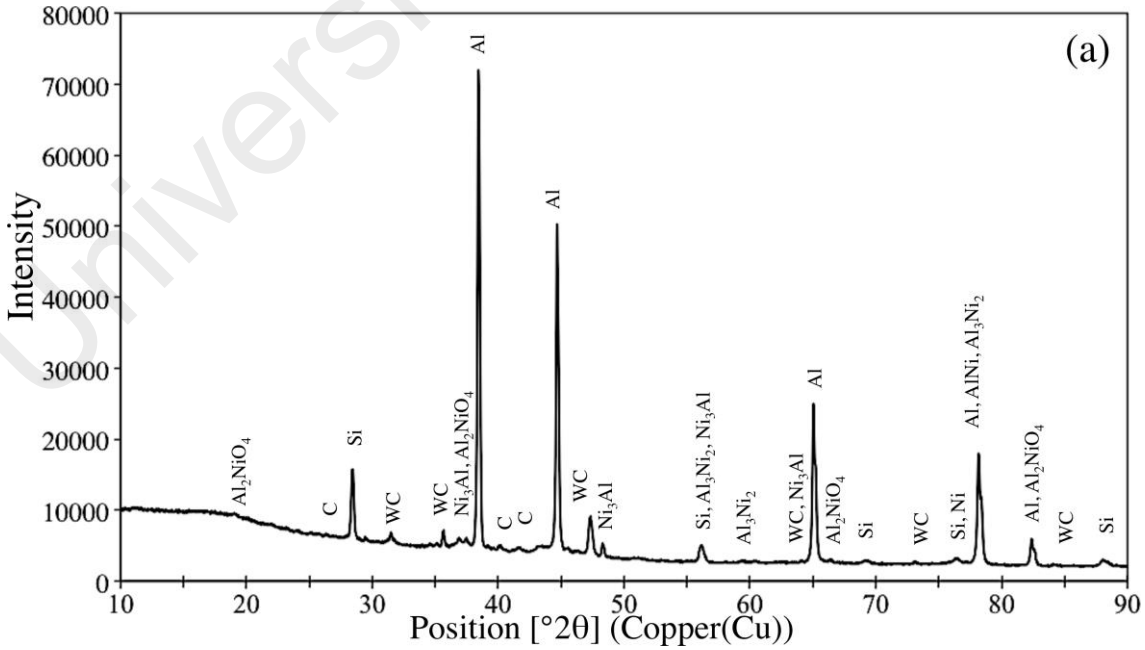

Figure 4.12: The X-ray diffraction spectrum for Ni-WC coating with graphite content (a) 5 wt. % (b) 10 wt. % and (c) 15 wt. %

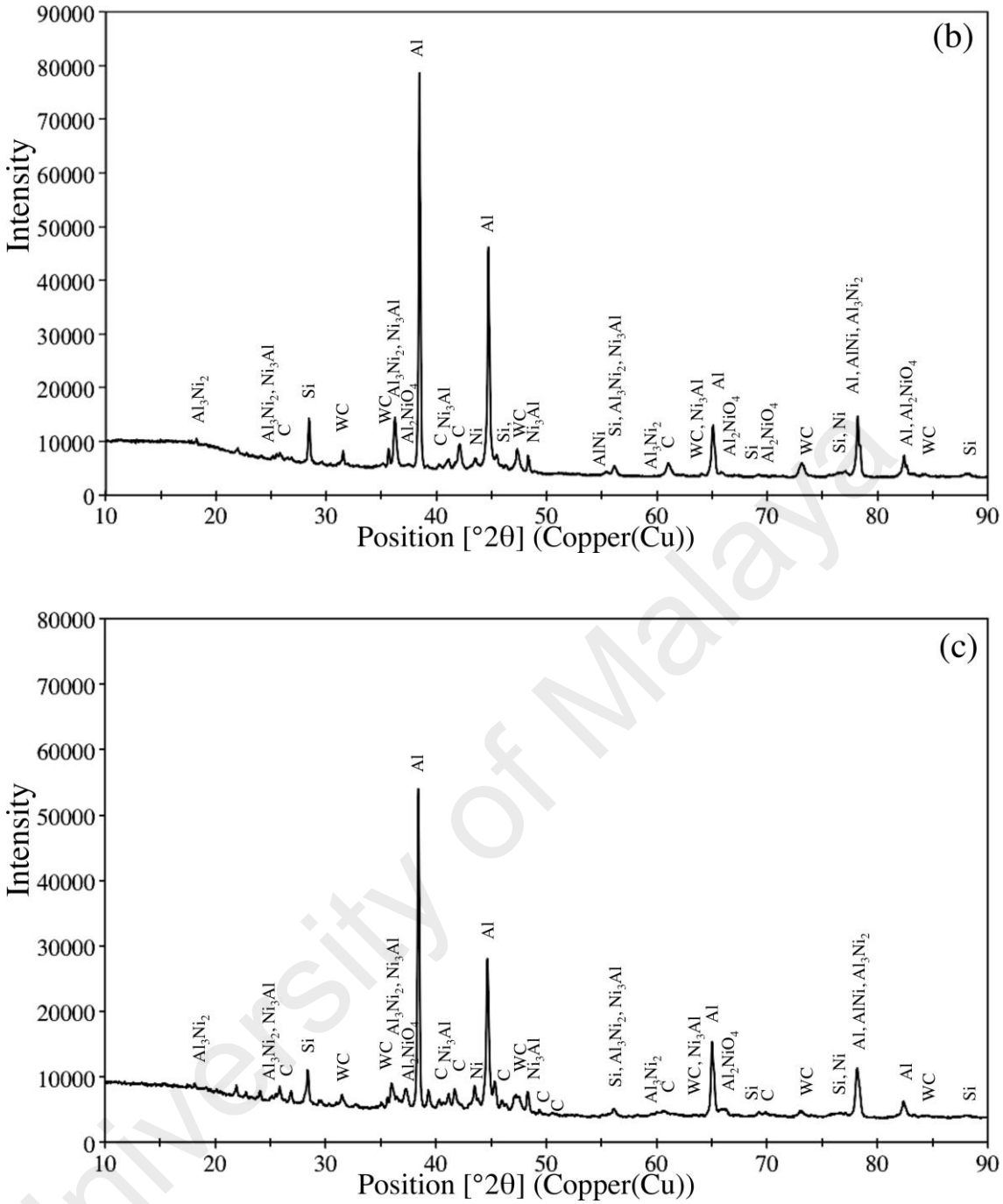

Figure 4.12: Continued

4.2.5 Phase identification of Ni-WC-TiO_2 coating

The X-ray diffraction pattern of Ni-WC-graphite composite coating with varying concentration of TiO_2 content is shown in Figure 4.13. The coating is composed of WC phase embedded in the Al-Ni intermetallic phase. The intermetallic phase was formed

based on the concentration of the nickel in the coating comprising of AlNIi, Al_3Ni, Al_3Ni_2, Ni_3Al. It is observed that characteristics reflection of the TiO_2 phase is also present which does not significantly increases in intensities as TiO_2 content is raised as depicted in Figure 4.13(a), (b) and (c). This may be due to partial evaporation of TiO_2 when laser impacts the powder and the heat generated is consumed in vaporizing or in the dissociation of TiO_2. Some of the reflections comprise of double peaks or peaks with shoulders wherein multiple compounds are formed are the same is presented in the Figure 4.13.

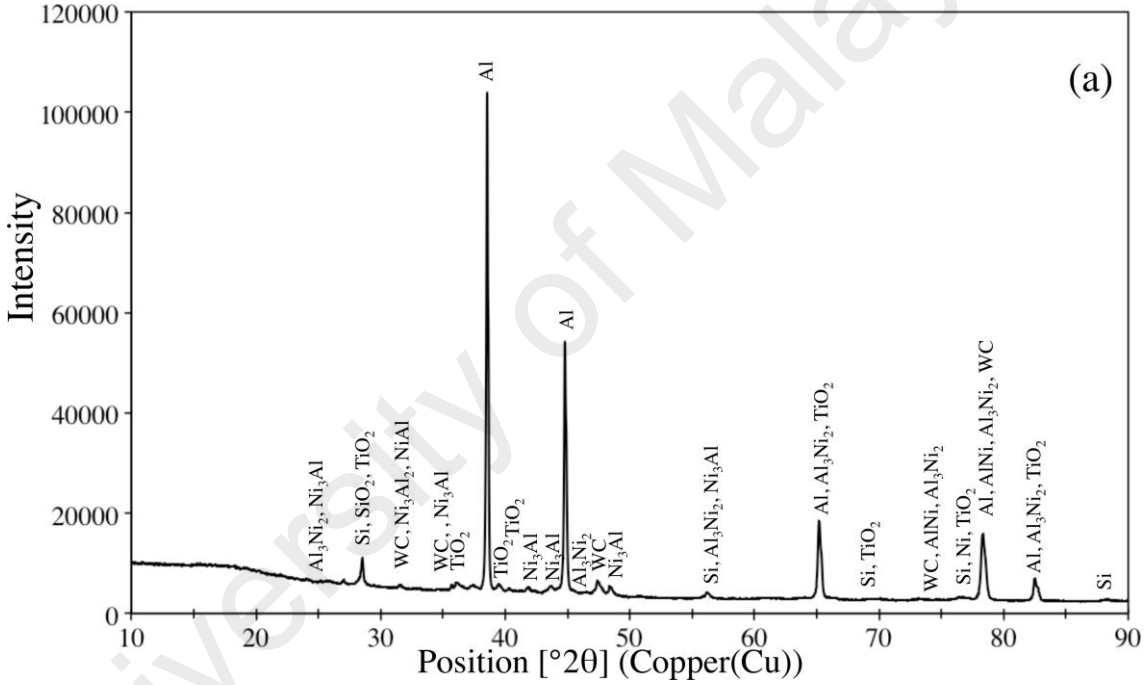

Figure 4.13: The X-ray diffraction spectrum for Ni-WC coating with TiO_2 content (a) 5 wt. % (b) 10 wt. % and (c) 15 wt. %

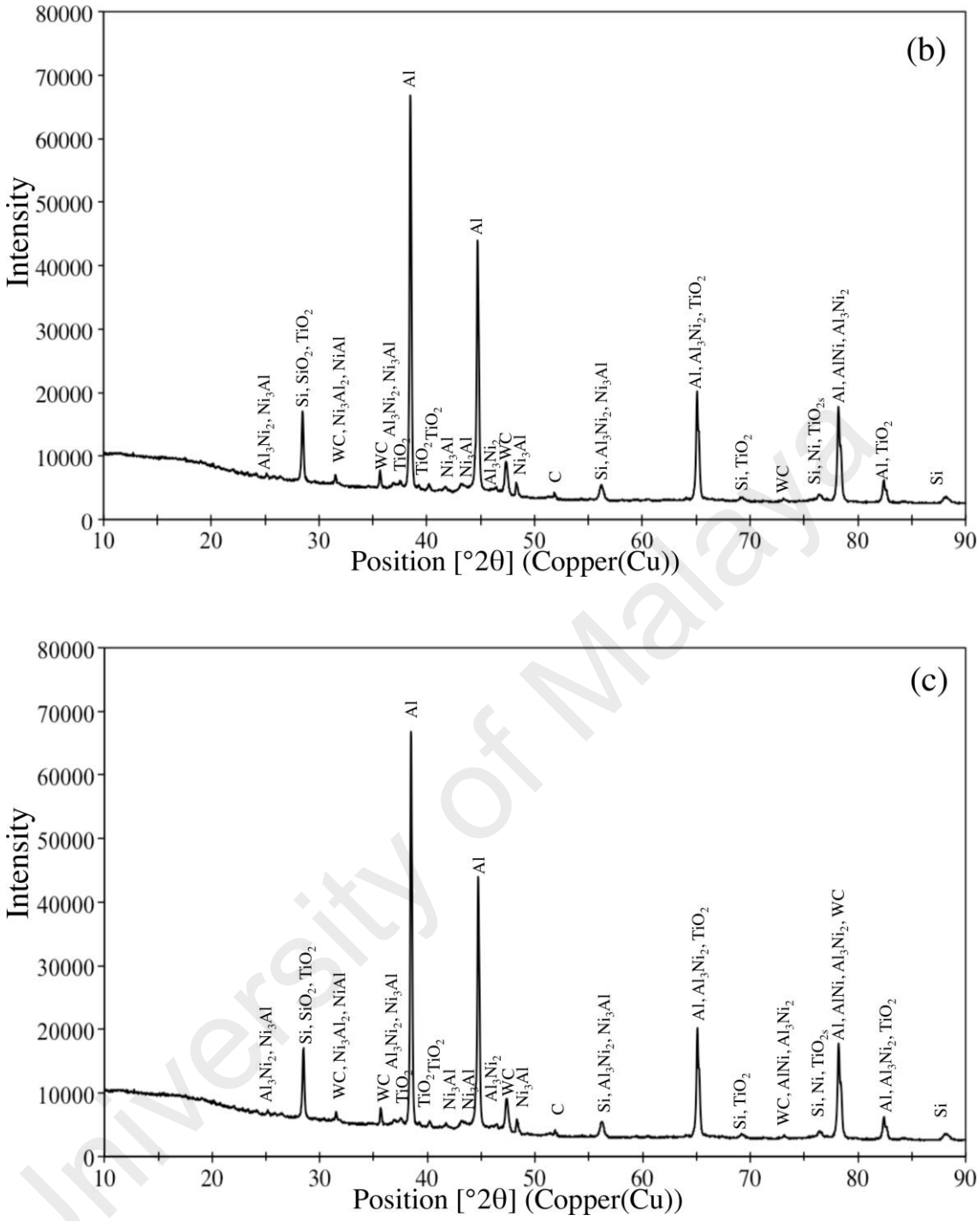

Figure 4.13: Continued

4.3 Hardness of MMC and HMMC coatings

The hardness as measured on the cross-sections of the 200 μm thick MMC and HMMC coatings are provided in Figure 4.14. The profile starts from substrate hardness and then as the concentration of nickel increases, enters in the eutectic zones. The hardness of

graphite based coatings decreases as the concentration increases with a maximum hardness for Ni-WC-5 wt. % graphite at 781 H_v. Similarly, the hardness for TiO_2 based coatings decreases as the concentration increases with a maximum hardness for Ni-WC-5 wt. % TiO_2 at 825 H_v. This trend and range of hardness were also observed by other researchers (Chao & Liang, 2004) wherein it was reported that the addition of TiO_2 causes an increase in ductile phase eutectics and thus leads for less harder coating.

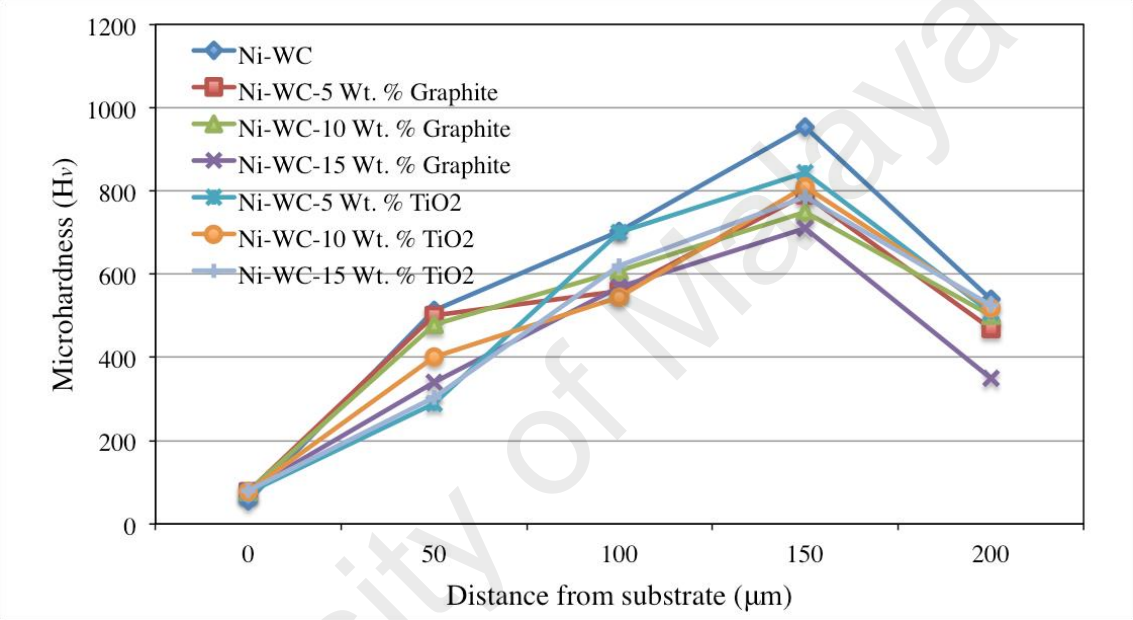

Figure 4.14: The surface hardness profiles for Ni-WC coating with graphite and TiO_2 content

4.4 Tribological properties of MMC coating

There are various applications that have been highlighted for Ni-WC based MMC laser cladding (Verwimp et al., 2011) such as cutting tools, plunger rods and in pressing tools signifying that Ni-WC based coatings improved wear resistance to around 3 times to that of the substrates utilized. It would be wise to note that the addition of solid lubricant to form hybrid metal matrix composite may further upscale their applications. In the following sections, an analysis for wear and friction coefficients has been made.

4.4.1 Wear and friction coefficient of AA5083 and Ni-WC coating

After the optimization of samples, the samples with highest surface hardness were evaluated for tribological testing so as to gauge the performance of coated samples with that of base alloy. The kinetic friction coefficient "μk" versus sliding distance for AA5083 and Ni-WC coating under normal loads of 10, 20, 30 and 40 N is displayed in Figure 4.15(a) and (b) respectively. Friction coefficient for AA5083 irrespective of the applied load did not attain a steady state and continued to rise towards the end of the experiment with greater fluctuations. These fluctuations were also present in the plots for the case of Ni-WC coating at higher applied loads of 30 N and 40N. The friction coefficient plots are indicative of ploughing induced adhesive wear arising due to building up of material. The small pieces of materials pulled out from the coating and were adhered to the counter-body steel balls. The material therefore ploughed off more coating material that will result in an increase in friction coefficient and wear. The deeper grooves are formed onto the counter-body where signs of material detachment are present due to severe adhesion. In one study similar phenomenon of fluctuations in friction coefficient plots for hard MMC SiC based friction stir processed AA5083 alloys was observed (Soleymani et al., 2012). It was reported that the addiction of harder carbide phase resulted in increase in friction coefficient as the carbide particles contributed to the damage of the counter-body surface. This resulted in the crushing of the carbide phase as well that was pulled out of the matrix thus acting as a loose abrasives (Basavarajappa et al., 2006) thus leading to increase in friction coefficient.

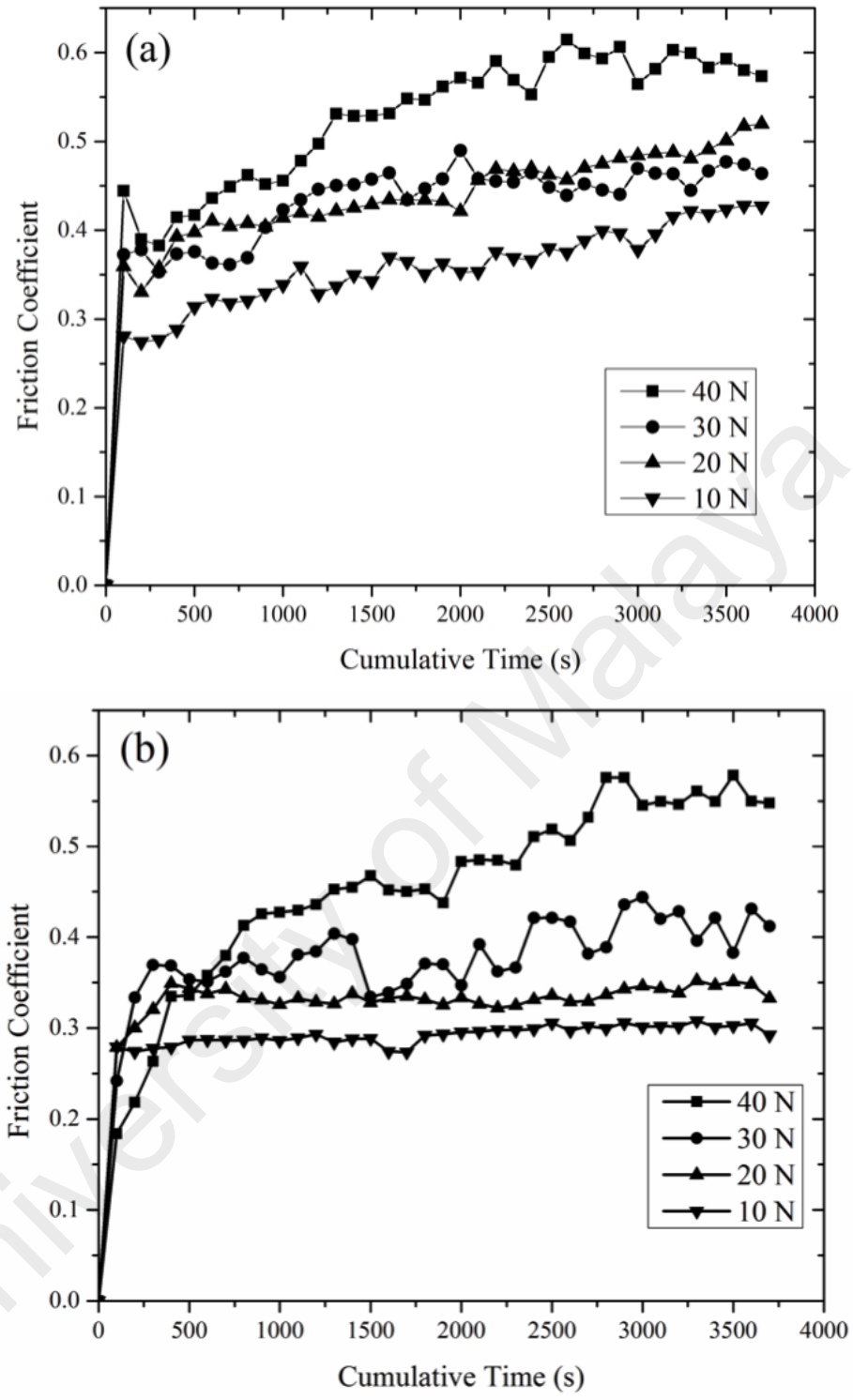

Figure 4.15: The friction coefficient of (a) AA5083 and (b) Ni-WC coating as a function of cumulative time for 10, 20, 30 and 40 N load

There was a slight difference in average friction coefficient values for AA5083. This indicates that aluminium has undergone similar wear mode for the range of normal load applied. A notable feature observed in the initial plots for AA5083 is higher friction

coefficient values which are attributed to running-in wear, characterized by the conformity of worn surfaces and initial successive wear of surfaces' micro asperities. Therefore, in the early stages of wear the damage is caused by micro-fractured brittle fragments within surface grains, removal of the oxide layer and changes in chemical composition. Thereafter, higher and stable friction in the later stages is conceded by tribochemical reactions that drastically contributes to the total amount of wear ensued (Stachowiak, 2006).

The running in wear process is acceptable wear regime experienced by components in the earlier operating stages of their lifetimes. In the case of Ni-WC coating, at lower applied loads, the friction coefficient "μk" has reached steady-state condition after a transition period of 100-200 seconds. Higher friction coefficients values at higher loads for Ni-WC coating is indicative that there was a change in the wear mechanism as the hard carbide particulates ejected from the softer aluminium matrix may have acted as harder abrasive asperities and may have played their role in increasing friction.

The variation of the steady-state friction coefficient as a function of increasingly applied loads is depicted in Figure 4.16(a). For the case of both substrate and coating, an increase in friction coefficient with respect to the normal load is observed. Furthermore, the mean values of friction coefficient "μk" for AA5083 by the change in normal loads was found to be higher (0.46) than coated metal (0.35). The lower average friction coefficient of the coating can be attributed to the microstructural and grain refinement as smaller grain and particle size exhibits lower friction coefficient values in contrast to the base alloy containing similar volume fraction and composition of alloying elements (Nath et al., 2012). For the case of 40N, AA5083 exhibited a friction coefficient value of 0.53. This is typical of the values of coefficient of friction in dry sliding wear of AA5083 against harder steel counterpart.

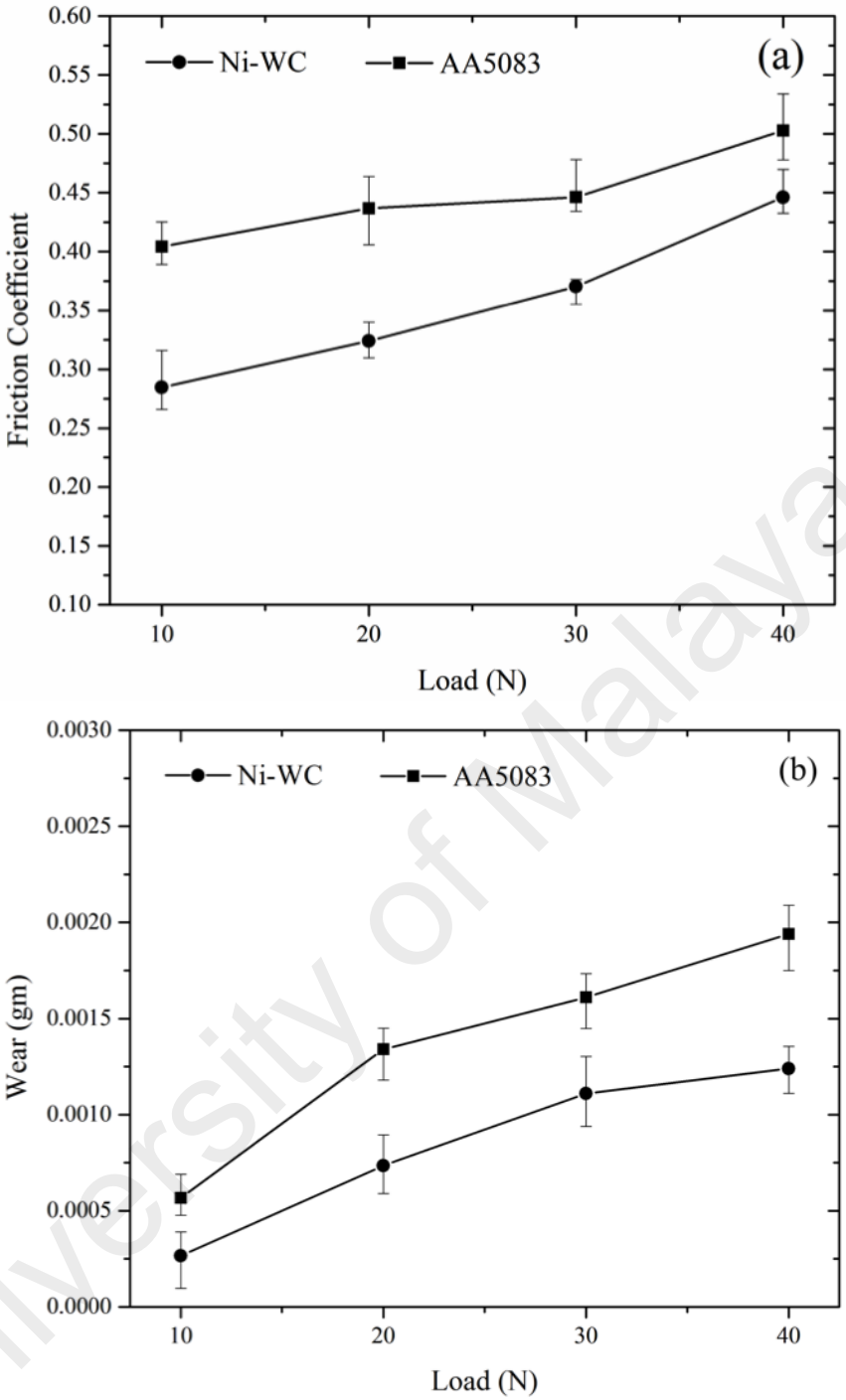

Figure 4.16: (a) Steady state friction coefficient of AA5083 and Ni-WC coating under various applied loads, (b) Wear response of AA5083 and laser treated Ni-WC coating.

Similar friction coefficient values between 0.5 to 0.6 were also reported for AA5083 against counter-body of AISI D3 steel with an applied load of a normal load of 5 Kgf/mm. (Soleymani et al., 2012) In another study, considerable fluctuation in sliding

curves was attributed to substrate lower hardness and friction coefficient values in the range of 0.55 to 0.65 were recorded (F. Y. Zhang & Yan, 2014). The friction coefficient of harder nickel tungsten carbide reinforced matrix remained higher for higher loads, which can be attributed to the bond strength between the carbide phase and softer aluminium matrix. When softer aluminium matrix wears out, the harder asperities damage the surface of the counter-body giving rise to an increase in surface roughness of mating part.

The formation of grooves in the counter-body further results in the destruction and removal of reinforced particulates. At higher loads, the sliding curves show visible vibrations and loud whistles which are a sign of possible harder asperities pullout (D.-X. Peng & Kang, 2014). Thereafter, these damaged particles present between the surfaces increase friction by operating as loose particles. The relation of wear and friction is further corroborated in Figure 4.16(b) showing variation in coating wear with increasing loads. For nearly all surfaces tested, the wear resistance of the treated samples was considerably better than that of the untreated. The wear of coating was considered to be almost 2.5 times lower than the bulk material samples for the case of lower applied loads but coating remained prone to a higher amount of wear at 30 and 40 N loads. The lower friction coefficient exhibited at lighter loads is attributed to a lesser transfer of shear stresses to the composite layer under tribochemical contact resulting in lower wear rates (gm).

4.4.2 Characterization of worn surface and debris

In order to investigate the tribological properties and wear mechanism that ensued the coating and substrate wear scars, surface morphology by SEM and EDS elemental analysis was performed on wear scars.

Figure 4.17 shows the SEM images along with spot scanning EDS spectrum of wear tracks for AA5083 and Ni-WC coating at 20 N applied loads. Under similar applied tribological conditions, the substrate and laser coated samples exhibited contrasting wear modes and based on worn grooves dimensions various inferences can be made. In the case of AA5083, the microstructure at higher magnification shows severe plastic deformation in terms of deeper and wider grooves and the presence of worn out debris. Earlier studies conducted found similar features in worn scar morphology (Nath et al., 2012). The harder asperities formed on stainless steel counter-body shifted the material to the side of the grooves. These wider grooves (150 μm) were formed due to smearing and ploughing action, which are characteristics of severe plastic deformation. Due to reciprocating cyclic load applied, fatigue cracks were generated during the wear process, and delamination started which indicates the initiation of debris formation in the transfer layer. The plate-like delaminated aluminium debris generated and iron transferred debris further assisted in greater material removal as presented Figure 4.18(a). Under severe wear regime in case of AA5083, debris generated was in the form of larger plate-like fragments (5 – 40 μm) in addition to smaller equiaxed particles (0.5 - 10 μm). Sheets like debris are a sign of delamination wear mechanism which has also been also reported (L. Peng, 2013; Soleymani et al., 2012). This is also confirmed in scar morphology of counter-body where the sheared aluminium material is transferred and adhered onto the scar surface as observed in OM image Figure 4.18(c). The presence of O and traces of Fe in EDS spectrum at point E (Figure 4.17(c)) shows the presence of oxidized material transferred from counter-body further deteriorating the wear of AA5083. At the beginning of wear tests, small pieces of material were pulled off and adhered to the counter-body. Thereafter, subsequently rubbing action oxidizes the adhered material that correlates with the EDS analysis. Therefore, it can be clearly illustrated that severe adhesive wear characterized the wear mechanism for AA5083. A

similar explanation was given by Panagopoulos and Georgiou (Panagopoulos & Georgiou, 2007) for severe wear of AA5083. It was pointed out that sliding wear mechanism of AA5083 against stainless steel, revealed an intense delamination and adhesive wear.

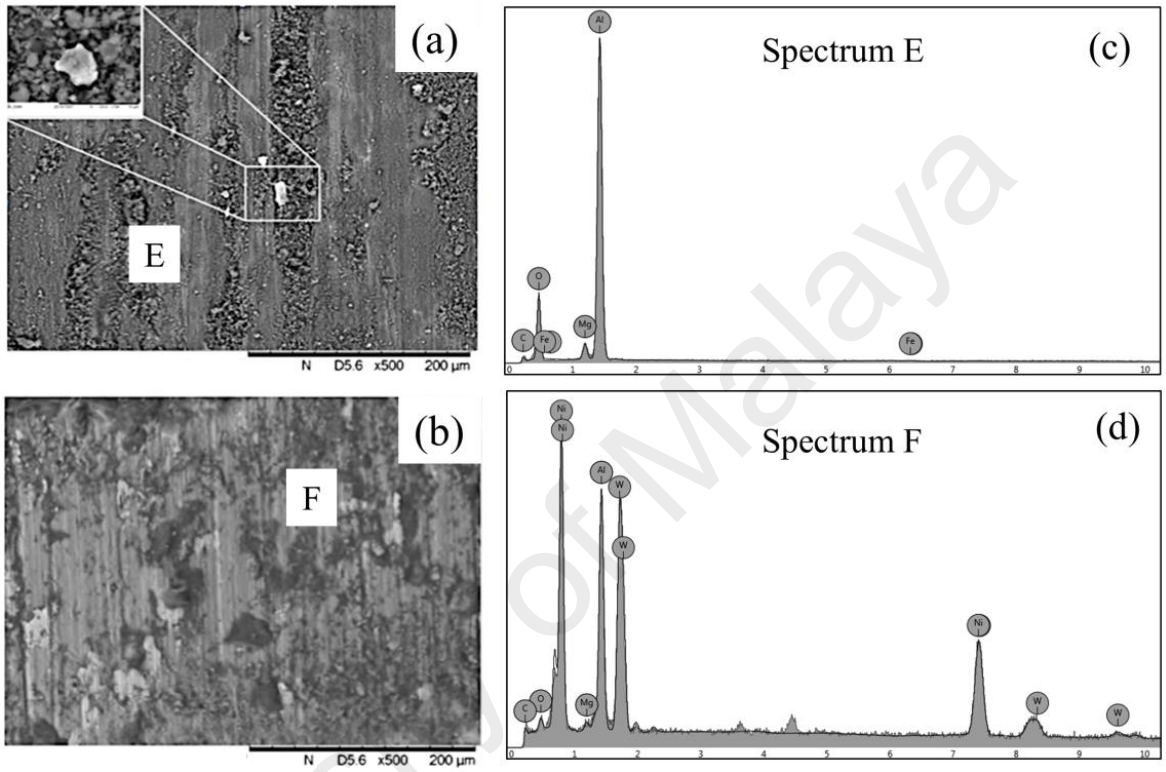

Figure 4.17: Scanning electron micrograph of worn surfaces for (a) AA5083 and (b) Ni-WC coating along with their EDS spectra of (c) area E and (d) area F

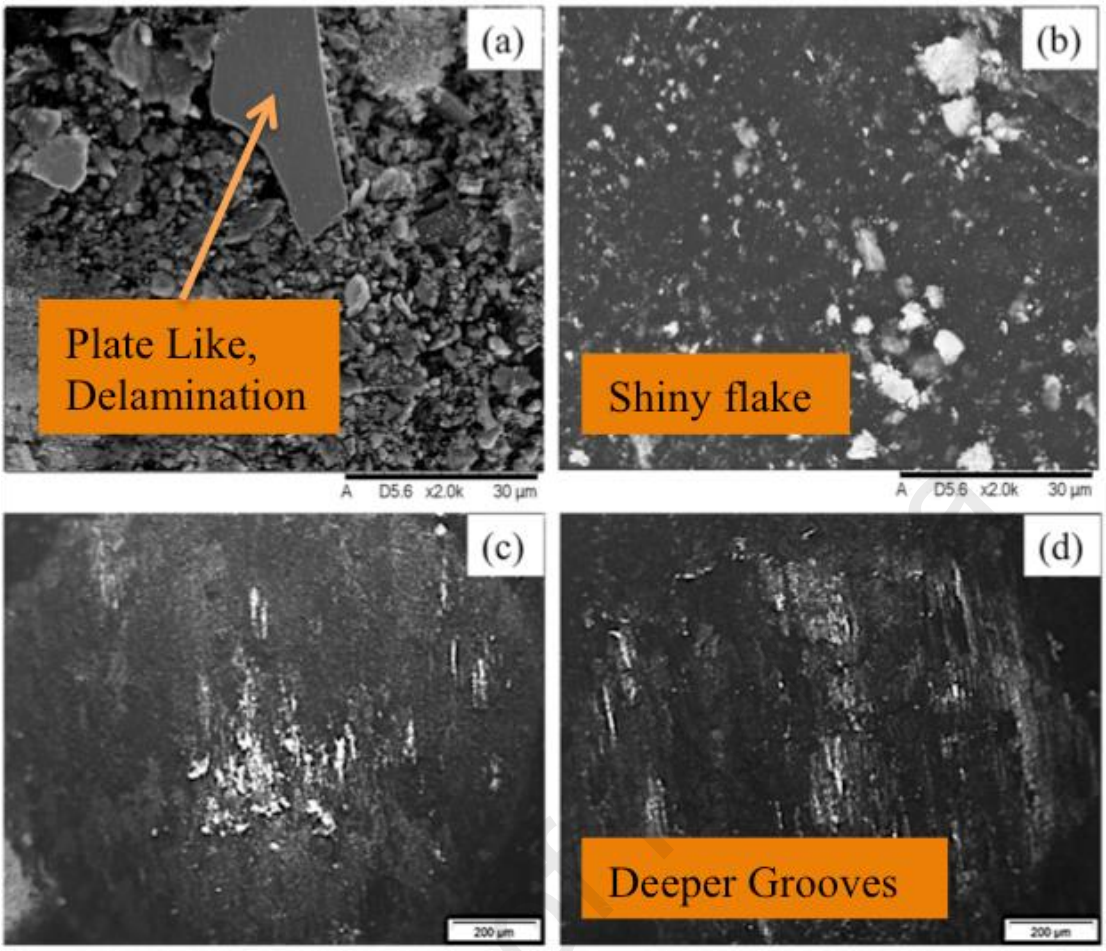

Figure 4.18: SEM images of debris for (a) AA5083 and (b) Ni-WC coating along with optical micrograph of 440c steel counter-body for (c) AA5083 and (d) Ni-WC coating

With the softer aluminium surface now protected by strongly bonded hard coating, the wear of the protected material remains far lesser as long as the coating doesn't wear out as easily. In the case of the Ni-WC coating, the extent of wear is clearly visible to be lower than AA5083 (Figure 4.17 (b)). EDS spectra at spot F as presented in Figure 4.17(d) indicates that Al, Ni, W and C were the major elements present resisting adhesive contact with counter-body. As compared with AA5083, the lesser amount of oxidation signifies mild oxidative wear for Ni-WC coating. Ni and its intermetallic compounds in the coating act as a hard reinforcing phase in a ductile aluminium matrix, whereas the presence of WC resists abrasion. The composite surface specimen worn scar morphology remains approximately smoother with fewer and shallow grooves.

These results are supported by the amount of debris generated, which are far lesser and are smaller equiaxed particles (0.5 – 50 μm). The smaller particle-like debris generated was blackish indicating oxidative wear mechanism, whereas larger and white flake-like debris observed are severe ploughing of iron particles transferred from the counter-body. The delaminated flake-like debris removed from the counter-body is clearly visible as white debris, which can be observed in Figure 4.18(b). The generation of iron-rich debris is caused by the abrasion of the counter-body steel when hard particles are trapped between mating surfaces. This phenomenon is due to higher hardness of reinforced composite coating. Hence, the amount of white debris found is lesser in aluminium samples than in coated samples. The reduction in the amount of wear can be related to higher surface hardness. The higher hardness achieved as a result of the optimization is attributed to the presence of hard brittle nickel-aluminium based intermetallic compounds. Furthermore, the softer aluminium matrix present in the interdendritic region provided with higher toughness. Coated samples at lower applied loads showed lesser initial friction coefficient clearly indicating higher hardness suppressing the plastic deformation followed by steady-state friction coefficient, which is an indication of resistance to adhesive wear. Furthermore, as in the case of abrasive wear, harder counter-body ploughs through the softer material and thus the hardness of the softer materials continues to be of paramount importance for improving wear resistance. The aim of the Ni-WC coating was to suppress the large plastic deformation in the form of formation wider grooves on the surface. In several studies, the effects of WC-15Co-15NiCr alloy (Nath et al., 2012) and WC-2Ti-2Mg (Staia et al., 2000; Staia et al., 2001) have been investigated on laser alloyed Al substrate and were found to have improved wear resistance by suppressing plastic deformation. In Figure 4.18(d) there is a lesser indication of the presence of adhered or material build-up on the counter-body scar but Ni-WC coating has produced significant scratches and ploughs marks.

Furthermore, black patches of oxidation are noticeably visible. The counter-body itself shows abrasive wear with well-defined marks of higher plastic deformation. Thus, Ni-WC coating underwent moderate abrasive and oxidative wear mechanism. Hence, laser composite surfacing of hard Ni-WC composite coating on AA5083 has significantly lowered wear damage during dry sliding testing conditions.

4.4.3 Atomic force microscopy of worn scars

Wear testing on the samples lead to removal and changes in the surface texture AFM characterization as showed in Figure 4.19 reveal the topographical features of worn scar for coated and uncoated samples. Surface scan area was kept 30 µm by 30 µm and the data of surface roughness (R_a) which is described as the arithmetic mean of the height deviations from profile mean value was extracted. The AA5083 worn scar AFM image Figure 4.19(a) shows the presence of hills in the form of coarse grooves and ridges showing plastic deformation and intense ploughing of ductile aluminium alloy with an average roughness value of 1.70 µm. Roughness, as created by dry sliding wear testing on the coated sample was lower to around 1.28 µm, which is 24% lower than that of the uncoated sample. The coated sample exhibited small protruding dimples indicative of mild abrasive wear Figure 4.19 (b). The AFM observations also suggest to coating ability in reducing wear of AA5083-O alloy.

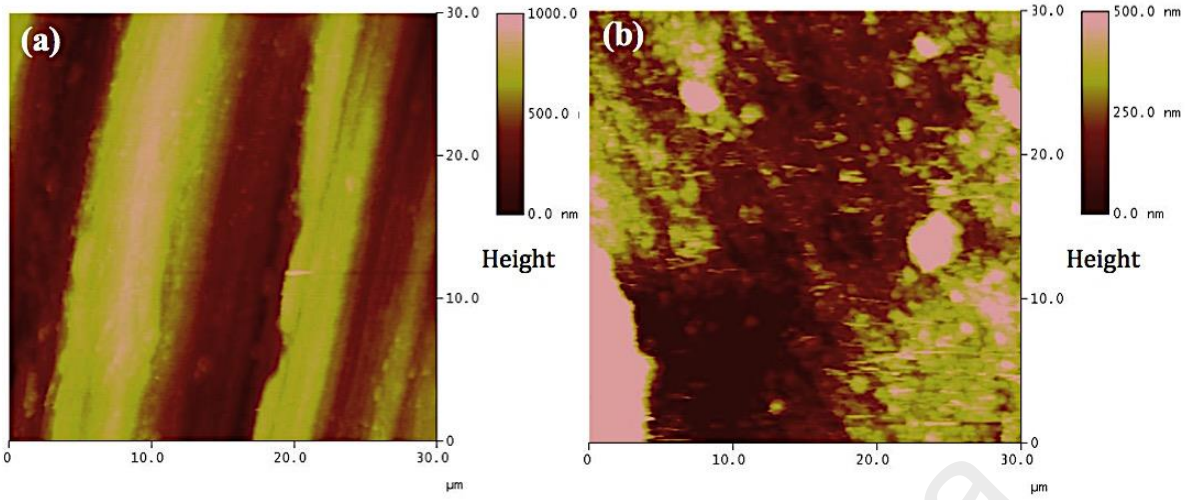

Figure 4.19: Atomic force microscopy (AFM) images of worn scar morphology of (a) AA5083; (b) Ni-WC coating

4.5 Tribological properties of HMMC coatings

After evaluating the tribological properties of AA5083 substrate and MMC Ni-WC coatings, an analysis of wear and friction characteristics of Al-17Si substrate and HMMC coatings was made which is presented below.

4.5.1 Wear and friction coefficient of Al-17Si substrate, Ni-WC-Graphite and Ni-WC-TiO_2 coating

For evaluating tribo-mechanical properties of coatings comprising of solid lubricant, applied load of 20 N was utilized with a frequency of 10 HZ for the duration of 1 hour (3600 sec). The kinetic friction coefficient "µk" versus sliding distance for Al-17%Si and Ni-WC coating with additives containing various concentrations is displayed in Figure 4.20. Friction coefficient for Al-17%Si did not attain a steady state condition and continued to rise towards the end of the experiment with greater fluctuations. These fluctuations were also present in the plots for the case of Ni-WC-5 wt. % graphite and 5 wt. % TiO_2 coating. A notable feature observed in the initial duration of all test is

higher friction coefficient values, which are attributed to running in wear, characterized by the conformity of worn surfaces and initial successive wear of surfaces' micro asperities. Therefore, in the early stages of wear, the damage is caused by micro-fractured brittle fragments within surface grains, removal of the oxide layer and changes in chemical composition. Thereafter, higher and stable friction in the later stages is conceded by tribochemical reactions that drastically contributes to the total amount of wear ensued. The running in wear process is acceptable wear regime experienced by components in the earlier operating stages of their lifetimes. Higher friction coefficients values at lower solid lubricant concentrations for Ni-WC coating is indicative that the amount of additives added was not enough for the formation of transfer layer that would have contributed to reducing friction. Albeit, with increasing concentration of additives a significant improvement in reduction of friction coefficient, is observed indicating that they were effective in reducing wear.

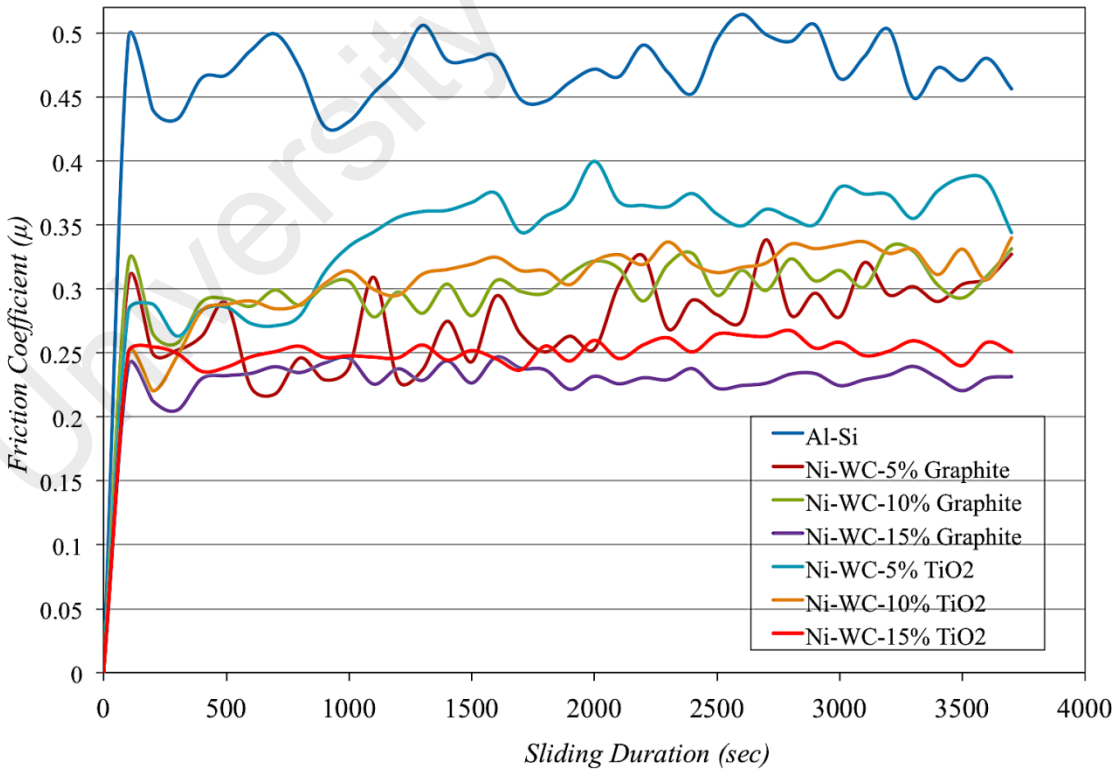

Figure 4.20: The friction coefficient of Al-17%Si and coatings with graphite and TiO_2 additives

The variation of the steady-state friction coefficient as a function of increasing additives concentrations is depicted in Figure 4.21(a). For the case of both additives a decrease in friction coefficient with respect to the normal load is observed. Furthermore, the mean values of friction coefficient "μk" for Al-17Si was found to be 0.47, 0.29 for Ni-WC-5 wt. % graphite, 0.30 for Ni-WC 10 wt. % graphite, 0.21 for Ni-WC 15 wt. % graphite, 0.35 for Ni-WC 5 wt. % TiO_2, 0.29 for Ni-WC 10 wt. % TiO_2 and 0.24 for Ni-WC 15 wt. % TiO_2 were observed. The lower average friction coefficient of the coating can be attributed to the microstructural and grain refinement as smaller grain and particle size exhibits lower friction coefficient values in contrast to the base alloy containing similar volume fraction and composition of alloying elements (Nath et al., 2012). For the case of Al-17Si alloy, it exhibited a friction coefficient value of 0.47, which has been observed for dry sliding friction of aluminium silicon alloys (Bidmeshki et al.; Dwivedi, 2006; Ramesh & Prasad, 2008). This is typical of the values of coefficient of friction in dry sliding wear of Al-Si against harder steel counterpart (Dwivedi, 2006). Higher friction coefficient for dry sliding of Al-Si alloys has been attributed to the impact of specific sliding condition on high friction being generated. At lower sliding speeds the greater amount of duration is available for the growth and evolution of asperity contact regions. This increases the amount of frictional force required to shear away these asperity contacts so as to maintain the contact relative motion (Dwivedi, 2006). For graphite based coatings, greater than 15 wt. % has shown friction coefficient in the range between 0.2 to 0.25 in Al-17Si is reported (Ye, 2003). For graphite based MMC coatings a friction coefficient in the range of 0.21-0.22 has also been observed (Scharf & Prasad, 2013). Under sol-gel coating of Ni-TiO_2, a friction coefficient of 0.37 has been reported under a load of 3N, sliding speed of 2 $mmin^{-1}$ and a contact radius of 6mm (YX Wang et al., 2014). In another work, the addition of 6.5 and 8.3 wt. % TiO_2 in Ni showed a friction coefficient

range in between 0.3-0.35.

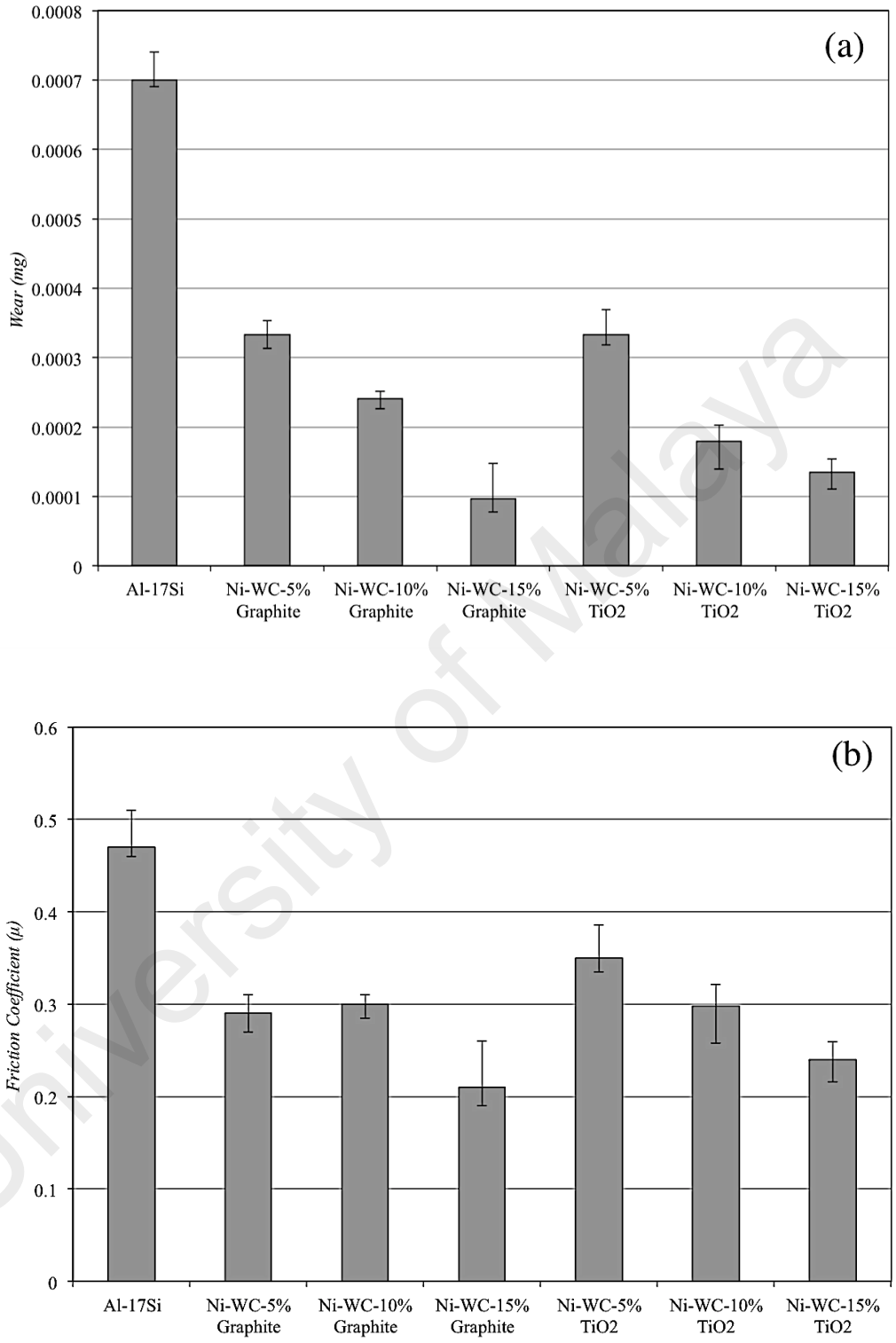

Figure 4.21: (a) Wear response of Al-17Si and laser treated Ni-WC coating with additives (b) Steady state friction coefficient of Al-17Si and laser treated Ni-WC coating with additives

The relation of wear and friction is further corroborated in Figure 4.21(b) showing substrate wear and variation in coating wear with the change in additive type and concentration. For nearly all surfaces tested, the wear resistance of the treated samples was considerably better than that of the untreated. The wear of coating, comprising of 15 wt. % graphite as an additive was considered to be almost 7.2 times lower than the bulk material samples under dry sliding conditions.

Similarly, the wear of 15 wt. % TiO_2 based coating was almost 5.1 times lesser than the substrate wear. It can be remarked that as does the concentration of shear-able graphite and TiO_2 phase in the coating increases, so does the friction coefficient and wear rates. Therefore, the composite coatings containing various particulates have been reported to have shown far lesser wear rates than that of the base alloy as per previous studies (Roy et al., 1992). Metal matrix composites have been significantly used in automotive, aerospace and industrial components registering low friction coefficient (Savan et al., 2000). In one study it was found that the wear rate was correlated with the concentration of graphite in the plasma sprayed metal matrix composite coating at a maximum of 8 wt. % graphite (Natarajan et al., 2016). Some researchers have also pointed out that with increasing concentration of TiO_2 in electrodeposited Ni coating, improves hardness and wear resistance (Baghery et al., 2010).

4.5.2 Wear characteristics of substrate Al-17Si alloy

In this section, the wear characteristics of substrate Al-17Si shall be made based on inferences of worn scar surfaces, the counter-body damage and the size and amount of debris generated.

4.5.2.1 Characterization of worn surfaces

The wear of the Al-17%Si hypereutectic piston alloy at 20N applied normal load is showed in Figure 4.22. Figure 4.22(b) and (c) shows that the wear of Al-Si alloy was characterized by the considerable generation of wear debris in the form worn particles. These particles that were formed on the wear scar were found to be higher in the content of oxygen as presented in Figure 4.22(d) and further contained a certain amount of iron, silicon, nickel and aluminium. As illustrated in Figure 4.22(b) abrasion in the form of grooves and scratches are visible which are translated into transverse cracks as wear progress. These cracks then progress to result in rapid material removal in the form of the plate-like debris. Earlier studies conducted found similar features in worn scar morphology (Sarkar, 1975). The harder asperities formed on stainless steel counter-body shifted the material to the side of the grooves. These grooves (30-40 μm) were formed due to smearing and ploughing action, which are characteristics of severe plastic deformation. Due to reciprocating cyclic load applied, fatigue cracks were generated during the wear process, and delamination started which indicates the initiation of debris formation in the transfer layer. The cracks that are propagated connect with each other and the fragmented metallic particles are further fragmented to form mechanically mixed oxide particles in the contact zone. During wear when tribo film is generated, is further weakened when the stresses derived on the sliding surface which leads to fracture of oxide film generated as oxidized debris.

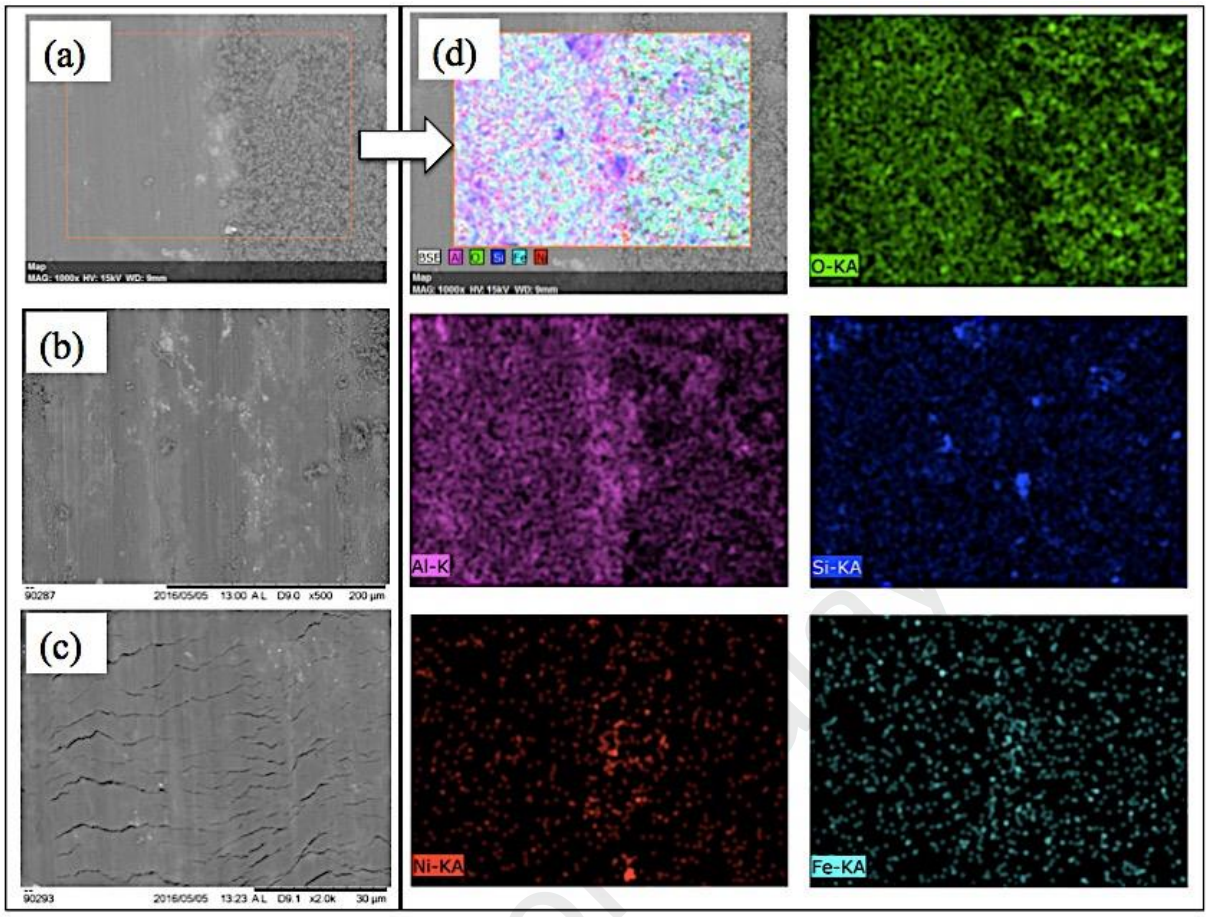

Figure 4.22: Scanning electron micrograph of worn surfaces for Al-Si alloy (a) Debris-scar interface, (b) and (c) at 0.5K and 1.0K magnification along with corresponding (d) EDX elemental mapping of O, Al, Si, Ni and Fe elements

4.5.2.2 Counter-body wear and debris analysis

Figure 4.23 shows the SEM images of debris and their EDS area mapping along with OM of counter-face. Figure 4.23(e) and (f) shows the presence of oxidized material transferred from counter-body further deteriorating the wear of Al-Si alloy. At the beginning of wear tests, small pieces of material were pulled off and adhered to the counter-body. Thereafter, subsequently rubbing action oxidizes the adhered material that correlates with the EDS analysis. These oxidized elements might be trapped between the sliding surfaces and get crushed or compacted due to the repetitive sliding Therefore, it can be clearly illustrated that severe abrasive wear with fatigue cracks

characterized the wear mechanism for Al-Si alloy. A similar explanation was given for severe wear of Al-Si alloys (Staia et al., 2001). It was pointed out that sliding wear mechanism of Al-Si alloy against stainless steel, revealed an intense delamination and abrasive and slight adhesive wear.

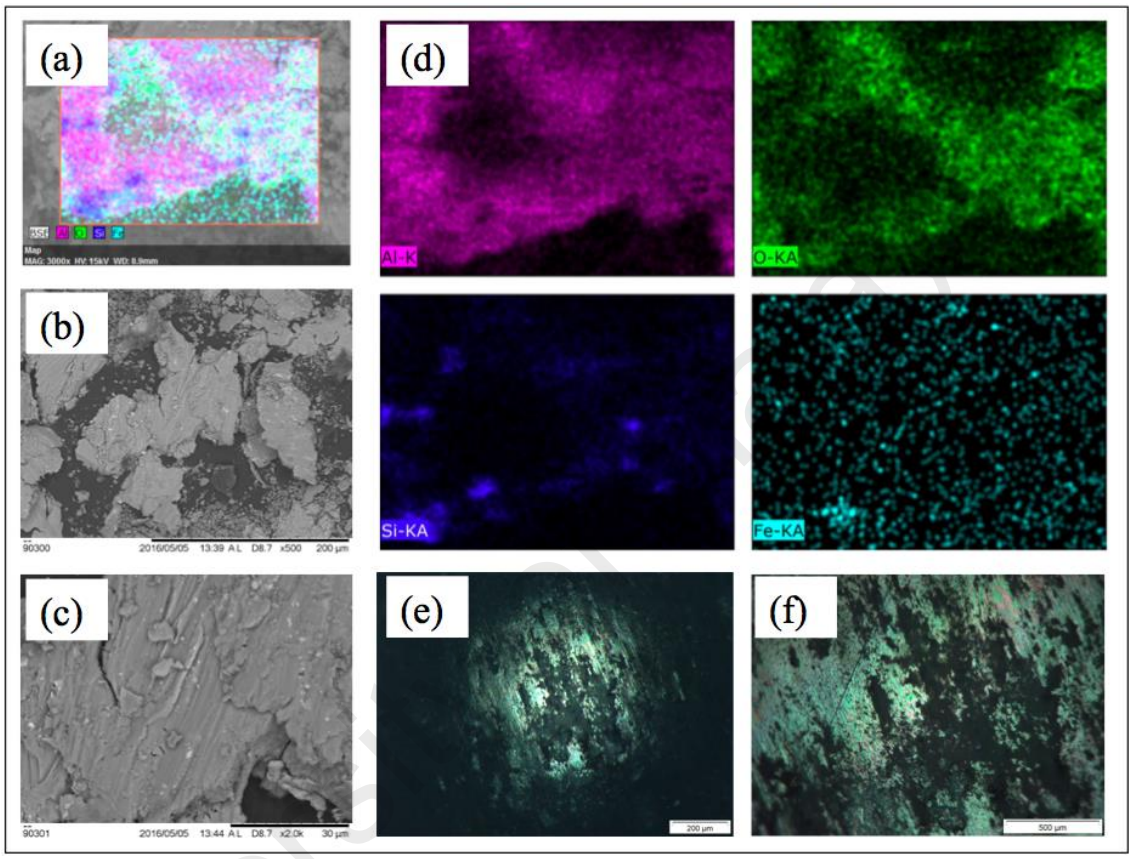

Figure 4.23: (a) EDX mapping of images for debris of Al-17%Si debris elemental mapping, (b) and (c) SEM image of debris at 0.5k and 2.0k magnification, (d) EDX elemental mapping of Al, O, Si and Fe and Fe element debris, (e) and (f) optical micrograph of counter body scar at distinctive magnifications

The plate-like de-laminated aluminium debris generated and the iron transferred debris further assisted in greater material removal as presented Figure 4.23(b) and (c). The oxide particles were generated as presented in the EDX of the wear debris (Figure 4.23(a) and (d)). The microstructure at higher magnification shows severe plastic deformation in terms of deeper and wider grooves that are also present on the worn out debris. Under severe wear regime in the case of Al-S alloy, debris generated was in the

form of larger plate-like fragments (100 - 200 μm) in addition to smaller equiaxed particles (0.5 - 20 μm). Sheets like debris are a sign of delamination wear mechanism which has also been also reported (L. Peng, 2013; Soleymani et al., 2012). This is also confirmed in scar morphology of counter-body where the sheared oxidized material is transferred and adhered onto the scar surface as observed in OM image Figure 4.23 (e) and (f).

4.5.3 Wear characteristics of Ni-WC-Graphite coating

In this section, the wear performance of Ni-WC-Graphite based HMMC coatings shall be made based on inferences of worn scar surfaces, the counter-body damage and the size and amount of debris generated.

4.5.3.1 Characterization of worn surface

The worn surface morphology and EDX area mapping of the element carbon for the Ni-WC-graphite coating deposited on hypereutectic piston alloy under a tribological normal applied load of 20N are shown in Figure 4.24. Figure 4.24(a) and (b) shows that the wear of Ni-WC-5 wt. % graphite was portrayed by the generation of the wear scar in the form of worn groove and light scratches. As illustrated in Figure 4.22(b) abrasion in the form of grooves and scratches are visible with are translated into parallel cracks to the sliding direction being produced as the wear progresses. These fatigue cracks then progress to result in material removal, in the form of adhered or compacted debris removal. Earlier studies conducted found similar features in worn scar morphology. These lighter grooves (30-40 μm) were formed due to slight smearing action. Due to reciprocating cyclic load applied, fatigue cracks may have generated during the wear process.

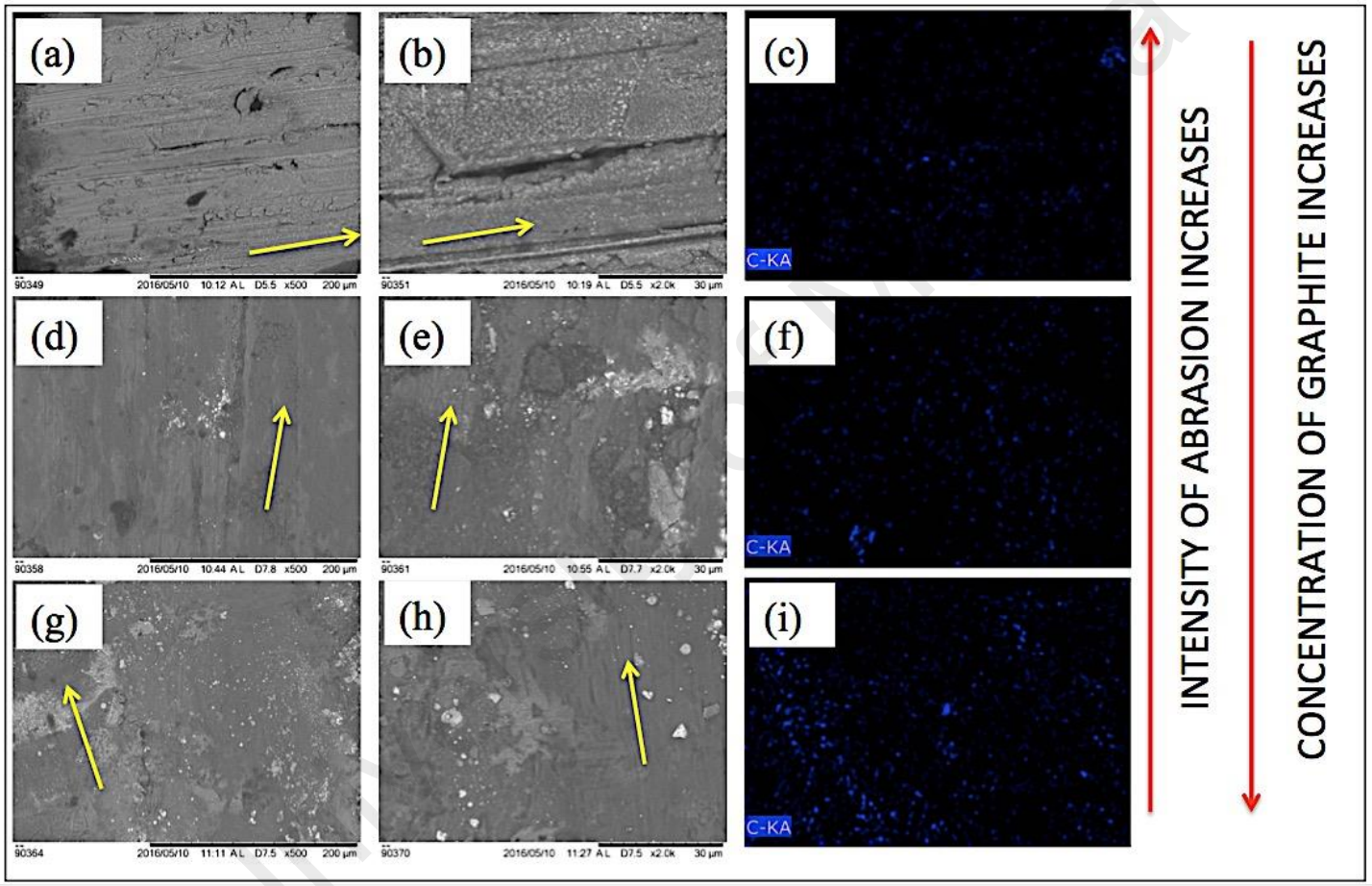

Figure 4.24: SEM image of coating wear with their magnified views for (a), (b) 5 wt. % graphite (d), (e) 10 wt. % graphite, (g), (h) 15 wt. % graphite, along with their corresponding EDX carbon element mapping in (c), (f) and (i).

However, at high frequency and temperature micro cracks may have initiated which propagated due to the involvement of fatigue induced wear. The EDS area mapping showing the amount of graphite concentration increasing respectively in Figure 4.24(a), (b) and (c) shows that the severity of the corresponding wear scars on the coating has reduced considerably.

Figure 4.25 shows the EDS spot scan on worn scar morphology for Ni-WC-Graphite coatings with a change in graphite content. It can be seen that the amount of carbon detected grows strongly as with concentration and so does the oxidation in the form of oxide formation. The intensity and formation are abrasives are reduced as the addition of graphite assists in the formation of an effective transfer layer that may shear itself away in the form of oxidized mixtures of various coatings and counter-face materials that are ejected during wear in the form of wear debris. These softer phases negate the cutting effect of carbide phase and hence assist in the reduction of material loss. The wear mechanism for higher concentrations of graphite seems to be more tending towards slight abrasive and more of an oxidative. It was found in one study (Natarajan et al., 2016) that the addition of graphite improves abrasion resistance and was indicated that the right amount of graphite can impart a sufficient amount of lubricating effect during service lifetimes of the components.

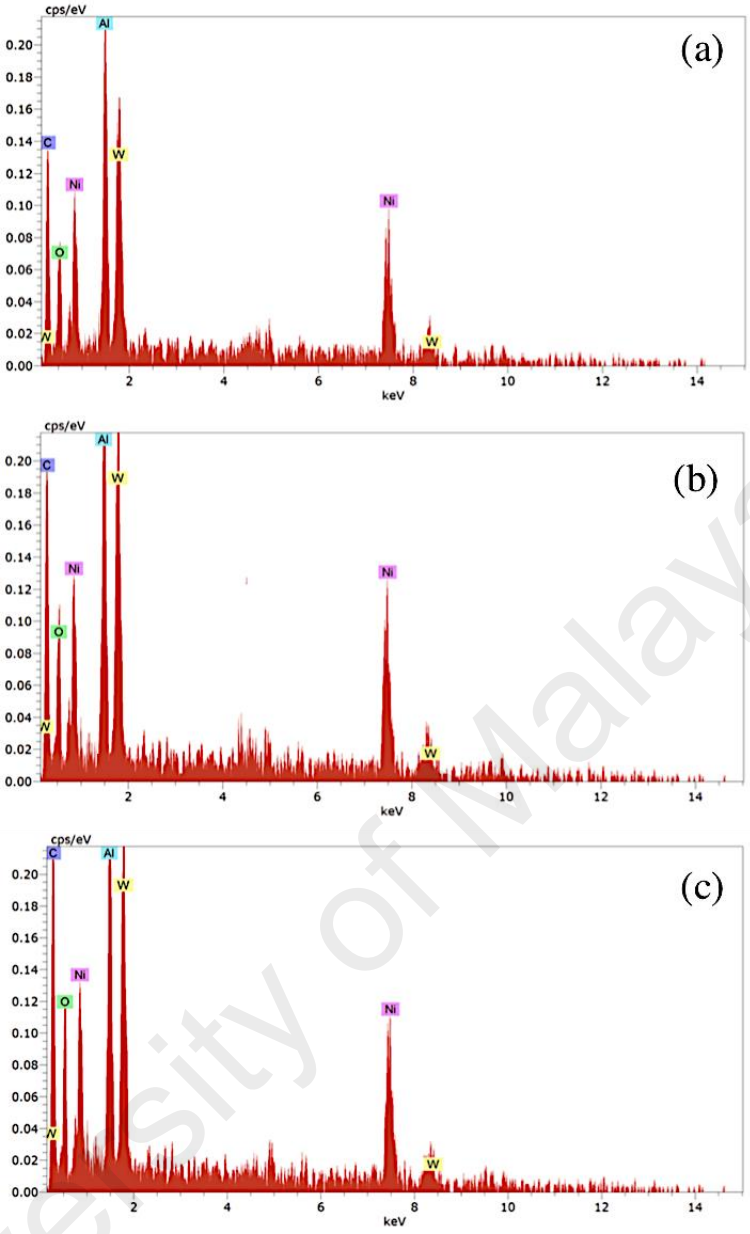

Figure 4.25: EDS spot scanning spectrums on worn scars of (a) Ni-WC-5 wt. % Graphite, (b) Ni-WC-10 wt. % Graphite and (c) Ni-WC-15 wt. % Graphite

4.5.3.2 Counter-body wear and debris analysis

The wear mechanism of the worn surfaces is highly correlated with the wear mechanism identified on the surface of the counter-body. Hence, it is quite important to look into the details of the worn surface morphology, material deposits, shearing, tribo film formation, abrasion, or the structure of the scar. From the Figure 4.26, it is quite evident

that with respect to the change in concentration of the graphite additive, significant changes in the wear mechanism of the counter-bodies are observed. This is an evidence of how closely the concentration of graphite can impact and alter the wearing phenomenon that took place during dry sliding.

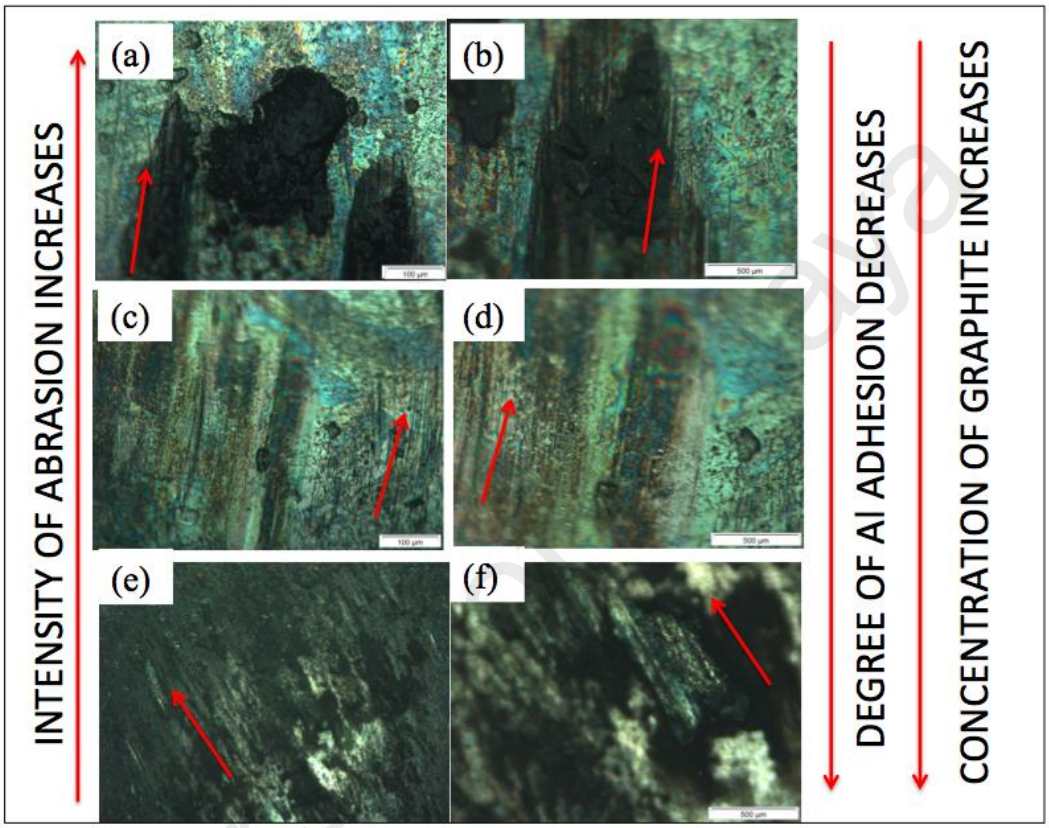

Figure 4.26: Optical micrographic images of counter-body worn tracks at lower and higher magnification for (a), (b) 5 wt. % graphite (c), (d) 10 wt. % graphite, (e), (f) 15 wt. % graphite

These are the characteristics of adhesion in addition to galling wear for 5 wt. % graphite coating, wherein the materials adhere from the contacting surface at higher hertizian contact pressure. The ball on plate induces extreme amounts of hertizian contact pressures, thus, the material galls and the galled material thereafter is grooved with the asperities that are formed at a micro level. After adhesion due to higher friction, slipping and tearing of the crystal structure follow the galling. From Figure 4.26(a), the galling

phenomena were observed for the counter-body of Ni-WC-5 wt. % graphite coating. There are highly adhered blackish deposits, which are somewhat shiny and seems melted or welded onto the hardened bearing steel. Even though the balls were cleaned and degreased with acetone in the ultrasonic cleaner for 30 minutes, these deposits remained and hence were neither in any form of debris attached nor loosely adhered coating or aluminium metal. No significant damage by abrasion is observed on this counter-body. Due to adhesion of coating onto the counter-body, the material was stuck on the counter-body as shown in the optical micrograph of the Figure 4.26(a) and magnified view in Figure 4.26(b). It has been referred in the literature that the material may itself tear off at greater loads friction weld to the counter-surface. The galled material appears as gouged with the torn lump of the material stuck to the surface of the counter-body. This galling is further reduced when the concentration of graphite was increased to 10 wt. % and signs of abrasive damage to the counter-body indicating the resistance of the 10. wt. % coating to abrasion itself. These black marks can be carbon deposits that are the part of the partial tribo-film formed on the surface. The counter-body of 10 wt. % graphite Ni-WC coating presents slight abrasion in the form of wider grooves and deep, signifying the significant damage that the coating has caused to the counter-body. There are black patches of oxide or tribo film that may have formed, but mainly the shiny steel and the grooves appearance indicate that the wear was mainly composed of abrasive based phenomenon.

Although galled material is not present, sheared tribo film chunks are also evident as depicted in the magnified view of Figure 4.26(f). The surface coverage of adhesion and abrasion is both ample enough to allow the greater portion of counter-body being involved in the sliding wear. The blackish areas and un-shiny non-conducive surface the counter-body are depicting carbon deposits or the possibility of the formation or partial formation of a tribo film easily shearable. This depiction may correlate with the least

friction coefficient that has been seen previously. There are no signs of wider grooves present Figure 4.26(e) showing material removal rate was comparatively quite lesser and their depth is far lesser than the 10 wt. % graphite coating (Figure 4.26(d)).

The amount of wear debris generated during dry sliding of Ni-WC coating with a variation of the percentage of graphite concentration is presented in Figure 4.27. The morphology, size, color and type of debris are also indicative of the wear mechanism that ensued the sliding of two hard bodies relative to each other. During wear, the material is transferred again and again between the sliding surfaces and is ejected eventually (Deuis et al., 1997). Upon closer examination of the quantity of debris generated, it is found that the amount of debris generated is greater for 5 wt. % graphite based coating that subsequently reduces as this concentration increases to 10 wt. %. This is also indicative of the severity of wear decreasing as the particle size of debris also decreases when the concentration increases. Ferrous whitish particles in higher concentration were found in 5 wt. % coating with debris size in the range of 100 μm to few micrometres are present showing that these hard abrasives further assisted in the cutting of the coating to produce abrasive marks as the sliding progresses. Further to this blackish oxidized aluminium debris with a size range of 400 μm indicating greater material removal was observed. The majority of the wear debris as oxidized was equiaxed. The signs of delamination wear or plate-like debris was absent in all coatings when compared with the substrate wear showing that the material removed was progressing through abrasive means. As the concentration of whitish particles decreases, the size of debris removed from the coating also reduces and higher number of equiaxed particles are generated which is more visible in SEM micrographs as presented in Figure 4.27 (e) and (f). It is believed that the iron material detached from the counter-face due to abrasive nature of the carbide reinforcement phase and is oxidized upon transfer film formation. The increase in solid lubricant phase in the

matrix decreases the micro cutting effect of carbide phase that may result in the lesser generation of third body abrasives (Deuis et al., 1997). In another study it was mentioned that as the amount of graphite increases, the size of the debris particles reduces which correlates to a reduction in surface roughness and width of wear grooves (Hirschhron & Daver, 1969).

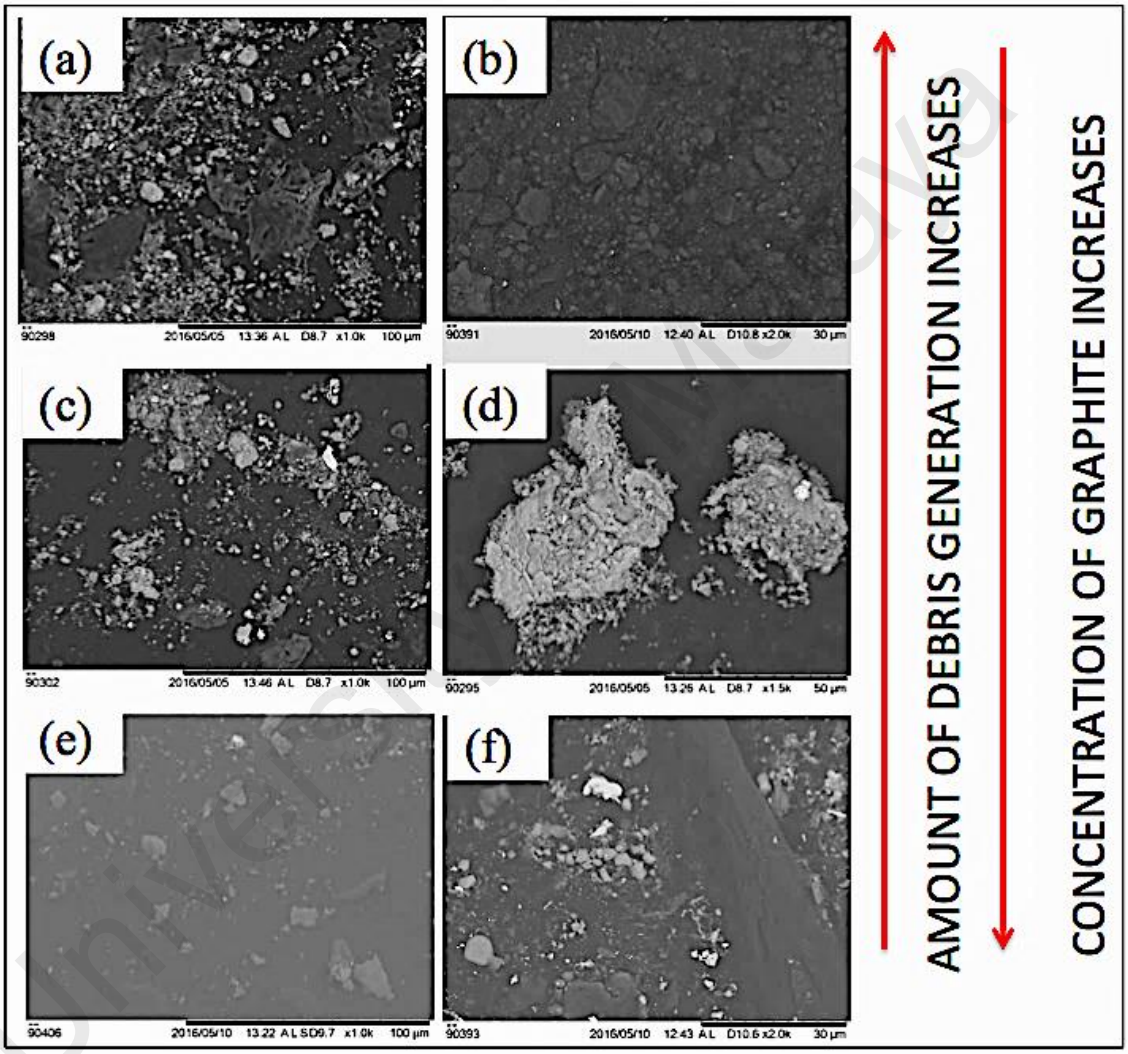

Figure 4.27: SEM images of counter-body worn debris at lower and higher magnification for (a), (b) 5 wt. % graphite (c), (d) 10 wt. % graphite, (e), (f) 15 wt. % graphite

Since, with the addition of solid lubricants, they enter in between the surfaces that are under frictional load. The hard WC particles create the deformation resistance in the composite that is mating the hard steel counter body, thus the contact area is reduced during the wear process. WC has excellent wear resistance and is brittle, but very hard having a Vickers hardness of 2900 H_v (ranks about 9 on Mohs scale) thus, improves the wear resistance of the composite coating. Thereafter, the graphite particles come in the wearing process. Since graphite has a layered structure and get sheared and tear away. It has lower hardness and they flake in patches, thus are able to transfer and coat onto the wear surface. Further to this, these graphite particles can also fill pores that are formed due to the abrasive particles pull-out. Thus, with the increase in graphite as a solid lubricant, the formation of transfer film and pores fill out improves thereby, gradually reducing the wear rates and friction coefficient (B Podgornik et al., 2015).

4.5.4 Wear characteristics of Ni-WC-TiO_2 coating

Literature, review points out to the fact that the addition of TiO_2 in nickel-based coatings is beneficial in reducing wear substantially (W. Chen et al., 2010). In this section, discussion shall be made on wear characteristics of Ni-WC-TiO_2 coatings based on worn scar, counter-body and debris analysis.

4.5.4.1 Characterization of worn surface

The SEM images of the worn surface along with their EDX area mapping of titanium element (Ti-kα) for varying concentration of TiO_2 additive is depicted in Figure 4.28. As observed, the amount of retained debris on the scar due to cutting action of carbide phase and the resulting intensity of abrasion in the form of grooves is found to have decreased with the concentration of additive put in the composite mixture.

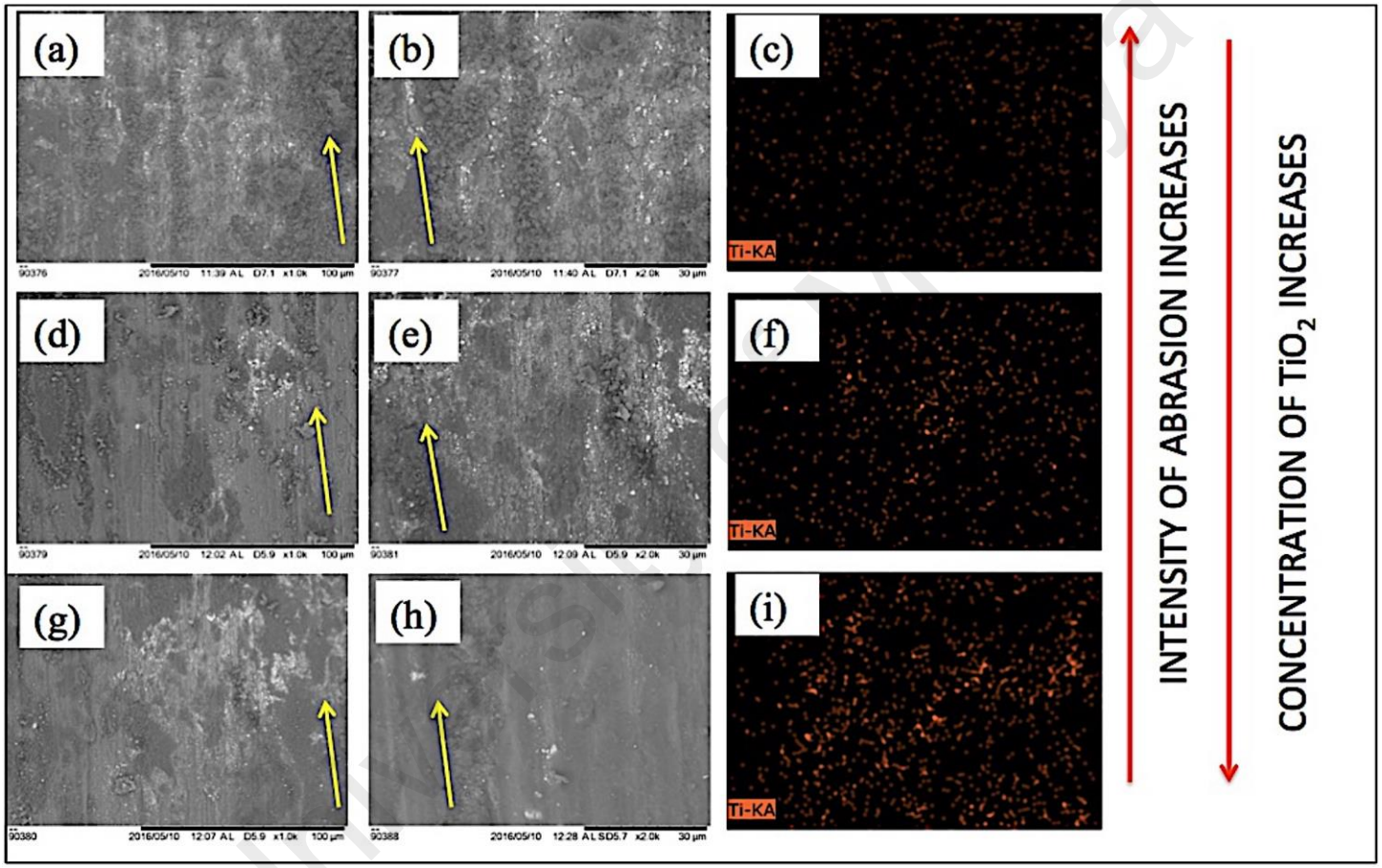

Figure 4.28: SEM image of coating with their magnified view for (a), (b) 5 wt. % TiO_2 (d), (e) 10 wt. % TiO_2, (g), (h) 15 wt. % TiO_2, along with their corresponding EDX titanium element mapping in (c), (f) and (i).

The EDS area maps in Figure 4.28(c), (f) and (i) shows that as the TiO_2 concentration in the Ni-WC coating increases, the amount of debris in the form of oxidized tribo-film reduces, signifying the resulting decrease in material removal rate. When TiO_2 is found to be in 5 and 10 wt. % in the coating, dark greyish matters were also found on the wear tracks. This indicates that chunks of delaminated sheets may have detached from the coating and may have adhered onto the counters-surface thereafter during the cyclic sliding process under higher contact pressure, the adhered mechanically mixed materials may have oxidized and ejected from the counter surface in the form of oxidized debris. Signs of shallow craters to identify delamination of materials are also present (Figure 4.28 (e)). It may also be observed ((Figure 4.28 (g)) that the worn scar morphology is much smoother indicating the efficiency of a greater amount of additive in reducing damage. The reduction in wear with the incorporation of TiO_2 was studied in electroplated nickel (Y Wang et al., 2014). They inferred that the embedment of TiO_2 in Ni matrix was able to able to reduce the direct contact of coating with abrasives and counter-face during the sliding wear.

Figure 4.29 shows the EDS spot scanning spectrums to analyze the amount of oxidation that took place during tribological wear of the Ni-WC-TiO_2 coating. The intensity in oxygen concentration further dictates that the wear mechanism was contributed partially by means of oxidative wear, which was more dominant in coatings with a higher concentration of TiO_2. In some studies carried out (G. R. Yang et al., 2015), it was indicated that the worn scar morphology comprised of debris containing oxides and graphite covering on the worn surface. The Ni/WC/G coating produced from vacuum coating was found to show excellent wear resistance.

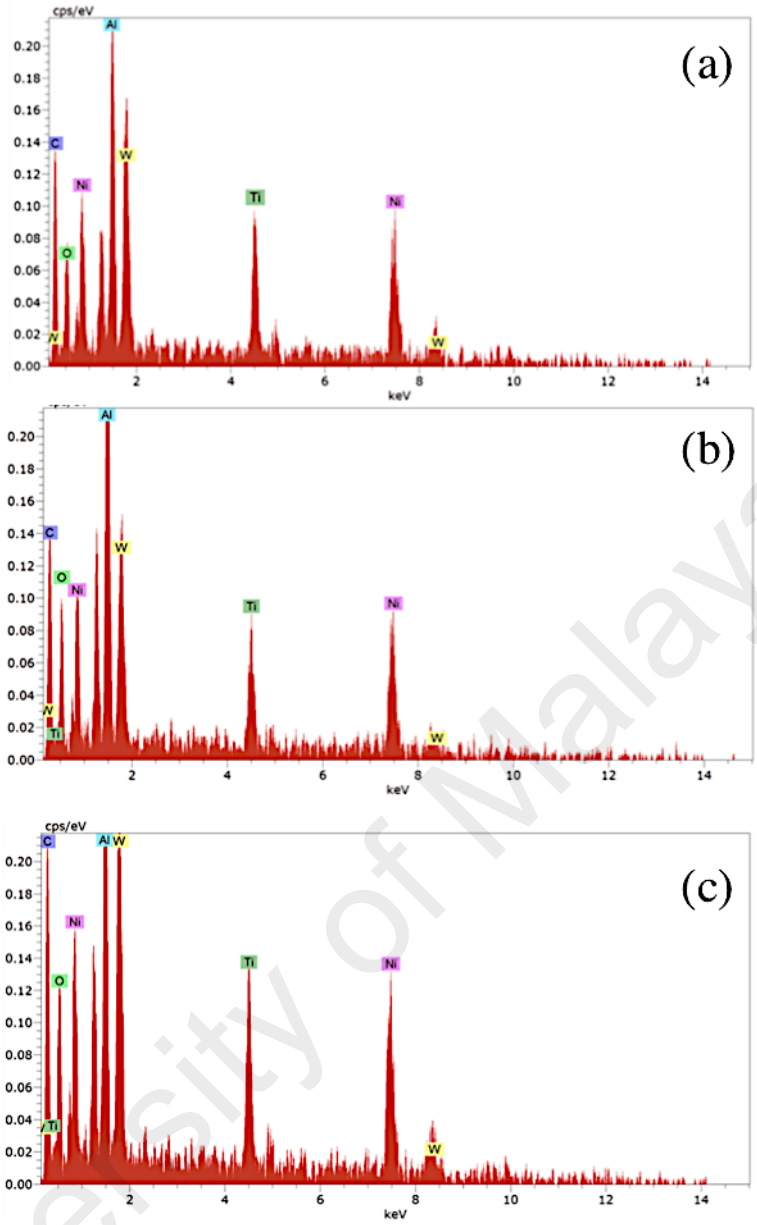

Figure 4.29: EDS spot scanning spectrums on worn scars of (a) Ni-WC-5 wt. % TiO_2, (b) Ni-WC-10 wt. % TiO_2 and (c) Ni-WC-15 wt. % TiO_2

4.5.4.2 Counter-body wear and debris analysis

The optical microscopic images taken from the counter-bodies that slid against Ni-WC coating comprising of varying amounts of TiO_2 additive is presented in Figure 4.30. As a general observation, it is noted that the degree of adhesion and abrasion wear decreases with the increasing amounts of TiO_2. The magnified view of the counter-body

for Figure 4.30(b) signifies adhesion in the form of shiny material being captured surrounded by oxidized traces of the partial tribo-layer. The intensity of black form of oxidized tribo-chemical film is observed to be patchy on the counter body with 10 wt. % TiO_2 (Figure 4.30(d)) and seems to be more uniform when this amount increases (Figure 4.30(f)). It is to be noted that the significant decrease in the abrasion for 15 wt. % TiO_2 is deduced to be due to the formation of grooves that are lesser in quantity, shallow and are narrow. In contrast, Figure 4.30(a) and (c) shows a greater number of grooves formation with an extensive amount of ploughing leading to deeper and wider grooves materialization.

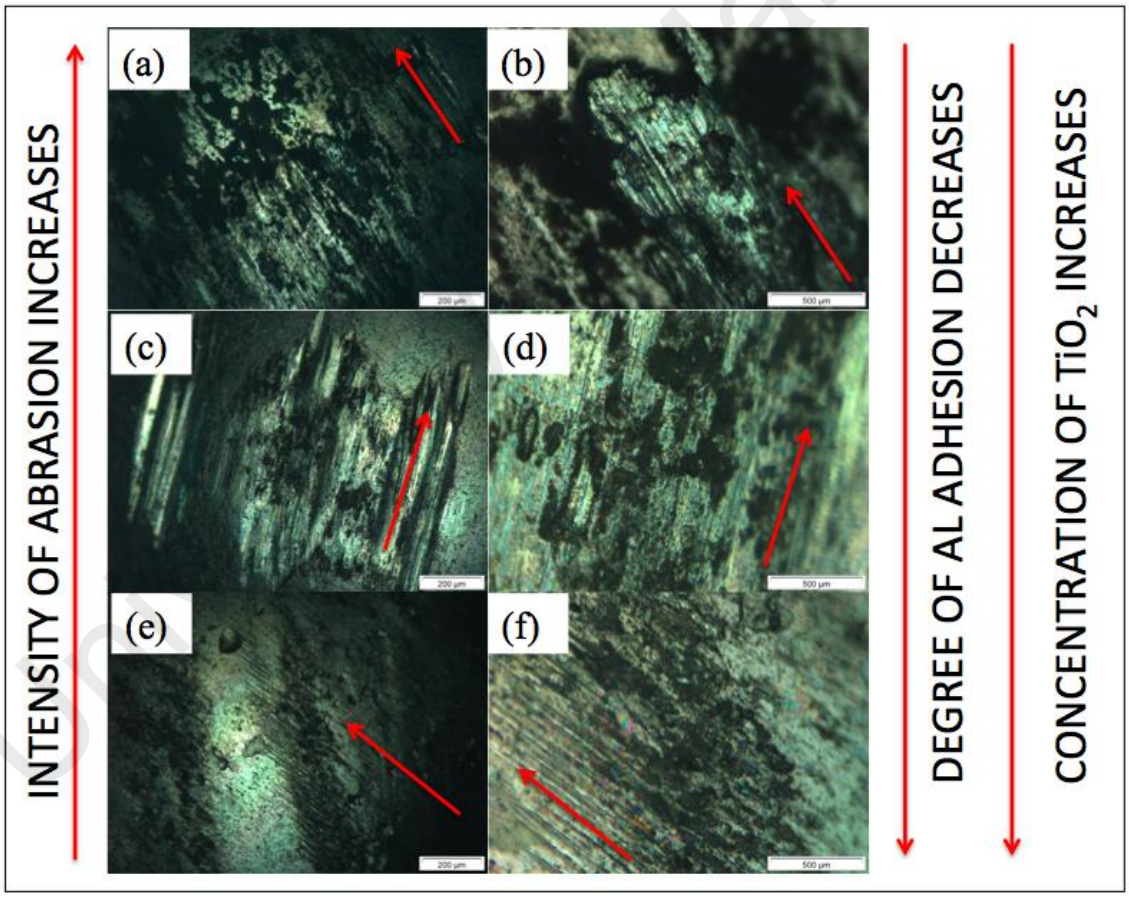

Figure 4.30: Optical micrographic images of counter-body worn tracks at lower and higher magnification views for (a), (b) 5 wt. % TiO_2 (d), (e) 10 wt. % TiO_2, (g), (h) 15 wt. % TiO_2

The amount and type of debris generated when the quantity of TiO_2 added is varied has been presented in Figure 4.31. As shown in Figure 4.31(a), greater sized chunks removal covered in smaller oxide debris was the characteristics of 5 wt. % TiO_2 Ni-WC coating. The whiter chunks were the part of the ferrous counter body that played a part in cutting as abrasives to induce wider and deeper grooves in the form of peaks and valleys. Upon closer examination of the wear debris, "undistorted wear grooves" signifying the signs of adhesive wear through gross material pull-out was observed. Significant change in terms of quantity of debris, though, is not observed for 10 wt. % TiO_2 Ni-WC coating however, the quantity of ferrous counter body debris or carbide abrasive pull-out is not observed. The debris in the case of 15 wt. % TiO_2 Ni-WC coating was found to be more of oxidative and was in the form of trapped or compacted. Herein, smaller particles generated during tribo chemical wear were ejected as the quantity to maintain critical thickness of the tribo-film started to reach a critical stage wherein the adhesion force between the film and the counter-body can no longer hold the new particles and hence are ejected so as to allow newly generated particles to adhere to the counter-body as a shear-able film. Since, TiO_2 is added as an additive that various other researchers have shown the beneficial effects of it (Chao & Liang, 2004) in reducing both friction and wear.

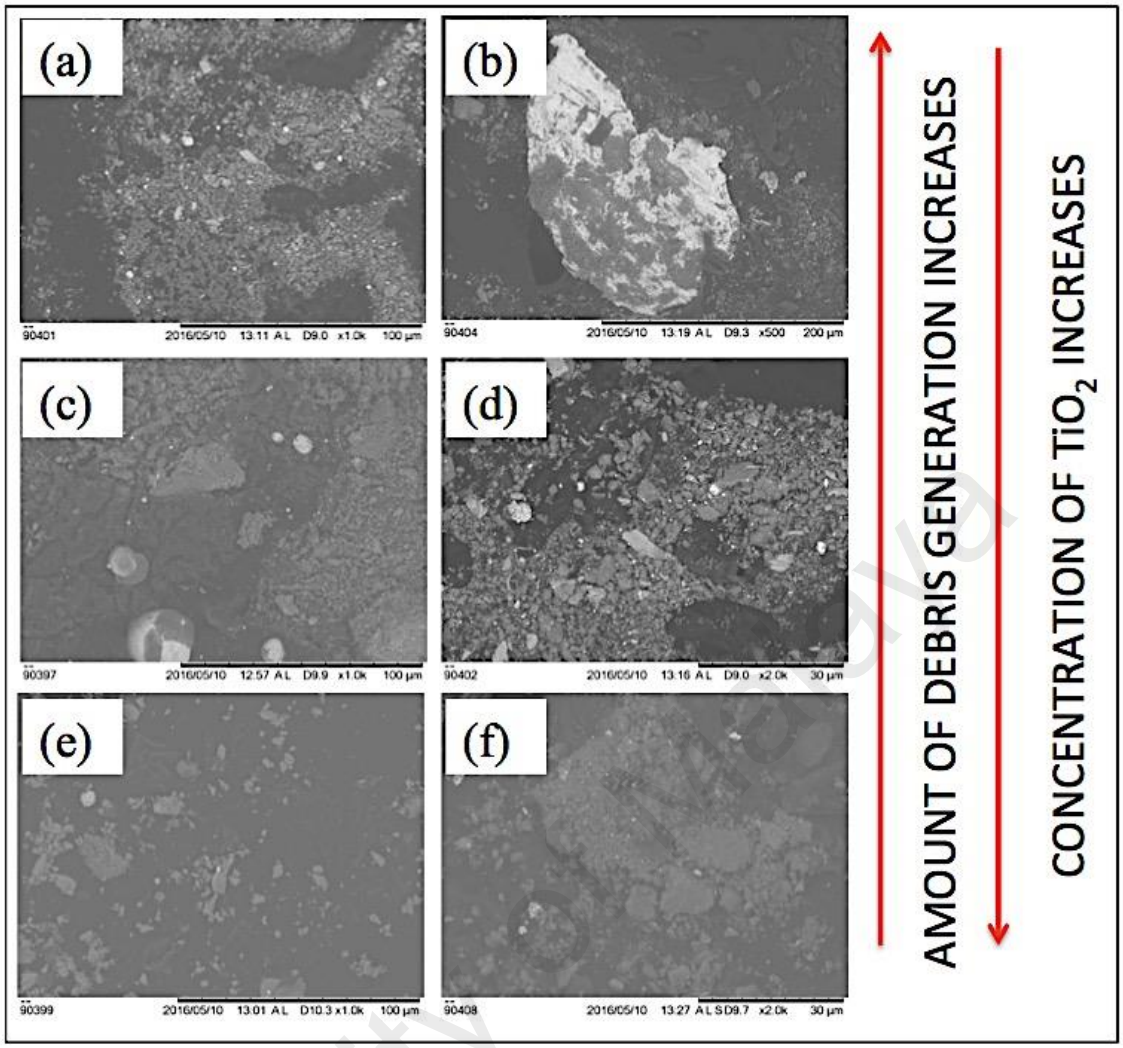

Figure 4.31: SEM images of counter-body worn debris at lower and higher magnification for (a), (b) 5 wt. % TiO_2 (c), (d) 10 wt. % TiO_2, (e), (f) 15 wt. % TiO_2

4.6 Comparative Evaluations

In this section, comparative evaluation in results obtained for substrates, MMC coating and HMMC coatings are discussed.

4.6.1 3D Surface scans and roughness profilometry of worn scars for AA5083, Al-17Si, MMC and HMMC coatings

Figure 4.32 identifies the worn scars 3D optical surface scans for AA5083, Al-17Si, Ni-WC, Ni-WC-15 wt. % graphite and Ni-WC-15 wt. % TiO_2. Visible, in terms of wear

depth, the substrates have undergone comparatively severe wear scar profiles than the coatings. Higher hardness and Si inclusions in Al-17Si alloy are somewhat more wear resistant than the wrought AA5083 alloy. However, this severity seems to reduce when these samples are coated. These 3D worn scar images corresponding to the SEM worn scar morphology, debris micrographs, and counter-surface corroborates and are helpful in determining the multiple wear mechanisms and the main mechanisms involved. The hard WC particles create the deformation resistance in the composite that is mating the hard steel counter body thus, the contact area is reduced. The nickel aluminum intermetallic phase is able to hold these harder carbide phases and acts as a supporting phase.

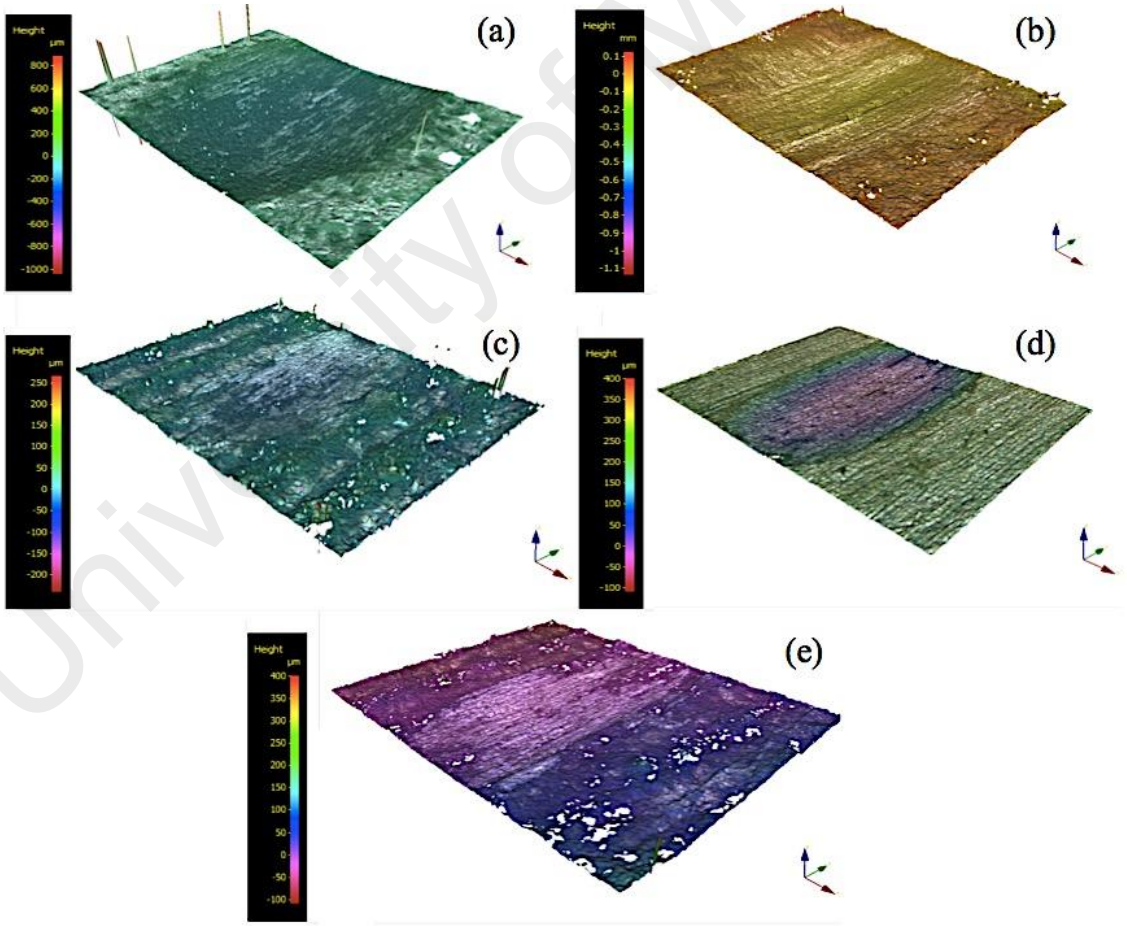

Figure 4.32: 3D surface scans for (a) AA5083, (b) Al-17Si (c) Ni-WC, (d) Ni-WC-15 wt. % Graphite (e) Ni-WC-15 wt. % TiO_2

Figure 4.33 shows the surface roughness measurement on worn scars for the substrates and coatings. Ranking-wise, the highest surface roughness is for AA5083 that is followed by Al-17Si substrate, MMC Ni-WC coating, HMMC Ni-WC-15 wt. % TiO_2 with the least being exhibited by Ni-WC-15 wt. % Graphite. The minimum surface roughness of around 200nm is observed for Ni-WC-15 wt. % graphite coating, which is almost 3 times lesser than Al-17Si substrate.

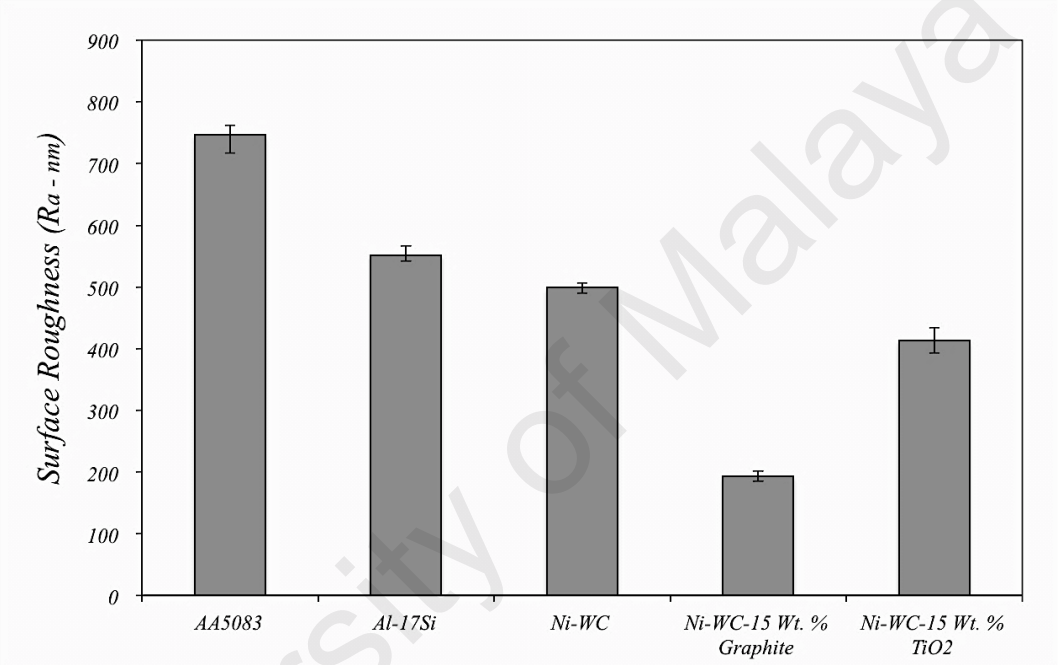

Figure 4.33: Surface roughness (R_a) of worn scars in nano-meters for substrates and coatings.

The surface profilometry scans of worn scars were carried out by Mitoyo roughness profilometer for AA5083 and Al-17Si substrate, MMC Ni-WC coating, HMMC Ni-WC-15 wt. % graphite and HMMC Ni-WC-15 wt. % TiO_2 (Figure 4.34). The depth of grooves can be observed in the form of peaks and valleys. From the surface profilometry across the scars, the maximum groove depth inside the wear scar between pile-ups is approximately 2.8μm for Al-17Si followed by AA5083 (2μm), Ni-WC (1.8μm), Ni-WC-15 wt. % TiO_2 (1.2μm) and the least wear depth related to Ni-WC-15

wt. % Graphite (0.7μm). In one research it was mentioned that as the amount of graphite in Ni-WC coating increases, a reduction in surface roughness and width of wear grooves is observed (Hirschhron & Daver, 1969). These observations of the wear grooves formation and the roughness after wear are consistent with the interpretation and analysis of results provided earlier in debris and worn scar morphology section.

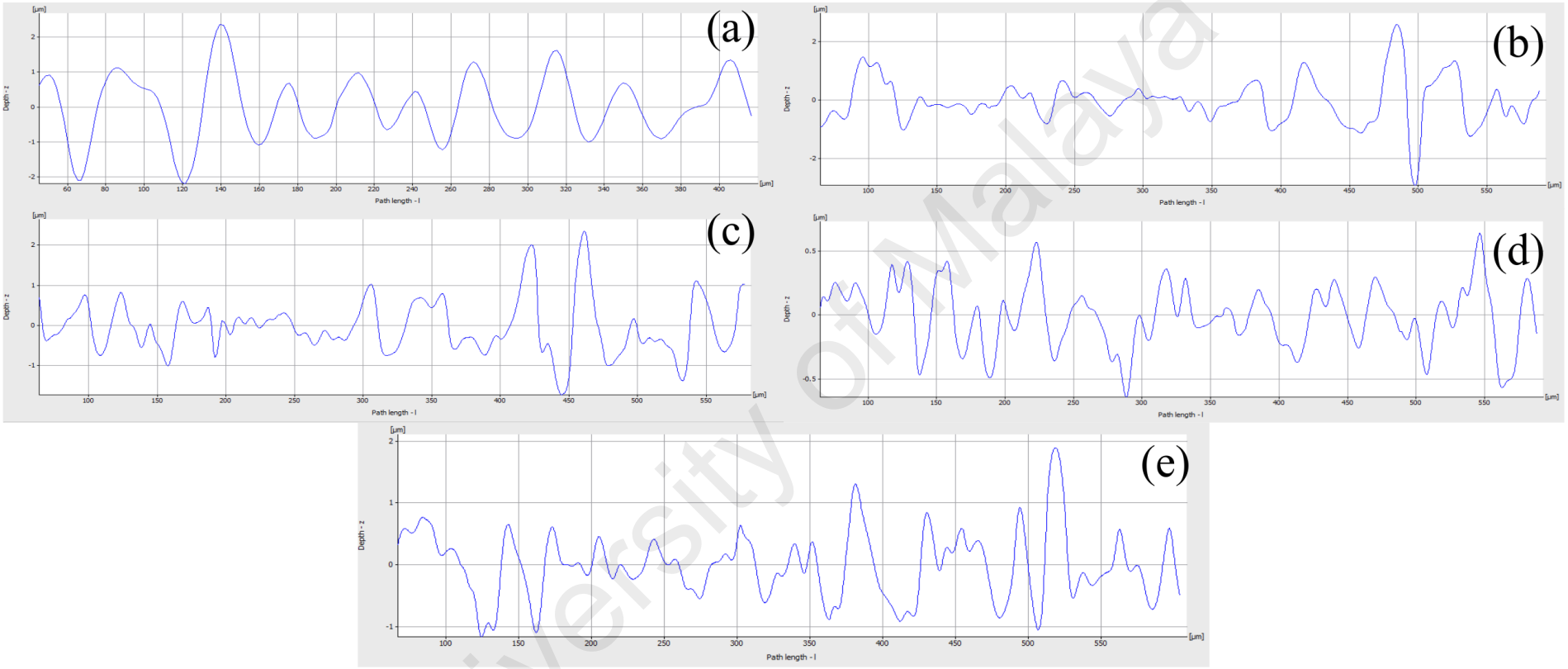

Figure 4.34: Surface profilometry scans for (a) AA5083, (b) Al-17Si (c) Ni-WC, (d) Ni-WC-15 wt. % Graphite (e) Ni-WC-15 wt. % TiO_2.

4.6.2 Comparative evaluation of wear mechanism for AA5083, Al-17Si, MMC and HMMC coatings

Table 4.7 presents a summary of tribo-mechanical properties of substrates and coatings that were obtained in the current research. A comparative evaluation is necessary for determining the degree of effectiveness of doping on wear resistance of HMMC coatings and the change in mechanisms due to which the tribological properties enhancement is brought. Furthermore, the degree of damage prevented for substrate must be realized so as to gain understanding as to how the laser composite surfacing has been beneficial in reducing friction and wear. Hence, the identification of wear mechanism in terms of severity shall be made for substrate AA5083 wrought and Al-17Si cast alloy in addition to the comparison of wear mechanism for MMC Ni-WC coating and HMMC Ni-WC-Graphite and Ni-WC-TiO_2.

Table 4.7: A summary of Tribo-mecahnical properties of substrates and coatings

Tribo-Mechanical Properties	**Surface Hardness (H_v)**	**Surface Roughness Ra after wear (nm)**	**Wear (mg)**	**Friction Coefficient**
Substrates				
AA5083	87	747	1.30	0.43
Al-17Si	92	552	0.70	0.47
MMC Coating				
Ni-WC	953	499	0.66	0.32
HMMC Coatings				
Ni-WC-5 Wt. % Gr	790	311	0.33	0.29
Ni-WC-10 Wt. % Gr	749	256	0.24	0.3
Ni-WC-15 Wt. % Gr	711	194	0.10	0.21
Ni-WC-5 Wt. % TiO_2	845	510	0.33	0.35
Ni-WC-10 Wt. % TiO_2	810	459	0.18	0.29
Ni-WC-15 Wt. % TiO_2	785	413	0.13	0.24

Under dry sliding conditions, the majority wear mechanisms that have been identified in the current research, are categorized as oxidative, abrasive, adhesive, delamination, extrusion or melting and fatigue induced wear. The deduction of wear mechanisms has been made based on the analysis carried out for the worn scar, counter-face and debris for both substrate and coating. Table 4.8 illustrates a summary of the wear mechanisms that have been identified for substrate, MMC and HMMC coatings. As a general overview, it is quite evident that the base alloy substrates have undergone intense abrasion with adhesion on their respective counter-bodies and faster material removal in the form of delaminated large wear debris. In contrast to the wrought alloy AA5083, the hypereutectic Al-17Si experiences comparatively lesser adhesion along with abrasion but the wear debris was slightly extruded as if melted or softened. Further to this fatigue induced cracks were also present, but Si reinforcement was particularly an advantage in reducing both friction and wear for these Al-Si cast alloys. When AA5083 was coated with Ni-WC MMC coating, the degree of abrasion, adhesion, and delamination was significantly reduced and moderate oxidative wear was seen. Interesting results were seen when 5-wt. % graphite was added in Ni-WC coating deposited on Al-Si alloy. Fatigue cracks on worn scar with mild extrusion of adhered material on the counter-face were characterized, however; the degree of delamination, abrasion and adhesion had already fallen. Additionally, more of a positive effect on the intensity of wear was observed when the concentration of graphite was further raised and oxidative mild wear was observed as the main wear mechanism involved. This was due to the fact that the transfer film generated between the counter face and the sliding area was formed more uniformly and the shear-able graphite was able to further reduce the friction. In the case of 5 wt. % TiO_2, the intensities of all wear mechanisms involved with MMC coatings were slightly reduced.

Table 4.8: Comparative analyses of wear mechanisms for substrates, MMC and HMMC coatings based on worn scar, debris and counter-body morphology

	Wear mechanisms					
	Abrasion	**Oxidation**	**Delamination**	**Adhesion**	**Softening/ /Material extrusion**	**Fatigue cracks**
Substrates						
AA5083	✓✓✓✓		✓✓✓	✓✓✓✓		
Al-17Si	✓✓✓	✓	✓✓	✓✓	✓✓	✓✓
MMC Coating						
Ni-WC	✓✓✓	✓✓	✓	✓✓✓		
HMMC Coating						
Ni-WC-5 Wt. % Graphite	✓✓		✓	✓✓✓	✓✓	✓✓
Ni-WC-10 Wt. % Graphite	✓	✓	✓	✓	✓	
Ni-WC-15 Wt. % Graphite	✓	✓✓		✓		
Ni-WC-5 Wt. % TiO2	✓✓✓	✓	✓	✓✓✓	✓	
Ni-WC-10 Wt. % TiO2	✓✓✓	✓		✓✓		
Ni-WC-15 Wt. % TiO2	✓✓	✓✓		✓		

*The relative extent of each wear mechanism: ✓: slight; ✓✓: moderate; ✓✓✓: heavy; ✓✓✓✓ Very heavy:

However, when TiO_2 in 10 and 15 wt. % was added in MMC coating, delamination, fatigue cracks and extrusion was completely evaded. However, the intensities of abrasion and adhesion were a bit higher as compared with coatings containing higher concentrations of graphite. It can be well established that the softer aluminium substrates can significantly gain advantages from the fabrication of MMC coatings, especially when additives are added to enhance their tribological performance by reducing the intensities of wear mechanisms involved.

CHAPTER 5: CONCLUSION AND FUTURE WORK

The conclusion section is followed by the future work outlook, which is recommended as a follow-up to the present study. The conclusions are aligned with the research objectives and have been elaborated and summed up in the form of each result which was obtained.

5.1 Conclusion

The following main conclusions were drawn from this research:

1. An MMC Ni-WC coated AA5083 alloy was made with a hardness of 953 H_v and wear resistance of 2.5 times that of AA5083 was achieved

2. HMMC coated Ni-WC-Graphite and Ni-WC-TiO_2 Al-17Si was made with the surface hardness of 781 H_v and 825 H_v respectively. The wear resistance obtained was 7 and 5 times to that of Al-17Si substrate respectively.

3. The HMMC coatings presented far superior tribological properties when compared to MMC coatings. Graphite and TiO_2 based coatings were able to suppress extensive adhesion and abrasion, which were the main wear mechanisms as observed for substrates and MMC coatings.

5.2 Future Work

The performance of the wear resistant laser based coatings is mainly limited by the high friction coefficient, higher surface roughness and lower toughness. It is believed that progress on these aforementioned fronts is necessary to drive efficiency of wear resistant hard facing coatings leading to economical, efficient and environmentally benign components.

1. As laser processing itself is a highly sensitive process, hence stringent control of lasing parameters such as incident beam quality and wavelength, interaction time, temperature gradients, and power density are vital. Thus, the selection and optimization of these process parameters are essential to obtain defect-free coatings. So far, researchers have focused on understanding the effect of the processing parameters and design of cladding systems, however, various optimization methods such as Taguchi, fuzzy logic approach, grey relational analysis, and genetic algorithm have not been taken into account.
2. Numerous prospects of fabricating "hybrid metal matrix composites" comprising of oxide, sulfide, and halide-based solid lubricating phase and hard ceramic phase are available. Another unique opportunity lies in the addition of nano-sized particulates and nano material components. Slight additions of nano particles (0.5–2 Vol.-%) produce more pronounced effects. These materials may act as nuclei agents to produce extremely fine microstructures. Hence, it would be interesting to see their interaction with lasers for fabrication of aluminum based nano composites and metal-ceramic systems.
3. It is quite essential to accommodate solid lubricant growth in the industrial sectors through a sustainable manner. Solid lubrication is exceptionally important for tribological applications where components are operating under extreme environment or when there is a chance of liquid lubricant to cease its function. Solid lubricants such as soft metals and their oxides, graphene, selenides have not been investigated in laser claddings.
4. Apart from solid lubricants, the simultaneous addition of rare earth elements and their oxides to investigate the tribo-mechanical performance of hybrid metal matrix composite coatings deposited on light metals such as titanium, magnesium and

aluminium have still not been investigated. The rare earth elements are found to improve microstructure and induce grain refinement effects.

5. It is quiet important to investigate the effect of the addition of greater concentrations of solid lubricants exceeding the concentration of 15 wt. % that has been employed in this research. Further to this, the balance in mechanical and tribological performance is required to be examined, based on the applications that have been targeted for the research work undertaken.

REFERENCES

Adachi, S., & Inami, J. (1998). Valve seat-bonded cylinder head and method for producing same: Patent No. US5742020 A.

Aghayan, M., & Narayanswamy, S. (2015). Morphology based statistical analysis of nanosecond pulsed laser texturing of the multicrystalline silicon. *Journal of Laser Applications, 27*(3), 032002. doi:doi:http://dx.doi.org/10.2351/1.4917043

Allen, C., & Ball, A. (1996). A review of the performance of engineering materials under prevalent tribological and wear situations in South African industries. *Tribology International, 29*(2), 105-116. doi:http://dx.doi.org/10.1016/0301-679X(95)00073-D

Almeida, A., Anjos, M., Vilar, R., Li, R., Ferreira, M. G. S., Steen, W. M., & Watkins, K. G. (1995). Laser alloying of aluminium alloys with chromium. *Surface and Coatings Technology, 70*(2), 221-229.

Almeida, A., Carvalho, F., Carvalho, P. A., & Vilar, R. (2006). Laser developed Al–Mo surface alloys: Microstructure, mechanical and wear behaviour. *Surface and Coatings Technology, 200*(16), 4782-4790.

Anandkumar, R., Almeida, A., Colaço, R., Vilar, R., Ocelik, V., & De Hosson, J. T. M. (2007). Microstructure and wear studies of laser clad Al-Si/SiC(p) composite coatings. *Surface and Coatings Technology, 201*(24), 9497-9505.

Anandkumar, R., Almeida, A., & Vilar, R. (2011). Wear behavior of Al–12Si/TiB2 coatings produced by laser cladding. *Surface and Coatings Technology, 205*(13–14), 3824-3832. doi:http://dx.doi.org/10.1016/j.surfcoat.2011.01.048

Anandkumar, R., Almeida, A., & Vilar, R. (2012). Microstructure and sliding wear resistance of an Al–12wt.% Si/TiC laser clad coating. *Wear, 282*, 31-39.

Ang, L. K., Lau, Y. Y., Gilgenbach, R. M., & Spindler, H. L. (1997). Analysis of laser absorption on a rough metal surface. *Applied physics letters, 70*(6), 696-698.

Aouadi, S. M., Gao, H., Martini, A., Scharf, T. W., & Muratore, C. (2014). Lubricious oxide coatings for extreme temperature applications: A review. *Surface and Coatings Technology, 257*, 266-277.

Arato, T., Aono, Y., Tsuruoka, S., & Komuro, K. (1996). Ceramic-particle-dispersed metallic member, manufacturing method of same and use of same: Patent No. US5589652 A.

Arnold, J., & Volz, R. (1999). Laser powder technology for cladding and welding. *Journal of thermal spray technology, 8*(2), 243-248.

Arslan, A., Masjuki, H. H., Varman, M., Kalam, M. A., Quazi, M. M., Al Mahmud, K. A. H., Gulzar, M., & Habibullah, M. (2015). Effects of texture diameter and depth on the tribological performance of DLC coating under lubricated sliding

condition. *Applied Surface Science, 356*, 1135-1149. doi:http://dx.doi.org/10.1016/j.apsusc.2015.08.194

Avril, L., Courant, B., & Hantzpergue, J. J. (2006). Tribological performance of α-Fe(Cr)-Fe2B-FeB and α-Fe(Cr)-h-BN coatings obtained by laser melting. *Wear, 260*(4–5), 351-360. doi:http://dx.doi.org/10.1016/j.wear.2005.04.012

Baghery, P., Farzam, M., Mousavi, A. B., & Hosseini, M. (2010). Ni–TiO2 nanocomposite coating with high resistance to corrosion and wear. *Surface and Coatings Technology, 204*(23), 3804-3810. doi:http://dx.doi.org/10.1016/j.surfcoat.2010.04.061

Bao, R., Yu, H., Chen, C., & Dong, Q. (2006). The effect of rare earth on the structure and performance of laser clad coatings. *Surface Review and Letters, 13*(04), 509-517. doi:doi:10.1142/S0218625X0600875X

Bartkowski, D., Młynarczak, A., Piasecki, A., Dudziak, B., Gościański, M., & Bartkowska, A. (2015). Microstructure, microhardness and corrosion resistance of Stellite-6 coatings reinforced with WC particles using laser cladding. *Optics & Laser Technology, 68*(0), 191-201. doi:http://dx.doi.org/10.1016/j.optlastec.2014.12.005

Basavarajappa, S., Chandramohan, G., Mukund, K., Ashwin, M., & Prabu, M. (2006). Dry sliding wear behavior of Al 2219/SiCp-Gr hybrid metal matrix composites. *Journal of materials engineering and performance, 15*(6), 668-674.

Bathula, S., Anandani, R. C., Dhar, A., & Srivastava, A. K. (2012). Microstructural features and mechanical properties of Al 5083/SiCp metal matrix nanocomposites produced by high energy ball milling and spark plasma sintering. *Materials Science and Engineering: A, 545*(0), 97-102. doi:http://dx.doi.org/10.1016/j.msea.2012.02.095

Belanger, P.-A., & Rioux, M. (1978). Ring pattern of a lens-axicon doublet illuminated by a Gaussian beam. *Applied optics, 17*(7), 1080-1088.

Bergmann, H. W., & Mordike, B. L. (1986). Laser surface melting. *NASA STI/Recon Technical Report N, 88*, 21435.

Bi, Q., Zhu, S., & Liu, W. (2013). High Temperature Self-Lubricating Materials. *Tribology in Engineering, 1*, 109-133.

Bidmeshki, C., Abouei, V., Saghafian, H., Shabestari, S. G., & Noghani, M. T. Effect of Mn addition on Fe-rich intermetallics morphology and dry sliding wear investigation of hypereutectic Al-17.5%Si alloys. *Journal of Materials Research and Technology*. doi:http://dx.doi.org/10.1016/j.jmrt.2015.11.008

Binnig, G., Quate, C. F., & Gerber, C. (1986). Atomic force microscope. *Physical review letters, 56*(9), 930.

Biswas, S. K. (2006). Wear of metals: a material approach. *Wear, Materials, Mechanisms and Practices. John Wiley & Sons, Ltd*, 21-36.

Blum, R., & Molian, P. (2014). CO2 laser coating of nanodiamond on aluminum using an annular beam. *Applied Surface Science, 288*, 1-8.

Bose, S., & Bandyopadhyay, A. (2015). Wear resistant low friction coefficient surfaces for joint and bone replacement materials and devices: Patent No. US20150004209 A1.

Brückner, F., Lepski, D., & Beyer, E. (2007). Modeling the influence of process parameters and additional heat sources on residual stresses in laser cladding. *Journal of thermal spray technology, 16*(3), 355-373.

Buchbinder, D., Meiners, W., Wissenbach, K., & Poprawe, R. (2015). Selective laser melting of aluminum die-cast alloy—Correlations between process parameters, solidification conditions, and resulting mechanical properties. *Journal of Laser Applications, 27*(S2), S29205. doi:doi:http://dx.doi.org/10.2351/1.4906389

Cai, Z.-B., Zhu, M.-H., & Lin, X.-Z. (2010). Friction and wear of 7075 aluminum alloy induced by torsional fretting. *Transactions of Nonferrous Metals Society of China, 20*(3), 371-376.

Carey, C., Cantwell, W. J., Dearden, G., Edwards, K. R., Edwardson, S. P., Mullett, J. D., Williams, C. J., & Watkins, K. G. (2007). *Effects of laser interaction with graphite coatings.* Paper presented at the Proceedings of the Laser Assisted Net Shape Engineering.

Chandrashekharaiah, T. M., & Kori, S. A. (2009). Effect of grain refinement and modification on the dry sliding wear behaviour of eutectic Al–Si alloys. *Tribology International, 42*(1), 59-65. doi:http://dx.doi.org/10.1016/j.triboint.2008.05.012

Chao, M.-J., & Liang, E.-J. (2004). Effect of TiO2-doping on the microstructure and the wear properties of laser-clad nickel-based coatings. *Surface and Coatings Technology, 179*(2–3), 265-271. doi:http://dx.doi.org/10.1016/S0257-8972(03)00857-0

Chatterjee, S., Majumdar, J. D., Shariff, S. M., Padmanabham, G., & Choudhury, A. R. (2012). Effect of laser post-treatment on Al2O3-TiB2-TiN composite coating with free hBN. *The International Journal of Advanced Manufacturing Technology, 61*(5-8), 559-567.

Chen, W., He, Y., & Gao, W. (2010). Electrodeposition of sol-enhanced nanostructured Ni-TiO2 composite coatings. *Surface and Coatings Technology, 204*(15), 2487-2492. doi:http://dx.doi.org/10.1016/j.surfcoat.2010.01.036

Chen, Y., Wu, D., Ma, G., Lu, W., & Guo, D. (2013). Coaxial laser cladding of Al2O3-13% TiO2 powders on Ti-6Al-4V alloy. *Surface and Coatings Technology, 228*, S452-S455.

Choi, W., Lahiri, I., Seelaboyina, R., & Kang, Y. S. (2010). Synthesis of graphene and its applications: a review. *Critical Reviews in Solid State and Materials Sciences, 35*(1), 52-71.

Chong, P. H., Man, H. C., & Yue, T. M. (2001). Microstructure and wear properties of laser surface-cladded Mo–WC MMC on AA6061 aluminum alloy. *Surface and Coatings Technology, 145*(1), 51-59.

Chong, P. H., Man, H. C., & Yue, T. M. (2002). Laser fabrication of Mo-TiC MMC on AA6061 aluminum alloy surface. *Surface and Coatings Technology, 154*(2), 268-275.

Choudhury, A. R., Ezz, T., Chatterjee, S., & Li, L. (2008). Microstructure and tribological behaviour of nano-structured metal matrix composite boride coatings synthesized by combined laser and sol–gel technology. *Surface and Coatings Technology, 202*(13), 2817-2829.

Chuang, Y.-C., Lee, S.-C., & Lin, H.-C. (2006). Effect of temperature on the sliding wear behavior of laser surface alloyed Ni-base on Al–Mg–Si alloy. *Applied Surface Science, 253*(3), 1404-1410.

Clare, A., Oyelola, O., Folkes, J., & Farayibi, P. (2012). Laser cladding for railway repair and preventative maintenance. *Journal of Laser Applications, 24*(3), 032004. doi:doi:http://dx.doi.org/10.2351/1.4710578

Courant, B., Hantzpergue, J. J., Avril, L., & Benayoun, S. (2005). Structure and hardness of titanium surfaces carburized by pulsed laser melting with graphite addition. *Journal of Materials Processing Technology, 160*(3), 374-381. doi:http://dx.doi.org/10.1016/j.jmatprotec.2004.06.025

Courant, B., Hantzpergue, J. J., & Benayoun, S. (1999). Surface treatment of titanium by laser irradiation to improve resistance to dry-sliding friction. *Wear, 236*(1), 39-46.

Cullity, B. D., & Weymouth, J. W. (1957). Elements of X-ray Diffraction. *American Journal of Physics, 25*(6), 394-395.

D'Amato, C., Buhagiar, J., & Betts, J. C. (2014a). Tribological characteristics of an A356 aluminium alloy laser surface alloyed with nickel and Ni-Ti-C. *Applied Surface Science*.

D'Amato, C., Buhagiar, J., & Betts, J. C. (2014b). Tribological characteristics of an A356 aluminium alloy laser surface alloyed with nickel and Ni–Ti–C. *Applied Surface Science, 313*, 720-729.

Das, D. K. (1994). Surface roughness created by laser surface alloying of aluminium with nickel. *Surface and Coatings Technology, 64*(1), 11-15.

DellaCorte, C., & Wood, J. C. (1994). High temperature solid lubricant materials for heavy duty and advanced heat engines.

Denney, P. E., & Whitehead, M. (2014). Hot-wire consumable to provide self-lubricating weld or clad: Patent No. US13/790,202.

Deuis, R. L., Subramanian, C., & Yellup, J. M. (1997). Dry sliding wear of aluminium composites—a review. *Composites Science and technology, 57*(4), 415-435.

Doll, G. L., Evans, R. D., & Ribaudo, C. R. (2006). Coated rolling element bearing cages: Patent No. US6994475 B2.

Dong, S., Xu, B., Wang, Z., Ma, Y., & Liu, W. (2007). *Laser remanufacturing technology and its applications.* Paper presented at the Photonics Asia 2007.

Donnet, C., & Erdemir, A. (2004). Solid lubricant coatings: recent developments and future trends. *Tribology Letters, 17*(3), 389-397.

Draper, C. W., & Poate, J. M. (1985a). Laser surface alloying. *International metals reviews, 30*(1), 85-108.

Draper, C. W., & Poate, J. M. (1985b). Laser surface alloying. *Laser, 30*(1).

Dubourg, L., & Archambeault, J. (2008). Technological and scientific landscape of laser cladding process in 2007. *Surface and Coatings Technology, 202*(24), 5863-5869.

Dubourg, L., Hlawka, F., & Cornet, A. (2002). Study of aluminium–copper–iron alloys: application for laser cladding. *Surface and Coatings Technology, 151*, 329-332.

Dubourg, L., Pelletier, H., Vaissiere, D., Hlawka, F., & Cornet, A. (2002). Mechanical characterisation of laser surface alloyed aluminium–copper systems. *Wear, 253*(9), 1077-1085.

Dubourg, L., Ursescu, D., Hlawka, F., & Cornet, A. (2005). Laser cladding of MMC coatings on aluminium substrate: influence of composition and microstructure on mechanical properties. *Wear, 258*(11), 1745-1754.

Duley, W. (2012). *Laser processing and analysis of materials*: Springer Science & Business Media.

Dursun, T., & Soutis, C. (2014). Recent developments in advanced aircraft aluminium alloys. *Materials & design, 56*(0), 862-871. doi:http://dx.doi.org/10.1016/j.matdes.2013.12.002

Dutta Majumdar, J., Chandra, B. R., Nath, A. K., & Manna, I. (2006). Compositionally graded SiC dispersed metal matrix composite coating on Al by laser surface engineering. *Materials Science and Engineering: A, 433*(1), 241-250.

Dwivedi, D. K. (2006). Wear behaviour of cast hypereutectic aluminium silicon alloys. *Materials & design, 27*(7), 610-616.

Ecer, G. M. (1984). Composite bearing structure of alternating hard and soft metal, and process for making the same: Patent No. US4474861 A.

Eichler, J., & Lesniak, C. (2008). Boron nitride (BN) and BN composites for high-temperature applications. *Journal of the European Ceramic Society, 28*(5), 1105-1109. doi:http://dx.doi.org/10.1016/j.jeurceramsoc.2007.09.005

Elhadj, S., Matthews, M. J., & Yang, S. T. (2014). Combined infrared thermal imaging and laser heating for the study of materials thermophysical and processing

properties at high temperatures. *Critical Reviews in Solid State and Materials Sciences, 39*(3), 175-196.

Erdemir, A. (2005). Review of engineered tribological interfaces for improved boundary lubrication. *Tribology International, 38*(3), 249-256.

Ezazi, M. A., Quazi, M. M., Zalnezhad, E., & Sarhan, A. A. D. (2014a). Enhancing the tribo-mechanical properties of aerospace AL7075-T6 by magnetron-sputtered Ti/TiN, Cr/CrN & TiCr/TiCrN thin film ceramic coatings. *Ceramics international, 40*(10), 15603-15615. doi:10.1016/j.ceramint.2014.07.067

Ezazi, M. A., Quazi, M. M., Zalnezhad, E., & Sarhan, A. A. D. (2014b). Enhancing the tribo-mechanical properties of aerospace AL7075-T6 by magnetron-sputtered Ti/TiN, Cr/CrN & TiCr/TiCrN thin film ceramic coatings. *Ceramics international*.

Farahmand, P., & Kovacevic, R. (2014). Parametric Study and Multi-Criteria Optimization in Laser Cladding by a High Power Direct Diode Laser. *Lasers in Manufacturing and Materials Processing, 1*(1), 1-20. doi:10.1007/s40516-014-0001-0

Farahmand, P., & Kovacevic, R. (2015). Laser cladding assisted with an induction heater (LCAIH) of Ni–60%WC coating. *Journal of Materials Processing Technology, 222*(0), 244-258. doi:http://dx.doi.org/10.1016/j.jmatprotec.2015.02.026

Fariaut, F., Boulmer-Leborgne, C., Semmar, N., & Le Menn, E. (2006). High-speed mass-transport phenomena during carburization of aluminum alloy by laser plasma treatment. *Applied Physics A, 83*(1), 95-101.

Figueroa, R., Abreu, C. M., Cristóbal, M. J., & Pena, G. (2012). Effect of nitrogen and molybdenum ion implantation in the tribological behavior of AA7075 aluminum alloy. *Wear, 276–277*(0), 53-60. doi:http://dx.doi.org/10.1016/j.wear.2011.12.005

Fouilland-Paille, L., Ettaqi, S., Benayoun, S., & Hantzpergue, J. J. (1997). Structural and mechanical characterization of Ti/TiC cermet coatings synthesized by laser melting. *Surface and Coatings Technology, 88*(1–3), 204-211. doi:http://dx.doi.org/10.1016/S0257-8972(96)02925-8

Fu, Y., & Batchelor, A. W. (1998). Laser alloying of aluminum alloy AA 6061 with Ni and Cr. Part II. The effect of laser alloying on the fretting wear resistance. *Surface and Coatings Technology, 102*(1), 119-126.

Gardos, M. N. (2000). Magnéli phases of anion-deficient rutile as lubricious oxides. Part I. Tribological behavior of single-crystal and polycrystalline rutile (Ti n O2n− 1). *Tribology Letters, 8*(2-3), 65-78.

Goldstein, J. (2012). *Practical scanning electron microscopy: electron and ion microprobe analysis*: Springer Science & Business Media.

Gopagoni, S., Scharf, T. W., Banerjee, R., & Tiley, J. S. (2013). Solid lubricating, hard and fracture resistant composites for surface engineering applications: Patent No. US3/769,787.

Han, B., Xue, M. P., Wang, Y., & Yu, M. F. (2012). Influence of MoS2 on the Microstructures and Properties of Ni-Based Alloying Coating. *Applied Mechanics and Materials, 130*, 1276-1280.

Hatch, J. E., & Aluminum, A. (1984). *Aluminum: properties and physical metallurgy*: ASM International.

He, X.-M., Liu, X.-B., Wang, M.-D., Yang, M.-S., Shi, S.-H., Fu, G.-Y., & Chen, S.-F. (2011). Elevated temperature dry sliding wear behavior of nickel-based composite coating on austenitic stainless steel deposited by a novel central hollow laser cladding. *Applied Surface Science, 258*(1), 535-541.

Herbst-Dederichs, C. (2005). Thermally applied coating of mechanically alloyed powders for piston rings: Patent No. US6887585 B2.

Hirschhron, J. S., & Daver, E. M. (1969). Wear and friction studies of nickel–tungsten carbide–graphite composites. *Powder Metallurgy, 12*(24), 519-537.

Holmberg, K. (1992). A concept for friction mechanisms of coated surfaces. *Surface and Coatings Technology, 56*(1), 1-10.

Huang, K., Lin, X., Xie, C., & Yue, T. M. (2008). Microstructure and wear behaviour of laser-induced thermite reaction Al2O3 ceramic coatings on pure aluminum and AA7075 aluminum alloy. *Journal of Wuhan University of Technology-Mater. Sci. Ed., 23*(1), 89-94.

Hung, C.-F., & Lin, J. (2004). Solidification model of laser cladding with wire feeding technique. *Journal of Laser Applications, 16*(3), 140-146. doi:doi:http://dx.doi.org/10.2351/1.1771167

Jendrzejewski, R., Van Acker, K., Vanhoyweghen, D., & Śliwiński, G. (2009). Metal matrix composite production by means of laser dispersing of SiC and WC powder in Al alloy. *Applied Surface Science, 255*(10), 5584-5587.

Jin, H. W., Rajagopalan, S., Ozekcin, A., Haque, T., Ertas, M. D., Zhao, B., Bailey, J. R., & Walker, T. F. (2013). Ultra-low friction coatings for drill stem assemblies: Patent No. US8561707 B2.

Kalita, S. J. (2011). Microstructure and corrosion properties of diode laser melted friction stir weld of aluminum alloy 2024 T351. *Applied Surface Science, 257*(9), 3985-3997. doi:http://dx.doi.org/10.1016/j.apsusc.2010.11.163

Kathuria, Y. P. (2000). Some aspects of laser surface cladding in the turbine industry. *Surface and Coatings Technology, 132*(2), 262-269.

Katipelli, L. R., Agarwal, A., & Dahotre, N. B. (2000). Laser surface engineered TiC coating on 6061 Al alloy: microstructure and wear. *Applied Surface Science, 153*(2), 65-78.

Kato, K. (2000). Wear in relation to friction — a review. *Wear, 241*(2), 151-157. doi:http://dx.doi.org/10.1016/S0043-1648(00)00382-3

Kawasaki, M., Kobayashi, T., & Oshima, T. (2004). Wear-resistant copper-base alloy: Patent No. US20040045641 A1.

Kawasaki, M., Mori, K., Takagi, S., & Ueda, K. (1988). Aluminum alloy cylinder head with valve seat formed integrally by copper alloy cladding layer and underlying alloy layer: Patent No. US06944850.

Kawasaki, M., Oshima, T., Kobayashi, T., Nakanishi, K., & Tachikawa, H. (2009). Wear-resistant copper-based alloy: Patent No. US7507305 B2.

Kazuhisa, M. (2007). Solid lubricants and coatings for extreme environments: state-of-the art survey. *NASA/TM-2007-214668*.

Kek, T., & Grum, J. (2010). Influence of the graphite absorber during laser surface hardening. *Strojniški vestnik-Journal of Mechanical Engineering, 56*(2), 150-157.

Kimura, Y., Wakabayashi, T., Okada, K., Wada, T., & Nishikawa, H. (1999). Boron nitride as a lubricant additive. *Wear, 232*(2), 199-206.

Klug, H. P., & Alexander, L. E. (1954). *X-ray diffraction procedures* (Vol. 2): Wiley New York.

Kostoglou, N., Polychronopoulou, K., & Rebholz, C. (2015). Thermal and chemical stability of hexagonal boron nitride (h-BN) nanoplatelets. *Vacuum, 112*(0), 42-45. doi:http://dx.doi.org/10.1016/j.vacuum.2014.11.009

Labisz, K. (2014). Microstructure and mechanical properties of high power diode laser (HPDL) treated cast aluminium alloys. *Materialwissenschaft und Werkstofftechnik, 45*(4), 314-324.

Lei, Y., Sun, R., Tang, Y., & Niu, W. (2015). Microstructure and phase transformations in laser clad CrxSy/Ni coating on H13 steel. *Optics and Lasers in Engineering, 66*(0), 181-186. doi:http://dx.doi.org/10.1016/j.optlaseng.2014.09.006

Leyland, A., & Matthews, A. (2000). On the significance of the H/E ratio in wear control: a nanocomposite coating approach to optimised tribological behaviour. *Wear, 246*(1–2), 1-11. doi:http://dx.doi.org/10.1016/S0043-1648(00)00488-9

Li, L. (2000). The advances and characteristics of high-power diode laser materials processing. *Optics and Lasers in Engineering, 34*(4–6), 231-253. doi:http://dx.doi.org/10.1016/S0143-8166(00)00066-X

Li, Y., Yang, X.-Y., Feng, Y., Yuan, Z.-Y., & Su, B.-L. (2012). One-dimensional metal oxide nanotubes, nanowires, nanoribbons, and nanorods: synthesis, characterizations, properties and applications. *Critical Reviews in Solid State and Materials Sciences, 37*(1), 1-74.

Liu, S., Zhang, Y., & Kovacevic, R. (2015). Numerical Simulation and Experimental Study of Powder Flow Distribution in High Power Direct Diode Laser Cladding Process. *Lasers in Manufacturing and Materials Processing, 2*(4), 199-218. doi:10.1007/s40516-015-0015-2

Liu, W.-G., Liu, X.-B., Zhang, Z.-G., & Guo, J. (2009). Development and characterization of composite Ni–Cr–C–CaF2 laser cladding on γ -TiAl intermetallic alloy. *Journal of Alloys and Compounds, 470*(1–2), L25-L28. doi:http://dx.doi.org/10.1016/j.jallcom.2008.03.020

Liu, X.-B., Liu, H.-Q., Liu, Y.-F., He, X.-M., Sun, C.-F., Wang, M.-D., Yang, H.-B., & Qi, L.-H. (2013). Effects of temperature and normal load on tribological behavior of nickel-based high temperature self-lubricating wear-resistant composite coating. *Composites Part B: Engineering, 53*(0), 347-354. doi:http://dx.doi.org/10.1016/j.compositesb.2013.05.032

Liu, X.-B., Liu, H.-Q., Meng, X.-J., Sun, C.-F., Wang, M.-D., Qi, L.-H., Shi, G.-L., & Wu, S.-H. (2014). Effects of aging treatment on microstructure and tribological properties of nickel-based high-temperature self-lubrication wear resistant composite coatings by laser cladding. *Materials chemistry and physics, 143*(2), 616-621. doi:http://dx.doi.org/10.1016/j.matchemphys.2013.09.043

Liu, X.-B., Meng, X.-J., Liu, H.-Q., Shi, G.-L., Wu, S.-H., Sun, C.-F., Wang, M.-D., & Qi, L.-H. (2014). Development and characterization of laser clad high temperature self-lubricating wear resistant composite coatings on Ti–6Al–4V alloy. *Materials & design, 55*, 404-409. doi:http://dx.doi.org/10.1016/j.matdes.2013.09.038

Liu, X.-B., Shi, S.-H., Guo, J., Fu, G.-Y., & Wang, M.-D. (2009). Microstructure and wear behavior of γ /Al4C3/TiC/CaF2 composite coating on γ -TiAl intermetallic alloy prepared by Nd:YAG laser cladding. *Applied Surface Science, 255*(11), 5662-5668. doi:http://dx.doi.org/10.1016/j.apsusc.2008.11.023

Liu, X.-B., Zheng, C., Liu, Y.-F., Fan, J.-W., Yang, M.-S., He, X.-M., Wang, M.-D., Yang, H.-B., & Qi, L.-H. (2013). A comparative study of laser cladding high temperature wear-resistant composite coating with the addition of self-lubricating WS2 and WS2/(Ni–P) encapsulation. *Journal of Materials Processing Technology, 213*(1), 51-58. doi:http://dx.doi.org/10.1016/j.jmatprotec.2012.07.017

Lo, K. H., Cheng, F. T., Kwok, C. T., & Man, H. C. (2003). Improvement of cavitation erosion resistance of AISI 316 stainless steel by laser surface alloying using fine WC powder. *Surface and Coatings Technology, 165*(3), 258-267.

Mabhali, L. A. B., Sacks, N., & Pityana, S. (2012). Three body abrasion of laser surface alloyed aluminium AA1200. *Wear, 290*, 1-9.

Maiman, T. (2002). Stimulated optical radiation in ruby. *SPIE milestone series*(173), 61-61.

Majumdar, J. D., & Manna, I. (2003). Laser processing of materials. *Sadhana, 28*(3-4), 495-562.

Man, H. C., Kwok, C. T., & Yue, T. M. (2000). Cavitation erosion and corrosion behaviour of laser surface alloyed MMC of SiC and Si3N4 on Al alloy AA6061. *Surface and Coatings Technology, 132*(1), 11-20. doi:http://dx.doi.org/10.1016/S0257-8972(00)00729-5

Man, H. C., Yang, Y. Q., & Lee, W. B. (2004). Laser induced reaction synthesis of TiC+ WC reinforced metal matrix composites coatings on Al 6061. *Surface and Coatings Technology, 185*(1), 74-80.

Man, H. C., Zhang, S., & Cheng, F. T. (2007). Improving the wear resistance of AA 6061 by laser surface alloying with NiTi. *Materials Letters, 61*(19), 4058-4061.

Man, H. C., Zhang, S., Yue, T. M., & Cheng, F. T. (2001). Laser surface alloying of NiCrSiB on Al6061 aluminium alloy. *Surface and Coatings Technology, 148*(2), 136-142.

McCrea, J., Katugaha, H., Palumbo, G., Panagiotopoulos, K., Brooks, I., Nagarajan, N., & Hirmer, G. (2014). Metal-clad hybrid article having synergistic mechanical properties: Patent No. US20140004352 A1.

Mendez, P. F., Barnes, N., Bell, K., Borle, S. D., Gajapathi, S. S., Guest, S. D., Izadi, H., Gol, A. K., & Wood, G. (2014). Welding processes for wear resistant overlays. *Journal of Manufacturing Processes, 16*(1), 4-25.

Milella, E., Cosentino, F., Licciulli, A., & Massaro, C. (2001). Preparation and characterisation of titania/hydroxyapatite composite coatings obtained by sol–gel process. *Biomaterials, 22*(11), 1425-1431. doi:http://dx.doi.org/10.1016/S0142-9612(00)00300-8

Miller Jr, R. G. (1997). *Beyond ANOVA: basics of applied statistics*: CRC Press.

Milonni, P. W. (2015). Lasers: the first 50 years: Scope: review, general interest. Level: general readership, teacher, undergraduate. *Contemporary Physics*, 1-4.

Miotello, A., & Ossi, P. M. (2010). *Laser-surface interactions for new materials production* (Vol. 130): Springer.

Miyoshi, K. (2007). Solid lubricants and coatings for extreme environments: state-of-the-art survey.

Mondal, S., Bandyopadhyay, A., & Pal, P. (2014). Application of artificial neural network for the prediction of laser cladding process characteristics at Taguchi-based optimized condition. *The International Journal of Advanced Manufacturing Technology, 70*(9-12), 2151-2158. doi:10.1007/s00170-013-5393-z

Mondal, S., Bandyopadhyay, A., & Pal, P. K. (2011). Ni-Cr-Mo cladding on mild steel surface using CO2 laser and process modeling with response surface methodology (RSM). *International Journal of Engineering Science and Technology, 1*(3), 6805-6816.

Natarajan, S., Edward Anand, E., Akhilesh, K. S., Rajagopal, A., & Nambiar, P. P. (2016). Effect of graphite addition on the microstructure, hardness and abrasive wear behavior of plasma sprayed NiCrBSi coatings. *Materials chemistry and physics, 175*, 100-106. doi:http://dx.doi.org/10.1016/j.matchemphys.2016.02.076

Nath, S., Pityana, S., & Dutta Majumdar, J. (2012). Laser surface alloying of aluminium with WC+ Co+ NiCr for improved wear resistance. *Surface and Coatings Technology, 206*(15), 3333-3341.

Niu, W., Sun, R., & Lei, Y. (2011). *Microstructure and wear properties of self-lubricating MoS2/Ni coating by laser cladding.* Paper presented at the Electronics and Optoelectronics (ICEOE), 2011 International Conference on.

Nowotny, S., Brueckner, F., Thieme, S., Leyens, C., & Beyer, E. (2015). High-performance laser cladding with combined energy sources. *Journal of Laser Applications, 27*(S1), S17001. doi:doi:http://dx.doi.org/10.2351/1.4817455

Oñate, J. I., Alonso, F., & García, A. (1998). Improvement of tribological properties by ion implantation. *Thin solid films, 317*(1–2), 471-476. doi:http://dx.doi.org/10.1016/S0040-6090(97)00564-6

Ouyang, J. H., Nowotny, S., Richter, A., & Beyer, E. (2001). Laser cladding of yttria partially stabilized ZrO2 (YPSZ) ceramic coatings on aluminum alloys. *Ceramics international, 27*(1), 15-24.

Panagopoulos, C. N., & Georgiou, E. P. (2007). Wear behaviour of 5083 wrought aluminium alloy under free corrosion conditions. *Tribology-Materials, Surfaces & Interfaces, 1*(3), 161-164.

Pariona, M. M., Teleginski, V., dos Santos, K., de Lima, A. A. O. C., Zara, A. J., Micene, K. T., & Riva, R. (2013). Influence of laser surface treated on the characterization and corrosion behavior of Al–Fe aerospace alloys. *Applied surface science, 276*, 76-85.

Pawlowski, L. (1999). Thick laser coatings: A review. *Journal of thermal spray technology, 8*(2), 279-295.

Peng, D.-X. (2011). Optimization of Welding Parameters on Wear Performance of Cladded Layer with TiC Ceramic via a Taguchi Approach. *Tribology Transactions, 55*(1), 122-129. doi:10.1080/10402004.2011.636172

Peng, D.-X., & Kang, Y. (2014). Wear Behavior of Ceramic Powder and Solid Lubricant Cladding on Carbon Steel Surface. *Tribology Transactions, 58*(1), 177-185. doi:10.1080/10402004.2014.951749

Peng, L. (2013). Preparation and Tribological Properties of NiCrBSiC Reinforced Laser Alloying Layer. *Tribology Transactions, 56*(4), 697-702. doi:10.1080/10402004.2013.782619

Peyre, P., & Fabbro, R. (1995). Laser shock processing: a review of the physics and applications. *Optical and Quantum Electronics, 27*(12), 1213-1229. doi:10.1007/BF00326477

Picas, J. A., Forn, A., Rilla, R., & Martín, E. (2005). HVOF thermal sprayed coatings on aluminium alloys and aluminium matrix composites. *Surface and Coatings Technology, 200*(1), 1178-1181.

Podgornik, B., Kosec, T., Kocijan, A., & Donik, Č. (2015). Tribological behaviour and lubrication performance of hexagonal boron nitride (h-BN) as a replacement for graphite in aluminium forming. *Tribology International, 81*(0), 267-275. doi:http://dx.doi.org/10.1016/j.triboint.2014.09.011

Podgornik, B., Kosec, T., Kocijan, A., & Donik, Č. (2015). Tribological behaviour and lubrication performance of hexagonal boron nitride (h-BN) as a replacement for graphite in aluminium forming. *Tribology International, 81*, 267-275.

Prasad, S. V., McDevitt, N. T., & Zabinski, J. S. (1999). Tribology of tungsten disulfide films in humid environments:: The role of a tailored metal-matrix composite substrate. *Wear, 230*(1), 24-34. doi:http://dx.doi.org/10.1016/S0043-1648(99)00082-4

Praveen, B. M., & Venkatesha, T. V. (2008). Electrodeposition and properties of Zn-nanosized TiO2 composite coatings. *Applied Surface Science, 254*(8), 2418-2424. doi:http://dx.doi.org/10.1016/j.apsusc.2007.09.047

Quintino, L., Costa, A., Miranda, R., Yapp, D., Kumar, V., & Kong, C. J. (2007). Welding with high power fiber lasers–a preliminary study. *Materials & design, 28*(4), 1231-1237.

Ramesh, C. S., & Prasad, T. B. (2008). Friction and Wear Behavior of Graphite-Carbon Short Fiber Reinforced Al–17%Si Alloy Hybrid Composites. *Journal of Tribology, 131*(1), 014501-014501. doi:10.1115/1.2991124

Ravnikar, D., Dahotre, N. B., & Grum, J. (2013). Laser coating of aluminum alloy EN AW 6082-T651 with TiB2 and TiC: Microstructure and mechanical properties. *Applied Surface Science, 282*, 914-922.

Reeves, C. J., Menezes, P. L., Lovell, M. R., & Jen, T.-C. (2013). Tribology of Solid Lubricants *Tribology for Scientists and Engineers* (pp. 447-494): Springer.

Renevier, N. M., Hamphire, J., Fox, V. C., Witts, J., Allen, T., & Teer, D. G. (2001). Advantages of using self-lubricating, hard, wear-resistant MoS2-based coatings. *Surface and Coatings Technology, 142–144*, 67-77. doi:http://dx.doi.org/10.1016/S0257-8972(01)01108-2

Richardson, D. J., Nilsson, J., & Clarkson, W. A. (2010). High power fiber lasers: current status and future perspectives. *Journal of the Optical Society of America B, 27*(11), B63-B92. doi:10.1364/JOSAB.27.000B63

Richman, R. H., & McNaughton, W. P. (1990). Correlation of cavitation erosion behavior with mechanical properties of metals. *Wear, 140*(1), 63-82. doi:http://dx.doi.org/10.1016/0043-1648(90)90122-Q

Roberts, E. W. (2012). Space tribology: its role in spacecraft mechanisms. *Journal of Physics D: Applied Physics, 45*(50), 503001.

Roy, M., Venkataraman, B., Bhanuprasad, V., Mahajan, Y., & Sundararajan, G. (1992). The effect of participate reinforcement on the sliding wear behavior of aluminum matrix composites. *Metallurgical Transactions A, 23*(10), 2833-2847.

Sarhan, A. A. D., Zalnezhad, E., & Hamdi, M. (2013). The influence of higher surface hardness on fretting fatigue life of hard anodized aerospace AL7075-T6 alloy. *Materials Science and Engineering: A, 560*(0), 377-387. doi:http://dx.doi.org/10.1016/j.msea.2012.09.082

Sarkar, A. (1975). Wear of aluminium-silicon alloys. *Wear, 31*(2), 331-343.

Savan, A., Pflüger, E., Voumard, P., Schröer, A., & Simmonds, M. (2000). Modern solid lubrication: recent developments and applications of MoS2. *Lubrication Science, 12*(2), 185-203.

Sawada, T., Yanagitani, A., Fukumoto, S., Okita, T., Tsuyumu, T., Asami, M., Matsuo, N., Matsuki, S., & Tsujii, Y. (2008). Raw material powder for laser clad valve seat and valve seat using the same: Patent No. US11881396.

Scharf, T. W., & Prasad, S. V. (2013). Solid lubricants: a review. *Journal of materials science, 48*(2), 511-531. doi:10.1007/s10853-012-7038-2

Scruggs, D. M. (1988). Materials transformable from the nonamorphous to the amorphous state under frictional loadings: Patent No. US4725512 A.

Sepeur, S., & Frenzer, G. (2014). Commercial Applications of Nanocomposite Sol-Gel Coatings *Sol-Gel Nanocomposites* (pp. 191-221): Springer.

Sexton, L., Lavin, S., Byrne, G., & Kennedy, A. (2002). Laser cladding of aerospace materials. *Journal of Materials Processing Technology, 122*(1), 63-68.

Sibillano, T., Ancona, A., Berardi, V., Schingaro, E., Basile, G., & Mario Lugarà, P. (2006). A study of the shielding gas influence on the laser beam welding of AA5083 aluminium alloys by in-process spectroscopic investigation. *Optics and Lasers in Engineering, 44*(10), 1039-1051.

Silfvast, W. T. (2004). *Laser fundamentals*: Cambridge University Press.

Singh, A., & Harimkar, S. P. (2012). Laser surface engineering of magnesium alloys: a review. *Journal of Materials, 64*(6), 716-733.

Sinnott, S. B., & Andrews, R. (2001). Carbon nanotubes: synthesis, properties, and applications. *Critical Reviews in Solid State and Materials Sciences, 26*(3), 145-249.

Sliney, H. E. (1993). *Solid lubricants*: ASM International.

Soleymani, S., Abdollah-Zadeh, A., & Alidokht, S. A. (2012). Microstructural and tribological properties of Al5083 based surface hybrid composite produced by friction stir processing. *Wear, 278*, 41-47.

Sorkin, V., Pan, H., Shi, H., Quek, S. Y., & Zhang, Y. W. (2014). Nanoscale Transition Metal Dichalcogenides: Structures, Properties, and Applications. *Critical Reviews in Solid State and Materials Sciences, 39*(5), 319-367.

Spalvins, T. (1987). A review of recent advances in solid film lubrication. *Journal of Vacuum Science & Technology A, 5*(2), 212-219.

Stachowiak, G. W. (2006). *Wear: materials, mechanisms and practice*: John Wiley & Sons.

Staia, M. H., Cruz, M., & Dahotre, N. B. (2000). Microstructural and tribological characterization of an A-356 aluminum alloy superficially modified by laser alloying. *Thin solid films, 377*, 665-674.

Staia, M. H., Cruz, M., & Dahotre, N. B. (2001). Wear resistance of a laser alloyed A-356 aluminum/WC composite. *Wear, 251*(1), 1459-1468.

Steen, W., & Mazumder, J. (2010). *Laser material processing*: Springer Science & Business Media.

Taguchi, G. (1987). Systems of experimental design: engineering methods to optimize quality and minimize cost. *Quality Resources, White Plains, New York*.

Taguchi, G., & Phadke, M. S. (1989). Quality engineering through design optimization *Quality Control, Robust Design, and the Taguchi Method* (pp. 77-96): Springer.

Tang, F., Wu, X., Ge, S., Ye, J., Zhu, H., Hagiwara, M., & Schoenung, J. M. (2008). Dry sliding friction and wear properties of B4C particulate-reinforced Al-5083 matrix composites. *Wear, 264*(7–8), 555-561. doi:http://dx.doi.org/10.1016/j.wear.2007.04.006

Tao, Z., Xun, C., Shunxing, W., & Shian, Z. (2000). Effect of CeO2 on microstructure and corrosive wear behavior of laser-cladded Ni/WC coating. *Thin solid films, 379*(1–2), 128-132. doi:http://dx.doi.org/10.1016/S0040-6090(00)01536-4

Tian, Y. S., Chen, C. Z., Chen, L. X., & Huo, Q. H. (2006). Microstructures and wear properties of composite coatings produced by laser alloying of Ti–6Al–4V with graphite and silicon mixed powders. *Materials Letters, 60*(1), 109-113. doi:http://dx.doi.org/10.1016/j.matlet.2005.07.082

Tobar, M. J., Alvarez, C., Amado, J. M., Rodríguez, G., & Yáñez, A. (2006). Morphology and characterization of laser clad composite NiCrBSi–WC coatings on stainless steel. *Surface and Coatings Technology, 200*(22), 6313-6317.

Todokoro, H., & Ezumi, M. (1999). Scanning electron microscope: Google Patents.

Tomida, S., Nakata, K., Saji, S., & Kubo, T. (2001). Formation of metal matrix composite layer on aluminum alloy with TiC-Cu powder by laser surface alloying process. *Surface and Coatings Technology, 142*, 585-589.

Touloukian, Y. S., & DeWitt, D. P. (1970). *Thermophysical Properties of Matter-The TPRC Data Series. Volume 7. Thermal Radiative Properties-Metallic Elements and Alloys*. Retrieved from

Toyserkani, E., Khajepour, A., & Corbin, S. F. (2004). *Laser cladding*: CRC press.

Uenishi, K., & Kobayashi, K. F. (1999). Formation of surface layer based on Al3Ti on aluminum by laser cladding and its compatibility with ceramics. *Intermetallics, 7*(5), 553-559.

Uhlmann, E., Sammler, F., Meixner, M., Heinrich, D., Gansert, F., Reimers, W., Berger, D., & Rieck, I. (2014). Analysis of residual stresses and wear mechanism of HF-CVD diamond coated cemented carbide tools. *Production Engineering*, 1-9.

Verwimp, J., Rombouts, M., Geerinckx, E., & Motmans, F. (2011). Applications of Laser Cladded WC-Based Wear Resistant Coatings. *Physics Procedia, 12, Part A*, 330-337. doi:http://dx.doi.org/10.1016/j.phpro.2011.03.042

Vigneau, J., Lesnevskiy, L., & Troshin, A. (2006). Method of protecting contacting surfaces between two metal parts benefiting from such protection: Patent No. US11/171,324.

Viswanathan, A., Sastikumar, D., Kumar, H., & Nath, A. K. (2012). Laser processed TiC–Al13Fe4 composite layer formation on Al–Si alloy. *Optics and Lasers in Engineering, 50*(9), 1321-1329.

Voevodin, A. A., & Zabinski, J. S. (2005). Nanocomposite and nanostructured tribological materials for space applications. *Composites Science and technology, 65*(5), 741-748. doi:http://dx.doi.org/10.1016/j.compscitech.2004.10.008

Vreeling, J. A., Ocelık, V., Hamstra, G. A., Pei, Y. T., & De Hosson, J. T. M. (2000). In-situ microscopy investigation of failure mechanisms in Al/SiC p metal matrix composite produced by laser embedding. *Scripta Materialia, 42*(6), 589-595.

Wang, A. H., & Xie, C. S. (2001). Microstructural study of laser-clad Fe-Al bronze on Al-Si alloy. *Journal of materials science, 36*(8), 1975-1979.

Wang, A. H., Zhang, X. L., Zhang, X. F., Qiao, X. Y., Xu, H. G., & Xie, C. S. (2008). Ni-based alloy/submicron WS2 self-lubricating composite coating synthesized by Nd:YAG laser cladding. *Materials Science and Engineering: A, 475*(1–2), 312-318. doi:http://dx.doi.org/10.1016/j.msea.2007.04.087

Wang, H. M., Yu, Y. L., & Li, S. Q. (2002). Microstructure and tribological properties of laser clad CaF2/Al2O3 self-lubrication wear-resistant ceramic matrix composite coatings. *Scripta Materialia, 47*(1), 57-61. doi:http://dx.doi.org/10.1016/S1359-6462(02)00086-6

Wang, K. L., Zhang, Q. B., Sun, M. L., Wei, X. G., & Zhu, Y. M. (2001). Rare earth elements modification of laser-clad nickel-based alloy coatings. *Applied Surface Science, 174*(3), 191-200.

Wang, K. L., Zhu, Y. M., & Steen, W. M. (2000). Laser remelting of plasma sprayed coatings. *Journal of Laser Applications, 12*(4), 175-178. doi:doi:http://dx.doi.org/10.2351/1.521930

Wang, L., Wang, B., Wang, X., & Liu, W. (2007). Tribological investigation of CaF2 nanocrystals as grease additives. *Tribology International, 40*(7), 1179-1185. doi:http://dx.doi.org/10.1016/j.triboint.2006.12.003

Wang, L., Zhou, J., Yu, Y., Guo, C., & Chen, J. (2012). Effect of powders refinement on the tribological behavior of Ni-based composite coatings by laser cladding. *Applied Surface Science, 258*(17), 6697-6704.

Wang, M., Li, Y., Wang, Z., & Bao, E. (2011). Effect of rare earth elements on the thermal cracking resistance of high speed steel rolls. *Journal of Rare Earths, 29*(5), 489-493.

Wang, Y., Ju, Y., Shakoor, R., Kahraman, R., & Gao, W. (2014). Nanocomposite Ni–TiO2 coatings produced by pulsed electroplating. *Materials Research Innovations, 18*(sup4), S4-1102-S1104-1106.

Wang, Y., Ju, Y., Wang, S., Lu, W., Yan, B., & Gao, W. (2014). Sol enhanced Ni-TiO2 composite coating on hypereutectic Al-Si alloy. *Materials Research Innovations, 18*(S4), S4-1107-S1104-1111.

Wang, Y., Li, G., Shi, Z., Liu, M., Zhang, X., & Liu, Y. (2014). Effects of graphite addition on the microstructure and properties of laser cladding Zr–Al–Ni–Cu amorphous coatings. *Journal of Alloys and Compounds, 610*, 713-717.

Warren, B. E. (1969). *X-ray Diffraction*: Courier Corporation.

Watkins, K. G., McMahon, M. A., & Steen, W. M. (1997). Microstructure and corrosion properties of laser surface processed aluminium alloys: a review. *Materials Science and Engineering: A, 231*(1), 55-61.

Weng, F., Chen, C., & Yu, H. (2014). Research status of laser cladding on titanium and its alloys: a review. *Materials & design, 58*, 412-425.

Wong, T. T., Liang, G. Y., He, B. L., & Woo, C. H. (2000). Wear resistance of laser-clad Ni–Cr–B–Si alloy on aluminium alloy. *Journal of Materials Processing Technology, 100*(1), 142-146.

Xiang, Z.-F., Liu, X.-B., Ren, J., Luo, J., Shi, S.-H., Chen, Y., Shi, G.-L., & Wu, S.-H. (2014). Investigation of laser cladding high temperature anti-wear composite coatings on Ti6Al4V alloy with the addition of self-lubricant CaF2. *Applied Surface Science, 313*(0), 243-250. doi:http://dx.doi.org/10.1016/j.apsusc.2014.05.196

Xu, J., Li, Z., Zhu, W., Liu, Z., & Liu, W. (2007). Investigation on microstructural characterization of in situ TiB/Al metal matrix composite by laser cladding. *Materials Science and Engineering: A, 447*(1), 307-313.

Xu, J., Liu, W., Kan, Y., & Zhong, M. (2006). Microstructure and wear properties of laser cladding Ti–Al–Fe–B coatings on AA2024 aluminum alloy. *Materials & design, 27*(5), 405-410.

Xu, J., Liu, W., & Zhong, M. (2006). Microstructure and dry sliding wear behavior of MoS2/TiC/Ni composite coatings prepared by laser cladding. *Surface and Coatings Technology, 200*(14–15), 4227-4232. doi:http://dx.doi.org/10.1016/j.surfcoat.2005.01.036

Yan, H., Wang, A. H., Zhang, X. L., Huang, Z. W., Wang, W. Y., & Xie, J. P. (2010). Nd: YAG laser cladding Ni base alloy/nano-h-BN self-lubricating composite coatings. *Materials Science and Technology, 26*(4), 461-468.

Yan, H., Zhang, J., Zhang, P., Yu, Z., Li, C., Xu, P., & Lu, Y. (2013). Laser cladding of Co-based alloy/TiC/CaF2 self-lubricating composite coatings on copper for continuous casting mold. *Surface and Coatings Technology, 232*(0), 362-369. doi:http://dx.doi.org/10.1016/j.surfcoat.2013.05.036

Yan, H., Zhang, P., Yu, Z., Lu, Q., Yang, S., & Li, C. (2012). Microstructure and tribological properties of laser-clad Ni–Cr/TiB2 composite coatings on copper with the addition of CaF2. *Surface and Coatings Technology, 206*(19–20), 4046-4053. doi:http://dx.doi.org/10.1016/j.surfcoat.2012.03.086

Yang, G. R., Huang, C. P., Song, W. M., Ma, Y., & Hao, Y. (2015). *The Effect of Graphite Content on the Wear Behavior of Ni/WC/G Composite Coating.* Paper presented at the Advanced Materials Research.

Yang, H. Z., Qiao, X. G., Wang, Y. P., Ali, M. M., Lai, M. H., Lim, K. S., & Ahmad, H. (2015). In-Fiber Gratings for Simultaneous Monitoring Temperature and Strain in Ultrahigh Temperature. *Photonics Technology Letters, IEEE, 27*(1), 58-61.

Yang, J. X., Wang, Z. C., Miao, X. H., & Wang, X. B. (2012). Microstructure and Tribological Properties of Self-Lubricating Graphite/Ni60 Composite Coatings Prepared by Laser Cladding. *Advanced Materials Research, 583*, 27-31.

Yang, M.-S., Liu, X.-B., Fan, J.-W., He, X.-M., Shi, S.-H., Fu, G.-Y., Wang, M.-D., & Chen, S.-F. (2012). Microstructure and wear behaviors of laser clad NiCr/Cr3C2–WS2 high temperature self-lubricating wear-resistant composite coating. *Applied Surface Science, 258*(8), 3757-3762. doi:http://dx.doi.org/10.1016/j.apsusc.2011.12.021

Yang, R., Liu, Z., Wang, Y., Yang, G., & Li, H. (2013). Synthesis and characterization of MoS2/Ti composite coatings on Ti6Al4V prepared by laser cladding. *AIP Advances, 3*(2), 022106.

Ye, H. (2003). An overview of the development of Al-Si-Alloy based material for engine applications. *Journal of materials engineering and performance, 12*(3), 288-297. doi:10.1361/105994903770343132

Zhang, F. Y., & Yan, M. F. (2014). Microstructure and mechanical properties of multiphase coating produced by plasma nitriding Ti coated GB-5083 aluminum alloy. *Surface and Coatings Technology, 253*(0), 268-276. doi:http://dx.doi.org/10.1016/j.surfcoat.2014.05.055

Zhang, H. X., Yu, H. J., & Chen, C. Z. (2014). In-situ Forming Composite Coating by Laser Cladding C/B4C. *Materials and Manufacturing Processes, 30*(6), 743-747. doi:10.1080/10426914.2014.994772

Zhang, S., Zhou, J., Guo, B., Zhou, H., Pu, Y., & Chen, J. (2008). Friction and wear behavior of laser cladding Ni/hBN self-lubricating composite coating. *Materials Science and Engineering: A, 491*(1–2), 47-54. doi:http://dx.doi.org/10.1016/j.msea.2007.12.015

Zhang, S., Zhou, J., Guo, B., Zhou, H., Pu, Y., & Chen, J. (2010). Friction and Wear Behavior of Laser Cladding NiAl/hBN Self-Lubricating Composite Coating *Advanced Tribology* (pp. 442-442): Springer.

Zhong, M., & Liu, W. (2010). Laser surface cladding: the state of the art and challenges. *Proceedings of the Institution of Mechanical Engineers, Part C: Journal of Mechanical Engineering Science, 224*(5), 1041-1060.

Zhu, L., Luo, L., Wu, Y., & Cheng, J. (2014). Microstructure and tribological properties of laser clad Ni-Ag/Tic composite coating. *Journal of Wuhan University of Technology-Mater. Sci. Ed., 29*(2), 242-245. doi:10.1007/s11595-014-0901-z

LIST OF PUBLICATIONS

(a) **Journal Papers Accepted**

Review Papers

1. **M.M Quazi**, M.A. Fazal, A.S.M.A. Haseeb, Farazila Yusof, H.H Masjuki, A. Arslan, Laser-based Surface Modifications of Aluminum and its Alloys, *Critical Reviews in Solid State and Materials Sciences*, (2015) 1-26. *ISI, Q1, i.f. (5.5)*
2. **M.M Quazi**, M.A. Fazal, A.S.M.A. Haseeb, Farazila Yusof, H.H Masjuki, A. Arslan, Laser based self-lubricating wear resistant composite coatings. *Lasers in manufacturing and materials processing*, (2016) 1-33. *Non-ISI, New Journal*
3. **M.M Quazi**, M.A. Fazal, A.S.M.A. Haseeb, Farazila Yusof, H.H Masjuki, A. Arslan, Effect of rare-earth elements and their oxides on tribo-mechanical performance of laser claddings: A review. *Journal of rare earths*, (2016) *Accepted. ISI, Q2, i.f. (2.1)*

Technical Papers

4. **M.M Quazi**, M.A. Fazal, A.S.M.A. Haseeb, Farazila Yusof, H.H Masjuki, A. Arslan, Laser composite surfacing of Ni-WC coating on AA5083 for enhancing tribo-mechanical properties. *Tribology Transactions*, (2016*) Accepted. ISI, Q2, i.f. (1.5)*

(b) **Journal Papers under review**

Technical Papers

1. **M.M Quazi**, M.A. Fazal, A.S.M.A. Haseeb, Farazila Yusof, H.H Masjuki, A. Arslan, , Effect of solid lubricants on friction and wear performance of laser composite surfaced Al-Si hypereutectic alloy. *Surface & Coatings Technology*, (2016*), Under Review, ISI, Q1, i.f. (2.2) – Major Revision*

(c) **Related Journal Papers with collaborations in the field of surface engineering**

1. M.A. Ezazi, **M.M. Quazi**, E. Zalnezhad, A.A.D. Sarhan, Enhancing the tribo-mechanical properties of aerospace AL7075-T6 by magnetron-sputtered Ti/TiN, Cr/CrN & TiCr/TiCrN thin film ceramic coatings, *Ceramics International*, 40 (2014) 15603-15615.
2. Q.M. Mehran, A.R. Bushroa, M.A. Fazal, **M.M. Quazi,** Scratch adhesion characteristics of PVD Cr/CrAlN multilayer coating deposited on aerospace AL7075-T6 alloy, *Pigment & Resin Technology*, 44 (2015).
3. A. Arslan, H.H. Masjuki, M. Varman, M.A. Kalam, **M.M. Quazi**, K.A.H. Al Mahmud, M. Gulzar, M. Habibullah, Effects of texture diameter and depth on the tribological performance of DLC coating under lubricated sliding condition, *Applied Surface Science*, 356 (2015) 1135-1149.
4. A. Arslan, H.H. Masjuki, M. Varman, M.A. Kalam, **M.M. Quazi**, M.H. Mosarof, Effect of change in temperature on the tribological performance of micro surface textured DLC coating. *Journal of Materials Research*, FirstView: 1-11 (2016).
5. J. Bhatti, M.A. Fazal, A. Faheem Khan, A.R. Bushroa, **M.M. Quazi**, Investigation of the mechanical properties of electrodeposited nickel and magnetron sputtered chromium nitride coatings deposited on mild steel substrate. *Journal of Adhesion Science and Technology*, (2016).
6. A. Arslan, H.H. Masjuki, M. Varman, M.A. Kalam, M.H. Mosarof, **M.M. Quazi,** Surface texture manufacturing techniques and tribological effect of surface texturing on cutting tool performance: a review, *Critical Reviews in Solid State and Materials Sciences*, (2016).

7. J. Bhatti, M.A. Fazal, A. Faheem Khan, A.R. Bushroa, **M.M. Quazi,** Structural and mechanical properties of (Cr, Ni) N single and gradient layer coatings deposited on mild steel by magnetron sputtering, *Tribology - Materials, Surfaces & Interfaces*, (2016).

(c) Conference papers, posters and presentations

1. M.A Ezazi, **M. M. Quazi** E. Zalnezhad, Ahmed A. D. Sarhan, "Hard Anodizing of Aerospace AL7075-T6 alloy for improving hardness and wear resistance", International symposium on Coatings Technology 2014, IMTCE 2014,Malaysia, 14–15th May 2014, (Oral Presentation) - Presenter **M. M. Quazi**
2. **M. M. Quazi**, M.A Ezazi, E. Zalnezhad, Ahmed A. D. Sarhan, "Wear resistance investigation of Anodised AL7075-T6", International symposium on Coatings Technology 2014, IMTCE 2014, Malaysia, 14–15th May 2014, (Poster Presentation) Presenter **M. M. Quazi**
3. Q.M Mehran, **M. M. Quazi**, M.A. Fazal, A.R. Bushroa, "Scratch Adhesion characteristics of PVD Cr/CrAlN multilayered coating deposited on Aerospace AL7075-T6 alloy", International symposium on Coatings Technology 2014, IMTCE 2014, Malaysia, 14–15th May 2014, (Poster Presentation)
4. A. Arslan, H. Masjuki, M. Varman, A. Kalam, R. Mufti, M. Gulzar, **M.M. Quazi,** Effect of surface texture on the tribological performance of DLC coating, Proceedings of Malaysian International Tribology Conference 2015, MITC 2015, 246-247, (Conference paper)
5. **M.M. Quazi**, M.A. Fazal, A.S.M.A Haseeb, H.H. Masjuki, E. Zalnezhad", Adhesion of PVD multilayer ceramic coating on AA7075-T6 aerospace alloy", 3rd Malaysia-Japan Tribology Symposium 2014 (MJTS2014), 11–12th Nov 2014, Kuala Lumpur, Malaysia (Oral Presentation, Presenter **M. M. Quazi**

AWARDS

1. **M.M. Quazi**, M.A. Fazal, A.S.M.A Haseeb, H.H. Masjuki, E. Zalnezhad", Adhesion of PVD multilayer ceramic coating on AA7075-T6 aerospace alloy", 3rd Malaysia-Japan Tribology Symposium 2014 (MJTS2014), 11–12th Nov 2014, Kuala Lumpur, Malaysia (Oral Presentation & Best student research award) Presenter **M. M. Quazi**
2. Fully funded Summer School on Lasers and Laser Applications (SSOLLA 2015) held at APRI, Gwangju Institute of Science and Technology (GIST), Korea. (Lasers Safety Training Certification), 7-13th Jul 2015.